Numerical Renormalization Group Studies of the Partially Broken SU(3) Kondo Model

Dissertation
zur
Erlangung des Doktorgrades (Dr. rer. nat.)
der
Mathematisch-Naturwissenschaftlichen Fakultät
der
Rheinischen Friedrich-Wilhelms-Universität Bonn

von
Evaristus Fuh Chuo
aus
Wum, Kamerun

Bonn 2013

Dieser Forschungsbericht wurde als Dissertation von der Mathematisch-Naturwissenschaftlichen Fakultät der Universität Bonn angenommen und ist auf dem Hochschulschriftenserver der ULB Bonn http://hss.ulb.uni-bonn.de/diss_online elektronisch publiziert.

1. Gutachter:	Prof. Dr. Johann Kroha
2. Gutachter:	PD. Dr. Ralf Bulla
Tag der Promotion:	16.04.2013
Erscheinungsjahr:	2013

This thesis is dedicated posthumously to my dad,
Fuh Chuo Clement, who passed away
during the course of this work.

Acknowledgement

I would like to take this singular and ultimate opportunity to express my sincere gratitude to those who in one way or the other helped me in the course of this piece of work. It is not possible for me to list all of them here by name. I am grateful.

I want especially to express appreciation to my supervisor, Prof. Dr. Johann Kroha who was always there when I needed him and greatly made this work not too difficult for me.

Special acknowledgement is due to the German Academic Exchange Service (DAAD) for providing the funds for my entire PhD project. A particular thank you to Dr. Laszlo Borda for all the NRG tricks he taught me and the great attention he paid to me during my visit at the Budapest University of Technology and Economics.

Of course, I am grateful to PD. Dr. Ralf Bulla for his very meticulous advice and suggestions every time I visited him in Cologne. I am equally indebted to Dr. Eran Sela for his inquisitiveness towards the model used in this thesis that let to some serious collaborations between us. Special thanks to Dr. Christian Kremers for giving me the necessary support needed to cope in a foreign country like Germany. I could not fail to mention, however, my debt to all the members of the Kroha group especially Katinka Ballmann, Ammar Nejati, and Zhong Yuan Lai for some useful discussions. Lastly, I want to thank my family and all my friends most specially Aji James for being there for me during the very trying time that my dad passed away.

Thus goes an old Aghem proverb “the river only meandered because there was no one to advise it”.

Abstract

The two-channel Kondo (2CK) effect with its exotic ground state properties has remained difficult to realize in physical systems. At low energies, a quantum impurity with orbital degree of freedom, like a proton bound in an interstitial lattice space, comprises a 3-level system with a unique ground state and (at least) doubly degenerate rotational excitations with excitation energy Δ_0. When immersed in a metal, electronic angular momentum scattering induces transitions between any two of these levels (couplings J), while the electron spin is conserved. We show by extensive numerical renormalization group (NRG) [1] calculations that without fine-tuning of parameters this system exhibits a 2CK fixed point, due to Kondo correlations in the excited-state doublet whose degeneracy is stabilized by the host lattice parity, while the channel symmetry (electron spin) is guaranteed by time reversal symmetry. We find a pronounced plateau in the entropy at $S(T_K < T < \Delta_0) = k_B \ln 2$ between the high-T value, $S(T \gg \Delta_0) = k_B \ln 3$, and the 2CK ground state value, $S(0) = k_B \ln \sqrt{2}$. This indicates a downward renormalization of the doublet below the non-interacting ground state, thus realizing the 2CK fixed point, in agreement with earlier conjectures [2]. We mapped out the phase diagram of the model in the $J - \Delta_0$ plane. The Kondo temperature T_K shows non-monotonic J-dependence, characteristic for 2CK systems.

Beside the two-channel Kondo effect of the model, we also study the single-channel version, which is realized by applying a strong magnetic field to the conduction band electrons so that their degeneracy is lifted and consequently having only one kind of electrons scattering off the impurity. This single-channel case is easier to analyze since the Hilbert space is not as large as that of the 2CK. We equally find a downward renormalization of the excited state energy by the Kondo correlations in the SU(2) doublet. In a wide range of parameter values this stabilizes the single-channel Kondo fixed point and a phase diagram is also mapped out for the model. In the single-channel version a plateau is found in the entropy at $S(T_K < T < \Delta_0) = k_B \ln 2$ between high-T value, $S(T \gg \Delta_0) = k_B \ln 3$, and the single-channel Kondo ground state value, $S(0) = k_B \ln 1$.

Zusammenfassung

Der zwei-Kanal Kondo Effekt (2CK) mit seinen außergewöhnlichen Grundzustandseigenschaften ist bisher physikalisch schwer zu realisieren gewesen. Eine niederenergetische Quantenstörstelle mit Drehimpulsfreiheitsgrad, wie z.B. ein gebundenes Proton an einer Gitterstörstelle, bildet ein 3-Level-System mit genau einem Grundzustand und einer (mindestens) zweifach entarteten Rotationsanregung mit Anregungsenergie. Befindet sich eine solche Störstelle in einem Metall, so werden durch Drehimpuls-Streuung Übergänge zwischen diesen entarteten Anregungen induziert (Kopplungsstärke J), wobei der Elektronenspin erhalten bleibt. Wir haben durch umfassende numerische Renormierungsgruppen (NRG)-Rechnungen [1] gezeigt, dass solche Systeme, selbst ohne Feinabstimmung der Kopplungsparameter, einen 2CK Fixpunkt aufweisen. Grund dafür sind Kondo Korrelationen der angeregten Doublets, deren Entartung durch die Parität der Gitterstruktur stabilisiert wird, während die Zerfallskanal-Symmetrie auf Grund der Zeitumkehrinvarianz garantiert ist. Die Berechnungen haben gezeigt, dass die Entropie $S(T_K < T < \Delta_0) = k_B \ln 2$ ein ausgeprägtes Plateau im Energieintervall zwischen dem Wert bei hohen Energien $S(T \gg \Delta_0) = k_B \ln 3$ und dem 2CK Grundzustand $S(0) = k_B \ln \sqrt{2}$ aufweist. Das ist ein numerischer Beweis dafür, dass das angeregte Doublet einen energetisch niedrigeren Zustand annimmt als der nicht interagierende Grundzustand. Damit wurde die zuvor gemachte Vermutung [2] bestätigt, dass sich in derartigen Systemen ein 2CK Fixpunkt realisieren lässt. Weiterhin haben wir ein Phasendiagramm des Modells in der $J - \Delta_0$ Ebene erstellt. Dies weist eine für 2CK Systeme typische nicht monotone Abhängigkeit der Kondotemperatur T_K von der Kopplungskonstanten J auf.

Zusätzlich zu dem zwei-Kanal Kondo Effekt (2CK) haben wir auch den ein-Kanal Kondo Effekt (1CK) eines solchen Systems untersucht, der sich durch das Anlegen eines starken Magnetfeldes verwirklichen lässt. Das Magnetfeld hebt die Entartung auf, so dass nur noch Elektronen eines Spinzustandes von der Störstelle gestreut werden. Die Untersuchungen des ein-Kanal Effektes sind numerisch weniger aufwendig, da der relevante Teil des Hilbert-Raumes deutlich kleiner als beim 2CK Effekt ist. Die Untersuchungen belegten ebenfalls eine Energieabnahme des angeregten Zustandes hervorgerufen durch Kondo Korrelationen innerhalb des SU(2) Doublets. Dadurch wird der ein-Kanal Kondo Fixpunkt innerhalb eines großen Parameterraumes stabilisiert. Dies ist deutlich dem erstellten Phasendiagramm zu entnehmen. Das Plateau der Entropy $S(T_K < T < \Delta_0) = k_B \ln 2$ befindet sich in der ein-Kanal Version des Kondo Effektes in demselben Energieintervall als beim 2CK Effekt und nimmt dort denselben Wert $S(T) = k_B \ln 2$ an. Die Entropie bei hohen Energien ist ebenfalls identisch zu dem 2CK Fall, wohingegen der 1CK Grundzustand die Entropie $S(0) = k_B \ln 1$ besitzt.

Nomenclature

NRG	Numerical Renormalization Group
1CK	Single-Channel Kondo
2CK	Two-Channel Kondo
TLS	Two-Level Systems
RG	Renormalization Group
T_K	Kondo Temperature
RGT	Renormalization Group Theory
AIM	Anderson Impurity Model
PRG	Perturbative Renormalization Group
k_B	Boltzmann Constant
ln	Natural Logarithm
Fig	Figure
fcc	face-centered cubic

List of Figures

List of Tables

Contents

Chapter 1

Introduction

The Kondo effect is a cornerstone in condensed matter physics that enables the understanding of the behavior of metallic systems with strongly interacting electrons. It has been studied for more than 70 years but has not ceased to amaze physicists because of the discoveries of more exotic ground states. The Kondo effect has a wide range of applications especially as an indicator of the purity of a metal from magnetic impurities, it serves as an example of the simplest possible magnetic systems, it also serves as a good example of asymptotic freedom, which is the theory that explains the situation where the coupling becomes non-perturbatively strong at low temperatures and low energies. When extended to a lattice of magnetic impurities, the Kondo effect can likely explain the formation of heavy fermions and Kondo insulators in intermetallic compounds etc.

The Kondo effect for magnetic impurities in metals was first explained by Jun Kondo in 1964 [4] (modeled as the single-channel Kondo model). However, Kondo's explanation is only valid down to a certain temperature and below this temperature, this theory makes an unphysical prediction (which says that resistivity diverges as the temperature approaches zero). The breakdown of Kondo's explanation became known in the literature as the Kondo problem and the temperature at which it breaks down as the Kondo temperature. The Kondo problem was solved ten years later by Kenneth Wilson using the numerical renormalization group (NRG) technique that he invented [1]. An analytical solution for the so called single-channel Kondo (1CK) effect was provided a few years later in 1980 by Natan Andrei and P.B. Wiegmann [5, 6]. The result of their work further confirmed the work Wilson had earlier done on the Kondo model using the NRG.

Nozières and Blandin in 1980 proposed a generalization of the single-channel Kondo model in which more than one conduction channels of electrons interact independently with the impurity through exchange coupling [7]. This was the birth of the multi-channel Kondo model. When only two conduction channels are considered the result is two-channel Kondo (2CK) effect. The 2CK effect is an archetype for electronic correlations in metals and so far a physical realization has been clear only in special fine-tuned systems. The 2CK unlike the 1CK effect has an exotic non-Fermi liquid ground state with a non-vanishing zero point entropy. After the introduction of the 2CK, NRG calculations were done on it which confirmed the non-Fermi liquid nature of the ground state [8] and the stability of the 2CK effect fixed point against anisotropy [9]. The theoretical framework for the calculation of some of its thermodynamic and dynamical properties has been worked out using methods such as the Bethe Ansatz [10, 11], the conformal field theory [12, 13, 14], and other methods like the Majorana fermion representation of the problem

[15].

It was later realized that the Kondo effect is not limited only to the case where the impurity is magnetic but occurs whenever a discrete, degenerate quantum degree of freedom is exchange-coupled to one or more conduction bands of electrons. In the case of more than one conduction band, they must be exchange-coupled in a symmetrical way. Vládar and Zawadowski were the first to suggest a model for a non-magnetic impurity Kondo model which was the two-level system (TLS) [16]. The TLS is a double well potential with an atom immersed in a metal. In this system the role of the impurity spin is played by internal degrees of freedom of the TLS and the magnetic spin of the conduction electrons serve as a channel index. In fact, in this system, the 2CK scenario results directly by virtue of the degeneracy of the magnetic spin of the electrons of the conduction band. However, the TLS has the obvious shortcoming in that it does not adequately explain 2CK behavior as detailed in [17, 18]. Due to the drawbacks of the TLS, Arnold et al. [2] proposed a model that could circumvent this drawbacks.

The reason why some experiments like that of Ralph and Buhrmann [3] have been barely understood till now is because there is no microscopic model with a stable 2CK fixed point. Consequently some of the fascinating observations made by Ralph and Buhrmann in their experiment are still not completely apprehended.

In this thesis, the partially broken SU(3) Kondo model proposed by Arnold et al. as a realistic, microscopic model for the 2CK effect is examined. The kondo degrees of freedom in this model are the parity-degenerate rotational states of an atomic three-level system and the flavor or channel degree of freedom is the magnetic spin of the conduction band electrons. This model is very robust with respect to dynamical screening as well as to coupling to higher impurity excitations as detailed out in [19]. Arnold et al. used the perturbative renormalization group (PRG) to study the physics of this model.

Our goal in this thesis is to use the non-perturbative technique, the NRG to show that the partially broken SU(3) Kondo model has a 2CK behavior in a wide parameter range, calculate some physical properties of the model and show that its Kondo temperature has two different kinds of behavior with respect to the coupling J. The rest of the thesis is organized as follows:

In Chapter 2, a pedagogical approach is used to explain the Kondo effect. It starts up with the phenomenology of the Kondo effect and then briefly gives an outline of magnetic impurities. The different methods used to understand the Kondo effect are also tackled in this chapter. The chapter ends by discussing the 1CK effect and giving its characteristics.

Chapter 3 focuses on the 2CK effect. It gives the physical description of the 2CK model and RG analysis of this model. It also explains the duality behavior of the 2CK model and ends with some characteristics of non-Fermi liquids.

In Chapter 4, two non-magnetic impurity models are presented and briefly explained. These two models are the TLS and the partially broken SU(3) Kondo model. The choice of these two models is due to their relevance to this work.

Chapter 5 presents an overview of the NRG method and the rationale behind the various steps of the method necessary for solving the Kondo problem.

In Chapter 6, the NRG presented in the previous chapter is used to solve the partially broken SU(3) Kondo model. The matrices necessary for the NRG calculation are given and the different states of the system are calculated. The results are presented, starting with the 1CK version of the partially broken SU(3) Kondo model which is obtained when the conduction band electrons are all polarized in the same direction. A phase diagram and the entropy for this 1CK model are also shown. In the second part of this chapter the more challenging calculations of the 2CK version of this model are carried out and the energy flows are shown which shows two 2CK characteristics. The phase diagram for the 2CK model is also presented and the duality and the non-monotonicity of the Kondo temperature behavior of this model is explicitly demonstrated too. The impurity contribution to the entropy of the system is calculated in the presence and absence of a small magnetic field.

We present the conclusion and give an outlook in chapter 7.

The Appendix gives some details on the NRG method as well as the calculations of the different basis states and the starting matrices necessary for the NRG procedure. The implementation of symmetries in the NRG method is done here and last but not least, a detailed calculation of the impurity entropy using the NRG method is presented.

Chapter 2

The Kondo effect and the renormalization group theory

The story of Kondo physics started in Leiden in 1934 when de Haas et al., [20] observed a resistivity minimum in seemingly pure gold, silver, and copper samples. This resistivity minimum was later explained by Jun Kondo [4] in 1964 as due to the presence of magnetic impurity atoms, such as manganese, iron, chromium, etc, in the gold metal. He used perturbation theory to calculate the resistivity, however, this theory breaks down at a certain temperature when the coupling becomes large. The temperature for which this happens became known as the Kondo temperature T_K. The search for a solution beyond the T_K became known in the literature as the Kondo problem while the explanation of the minimum is known as the Kondo effect.

For many problems in physics perturbation theory is divergent. The Kondo problem is such a problem and so to solve it, one needs a technique like the renormalization group theory (RGT) which solves these types of problems. In this chapter, we discuss the Kondo effect and some of the methods that are used to obtain the interesting physics that comes out of it. We will briefly introduce methods like perturbation theory which was used by Jun Kondo to explain the effect and also the basic ideas behind a more robust method like the RGT.

2.1 Phenomenology

The electrical resistivity of metals is ordinarily caused by impedance to the free flow of conduction electrons. This usually arises as a result of the conduction electrons being scattered off phonons. The quanta of vibrations of ionic lattice are known as phonons. One would expect that as the temperature is lowered, less and less phonons will be excited, and the electrical resistivity will decrease monotonically. It turns out that in the presence of a few magnetic impurities, the simple picture painted above is no longer respected. The resistivity rather passes through a minimum and increases before saturating to a finite value. The analysis of this problem is not a simple one, since we have to deal with a many-body problem that can not be reduced to a one-body case. Fig. 2.1 gives a picture of the different scenarios that set in as the temperature is lowered. Firstly, at high temperature, the major contributor to the resistivity are phonons which cause a resistivity varying as T^5. It is indicated in Fig. 2.1 by the blue part of the curve and would decrease monotonically in the absence of impurities or imperfections in the metal. In the presence of magnetic impurities, at low temperatures, the curve passes through a minimum and starts to increase (the red part of the curve), an effect which is due to spin flip scattering off the impurity and is proportional to ln$T$. At much lower temperatures (the green part of the curve), there is the formation of a singlet due to screening of the local moment. The temperature at which the singlet is formed is known as the Kondo temperature.

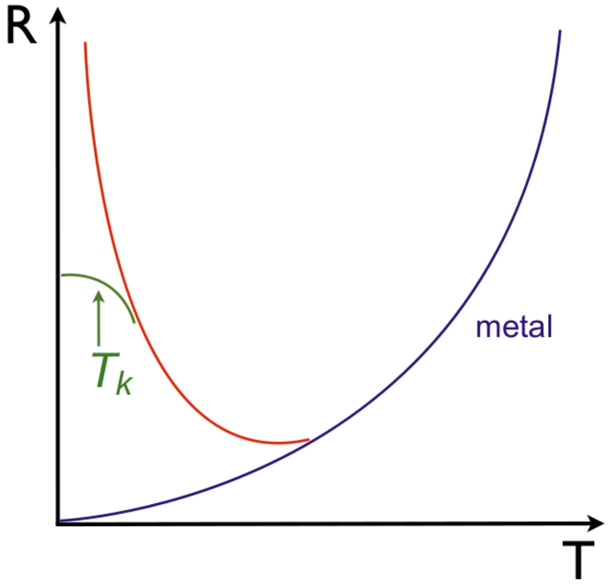

Figure 2.1: The change of resistivity R as the temperature T is decreased. The blue line is for phonon scattering proportional to T^5, while the red line is the spin flip scattering of the impurity which is proportional to $\ln T$, and lastly the green curve is the screening of the local moment that leads to the formation of a singlet.

2.2 Impurity magnetic moments in metals

The obvious question to ask here is, why does iron, cobalt, or manganese in copper have magnetic moments whereas gold in copper does not? The answer to this is electrostatic repulsive interactions between electrons. We will attempt to explain this by using the Anderson impurity model (AIM) [21]. In this section we will briefly explain the AIM and then show how the Kondo model is obtained from it as an effective low temperature model using the Schrieffer-Wolff transformation.

2.2.1 Anderson impurity model

Iron atoms have incomplete d-shells with non-zero total spin. This means that the iron atom has a singly occupied orbital when it is in isolation. When this atom is brought in contact with conduction electrons by being placed inside a metal, there is a chance for hybridization to occur. This means that it is possible for one of the conduction electrons to jump to the singly occupied impurity orbital and briefly spend some time there. The reverse can actually occur too, that is, an electron of the impurity jumps onto the conduction band. A complete description of these impurities in metals can be modeled using the famous Anderson Hamiltonian.

$$H_A = \sum_{\mathbf{k},\sigma} \varepsilon_{\mathbf{k}} c^{\dagger}_{\mathbf{k}\sigma} c_{\mathbf{k}\sigma} + \varepsilon_d \sum_{\sigma} d^{\dagger}_{\sigma} d_{\sigma} + U d^{\dagger}_{\uparrow} d_{\uparrow} d^{\dagger}_{\downarrow} d_{\downarrow} + V \sum_{\mathbf{k},\sigma} (c^{\dagger}_{\mathbf{k}\sigma} d_{\sigma} + d^{\dagger}_{\sigma} c_{\mathbf{k}\sigma}) \tag{2.1}$$

The first term in (2.1) is the kinetic energy of the conduction electron where $\varepsilon_{\mathbf{k}}$ is the dispersion relation measured relative to the Fermi energy and $c^{\dagger}_{\mathbf{k}\sigma}$ ($c_{\mathbf{k}\sigma}$) is the creation (annihilation) operator. In the second term, ε_d is the energy of the impurity level, $d^{\dagger}_{\sigma}$ and d_{σ} are creation and annihilation operators at the impurity site respectively. The third term is known as the Hubbard term, where U is the Coulomb interaction, that causes a second electron in the impurity orbital to pick up electrostatic potential energy. The last term is the hybridization term which comes about due to hopping of electrons into and out of the impurity orbital. Fig. 2.2 shows both the high and low energy dynamics of the AIM. To describe the low-energy dynamics, one needs to separate out the energy scales.

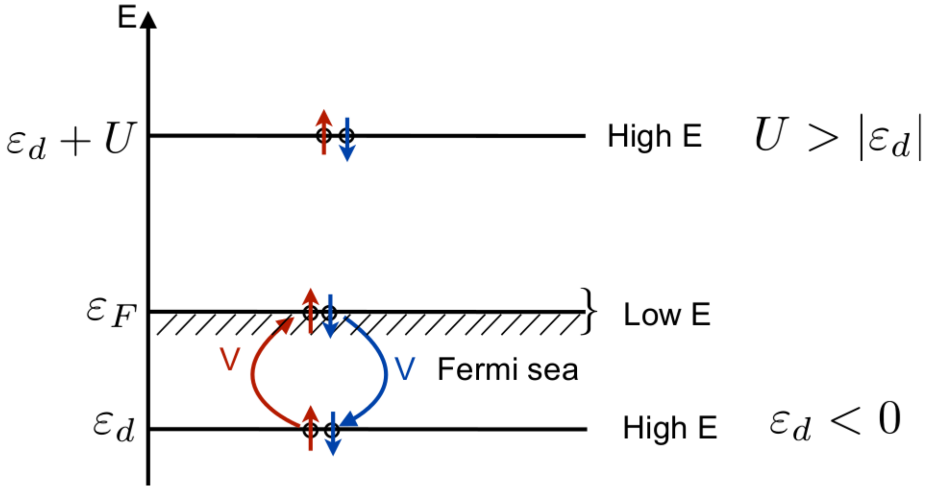

Figure 2.2: Energy level scheme of the Anderson impurity model, where the High and Low E values on the plot denote the absolute values of the energy difference of the various energy levels from the Fermi level ε_F.

2.2.2 Origin of the Kondo Hamiltonian

In this subsection we will outline the raison d'etre for briefly introducing the AIM in the preceding subsection. The Kondo model is just an effective model that corresponds to a certain parameter regime of the Anderson model. We will explain how the Kondo Hamiltonian can be obtained from the Anderson Hamiltonian. The condition for a local moment to exist is that the singly occupied configuration lies lowest in energy, that is $\varepsilon_d < \varepsilon_F$, $\varepsilon_d + U > \varepsilon_F$, and $U > |\varepsilon_d|$. For example, some numerical values for the different parameters are: $U \cong 10eV$, $|\varepsilon_d| \cong 0.5V$. Fig. 2.3 shows the different energy levels. For $\frac{U}{|\varepsilon_d|} \gg 1$, the dynamics of the system is effectively restricted to the Hilbert space with $n_d = \sum_{\sigma} d^{\dagger}_{\sigma} d_{\sigma} = 1$

Schrieffer-Wolff transformation

As already mentioned above, the Kondo model can be deduced from the Anderson model using the Schrieffer-Wolff transformation which was first introduced by J. R. Schrieffer

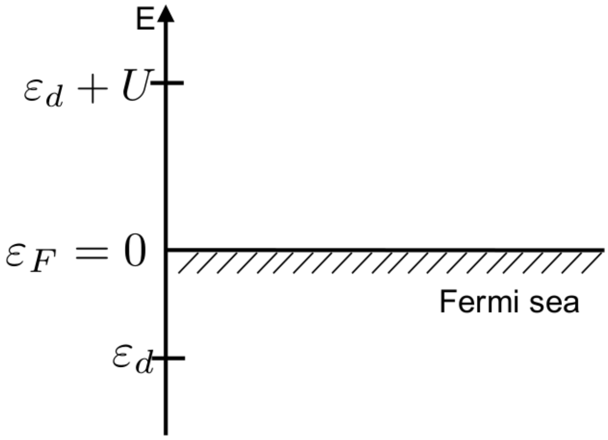

Figure 2.3: Energy conditions for local moment to exist.

and P. A. Wolff in ref. [22]. We will briefly give the rationale behind this transformation and give sketches of calculations required to move from the Anderson Hamiltonian to the Kondo Hamiltonian.

The object usually left behind when a local moment forms within an atom is always a quantum mechanical object with pure spin degrees of freedom. The interaction of these spin degrees of freedom and the surrounding conduction band electrons is usually via virtual charge fluctuations, whereby an electron from the conduction sea briefly migrates onto the ion or vice versa leading to a spin-exchange between the local moment and the conduction band electrons. This process induces an antiferromagnetic interaction between the conduction electrons and the magnetic ion. Fig. 2.4(a) and Fig. 2.4(b) show the two possible spin exchange processes. Fig. 2.4(a) shows the process in which the conduction electron hybridizes with the impurity electron. This only happens if it has the same orbital symmetry. Consequently the intermediate state formed during this process is spatially symmetric and hence has a spin-antisymmetric singlet state. Whereas the process in Fig. 2.4(b) passes through a doubly occupied singlet impurity state and can only occur if the impurity state and incoming conduction electron have opposite spins. It can be noticed that spin exchange only takes place in the singlet channel thereby lowering the energy of the singlet configuration as will be shown below in the sketchy calculation of the Schrieffer-Wolff transformation. One usually starts with the decomposition of the total

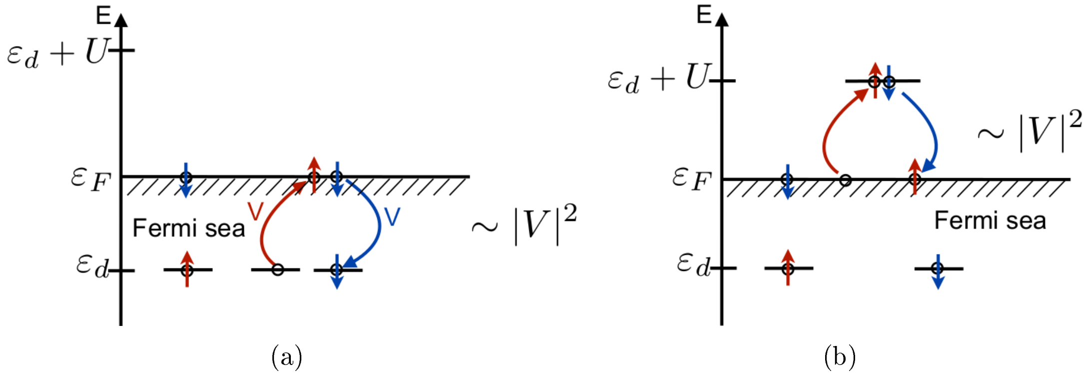

(a)

(b)

Figure 2.4: Spin exchange process that passes (a) through an intermediate state, (b) via a doubly occupied singlet impurity state.

wave function. That is

$$|\psi\rangle = |\psi_0\rangle + |\psi_1\rangle + |\psi_2\rangle \tag{2.2}$$

where $|\psi_m\rangle$, $m = 0, 1, 2$ are components of $|\psi\rangle$ with occupation number $n_d = m$. We also make use of projection operators which act on the different subspaces of $m = 0, 1, 2$. These projectors have the following forms

$$\begin{aligned} P_0 &= (1 - n_{d_\uparrow})(1 - n_{d_\downarrow}) \\ P_1 &= (1 - n_{d_\uparrow})n_{d_\downarrow} + n_{d_\uparrow}(1 - n_{d_\downarrow}) \\ P_2 &= n_{d_\uparrow} n_{d_\downarrow} \end{aligned} \tag{2.3}$$

P_0 is the projection operator on the subspace $m = 0$, P_1 is for $m = 1$, and P_2 for $m = 2$. The projection operators respect the following basic rules

$$\begin{aligned} P_n P_m &= P_n \delta_{nm} \\ \sum_{m=0,1,2} P_m &= 1 \\ |\psi_m\rangle &= P_m |\psi\rangle \end{aligned} \tag{2.4}$$

We can now decompose the Schrödinger equation in the following way

$$P_m H|\psi\rangle = P_m E|\psi\rangle \tag{2.5}$$

When

$$\sum_m P_m^2 = 1 \tag{2.6}$$

is inserted in (2.5), one obtains the following relation

$$\sum_n (P_m H P_n) P_n |\psi\rangle = E P_m |\psi\rangle \tag{2.7}$$

Where P_n is the projection operator onto the subspace with occupation number n. (2.7) can be expressed in matrix form as follows

$$\begin{pmatrix} H_{00} & H_{01} & H_{02} \\ H_{10} & H_{11} & H_{12} \\ H_{20} & H_{21} & H_{22} \end{pmatrix} \begin{pmatrix} \psi_0 \\ \psi_1 \\ \psi_2 \end{pmatrix} = E \begin{pmatrix} \psi_0 \\ \psi_1 \\ \psi_2 \end{pmatrix} \tag{2.8}$$

H_{02} and H_{20} are equal to zero since the Anderson Hamiltonian couples only to neighboring subspaces. To obtain the effective Hamiltonian for $|\psi_1\rangle$, we eliminate $|\psi_0\rangle$ and $|\psi_2\rangle$ from (2.8). The following expression is obtained in terms of $|\psi_1\rangle$

$$[H_{11} + H_{12}(E - H_{22})^{-1} H_{21} + H_{10}(E - H_{00})^{-1} H_{01}]|\psi_1\rangle = E|\psi_1\rangle \tag{2.9}$$

The second and third terms describe virtual excitations. The matrix elements of (2.9) are explicitly written out in the following way:

$$\begin{aligned} H_{00} &= (\sum_{\mathbf{k},\sigma} \varepsilon_{\mathbf{k}} c^\dagger_{\mathbf{k}\sigma} c_{\mathbf{k}\sigma}) P_0 \\ H_{11} &= (\sum_{\mathbf{k},\sigma} \varepsilon_{\mathbf{k}} c^\dagger_{\mathbf{k}\sigma} c_{\mathbf{k}\sigma} + \varepsilon_d \mathbb{1}) P_1 \\ H_{22} &= (\sum_{\mathbf{k},\sigma} \varepsilon_{\mathbf{k}} c^\dagger_{\mathbf{k}\sigma} c_{\mathbf{k}\sigma} + 2\varepsilon_d \mathbb{1} + U\mathbb{1}) P_2 \end{aligned} \tag{2.10}$$

for the diagonal elements and

$$\begin{aligned} H_{10} &= P_1 H P_0 = \sum_{\mathbf{k},\sigma} V_{\mathbf{k}d} d^\dagger_\sigma c_{\mathbf{k}\sigma} P_0, \;\; H_{01} = H_{10}^\dagger \\ H_{21} &= P_2 H P_1 = \sum_{\mathbf{k},\sigma} V^*_{\mathbf{k}d} d^\dagger_\sigma c_{\mathbf{k}\sigma} P_1, \;\; H_{12} = H_{21}^\dagger \end{aligned} \tag{2.11}$$

for the off diagonal elements. Here $\mathbb{1}$ denotes an identity matrix operator. By substituting the above diagonal and off-diagonal elements in the second and third term of (2.9) one obtains these expressions for them

$$\begin{aligned} H_{12}(E-H_{22})^{-1}H_{21} &= -\sum_{\substack{\mathbf{kk}'\\ \sigma\sigma'}} \frac{V^*_{\mathbf{k}'d}V_{\mathbf{k}d}}{U+\varepsilon_d-\varepsilon_{\mathbf{k}}}\left(1-\frac{(E-\varepsilon_d-H_0)}{U+\varepsilon_d-\varepsilon_{\mathbf{k}}}\right)^{-1} d_\sigma d^\dagger_{\sigma'} c^\dagger_{\mathbf{k}\sigma} c_{\mathbf{k}'\sigma'} \\ H_{10}(E-H_{00})^{-1}H_{01} &= -\sum_{\substack{\mathbf{kk}'\\ \sigma\sigma'}} \frac{V^*_{\mathbf{k}'d}V_{\mathbf{k}d}}{\varepsilon_{\mathbf{k}}-\varepsilon_d}\left(1-\frac{(E-\varepsilon_d-H_0)}{\varepsilon_{\mathbf{k}}-\varepsilon_d}\right)^{-1} d^\dagger_\sigma c_{\mathbf{k}\sigma} c^\dagger_{\mathbf{k}'\sigma'} d^\dagger_{\sigma'}. \end{aligned} \tag{2.12}$$

In (2.12) above, the second term in the parenthesis on the right hand side, is much smaller than one, since the system is restricted to a singly occupied subspace ($E-H_0 \approx \varepsilon_d$), that is lowest order in the hybridization $V_{\mathbf{k}d}$, so it is neglected. The following expression is used to express (2.12) in terms of spin dependent expressions,

$$\sum_{\sigma,\sigma'} c^\dagger_{\mathbf{k}\sigma} d^\dagger_{\sigma'} c_{\mathbf{k}'\sigma'} d_\sigma = -2\left(\mathbf{S}_{\mathbf{kk}'}\cdot\mathbf{S}_d + \frac{1}{4}\sum_\sigma c^\dagger_{\mathbf{k}\sigma} c_{\mathbf{k}\sigma} \sum_{\sigma'} n_{d_{\sigma'}}\right) \tag{2.13}$$

where $\mathbf{S}^i_{\mathbf{kk}'} = \frac{1}{2}\sum_{\alpha\beta} c^\dagger_{\mathbf{k}\alpha}(\sigma^i)_{\alpha\beta} c_{\mathbf{k}'\beta'}$ with σ^i the Pauli matrices. The second quantization representation of $\mathbf{S}_d$ is the same, except that in place of c operators there are d's. With the help of the following identity

$$\sum_{i=x,y,z} \sigma^i_{\alpha\beta}\sigma^i_{\gamma\delta} = 2\delta_{\alpha\delta}\delta_{\beta\gamma} - \delta_{\alpha\beta}\delta_{\gamma\delta}, \tag{2.14}$$

one can easily prove (2.13). Where δ is the Kronecker delta function, which is 1 if the variables are equal and 0 if they are different. After some mathematical gymnastics, (2.12) is obtained in terms of spin operators as follows

$$\begin{aligned} H_{12}(E-H_{22})^{-1}H_{21} &= -\sum_{\mathbf{kk}'} \frac{V^*_{\mathbf{k}'d}V_{\mathbf{k}d}}{U+\varepsilon_d-\varepsilon_{\mathbf{k}}}\mathbf{S}_{\mathbf{kk}'}\cdot\mathbf{S}_d - \frac{1}{2}\sum_{\mathbf{kk}'} \frac{V^*_{\mathbf{k}'d}V_{\mathbf{k}d}}{U+\varepsilon_d-\varepsilon_{\mathbf{k}}} c^\dagger_{\mathbf{k}\sigma} c_{\mathbf{k}\sigma} \\ H_{10}(E-H_{00})^{-1}H_{01} &= -\sum_{\mathbf{kk}'} \frac{V^*_{\mathbf{k}'d}V_{\mathbf{k}d}}{\varepsilon_{\mathbf{k}}-\varepsilon_d}\mathbf{S}_{\mathbf{kk}'}\cdot\mathbf{S}_d - \frac{1}{2}\sum_{\mathbf{kk}'} \frac{V^*_{\mathbf{k}'d}V_{\mathbf{k}d}}{\varepsilon_{\mathbf{k}}-\varepsilon_d} c^\dagger_{\mathbf{k}\sigma} c_{\mathbf{k}\sigma} + \sum_{\mathbf{k}} \frac{V^*_{\mathbf{k}'d}V_{\mathbf{k}d}}{\varepsilon_{\mathbf{k}}-\varepsilon_d} \end{aligned} \tag{2.15}$$

where we use the relation $\sum_\sigma n_{d_\sigma} = 1$ in order to obtain the effective Hamiltonian in the singly occupied subspace and by substituting (2.15) in (2.9) thus the following,

$$H_{eff} = \sum_{\mathbf{k},\sigma} \varepsilon_{\mathbf{k}} c^\dagger_{\mathbf{k}\sigma} c_{\mathbf{k}\sigma} + \sum_{\mathbf{kk}'} J_{\mathbf{kk}'}\mathbf{S}_{\mathbf{kk}'}\cdot\mathbf{S}_d + \sum_{\mathbf{kk}'} K_{\mathbf{kk}'} c^\dagger_{\mathbf{k}\sigma} c_{\mathbf{k}\sigma} + \varepsilon_d + \sum_{\mathbf{k}} \frac{V^*_{\mathbf{k}'d}V_{\mathbf{k}d}}{\varepsilon_{\mathbf{k}}-\varepsilon_d}. \tag{2.16}$$

Here the first term is the kinetic energy of conduction electrons, the second term is the effective exchange coupling between the impurity and the conduction sea where the coupling is given by

$$\begin{aligned} J_{\mathbf{k}\mathbf{k}'} &= \frac{V^2}{U+\varepsilon_d-\varepsilon_{\mathbf{k}}} + \frac{V^2}{\varepsilon_{\mathbf{k}}-\varepsilon_d} \\ &\approx \frac{V^2}{U+\varepsilon_d} + \frac{V^2}{-\varepsilon_d} > 0. \end{aligned} \tag{2.17}$$

The second approximate equality holds, because $|\varepsilon_{\mathbf{k}}| \ll |\varepsilon_d|, |\varepsilon_d + U|$ at low energies. $J_{\mathbf{k}\mathbf{k}'} > 0$ means antiferromagnetic coupling. The third term is just a residual potential scattering off the impurity. This term normally vanishes when there is particle-hole symmetry and consequently can be dropped, since it does not involve the internal dynamics of the impurity. The coupling in this third term has the following form

$$K_{\mathbf{k}\mathbf{k}'} = \frac{V^2}{\varepsilon_{\mathbf{k}}-\varepsilon_d} - \frac{V^2}{U+\varepsilon_d-\varepsilon_{\mathbf{k}}} \tag{2.18}$$

The fourth and the fifth terms are just constants, and the energies may be measured with respect to them, thus leading to the famous Kondo Hamiltonian

$$H_K = \sum_{\mathbf{k},\sigma} \varepsilon_{\mathbf{k}} c^\dagger_{\mathbf{k}\sigma} c_{\mathbf{k}\sigma} + \sum_{\mathbf{k}\mathbf{k}'} J_{\mathbf{k}\mathbf{k}'} \mathbf{S}_{\mathbf{k}\mathbf{k}'} \cdot \mathbf{S}_d \tag{2.19}$$

2.3 Kondo metals

2.3.1 Single-channel Kondo problem

The single-channel Kondo model arises when one conduction band of electrons is exchange coupled to the impurity. It is described by the following Hamiltonian

$$H_K = \sum_{\mathbf{k},\sigma} \varepsilon_{\mathbf{k}} c^\dagger_{\mathbf{k}\sigma} c_{\mathbf{k}\sigma} + J\mathbf{S}\cdot \mathbf{s}, \quad J > 0 \tag{2.20}$$

Where $\mathbf{S}$ is the impurity spin operator, $\mathbf{s}$ the conduction electron spin operator. $\mathbf{s}$ is defined in terms of electron operators as follows $\sum_{\mathbf{k}\mathbf{k}'} c^\dagger_{\mathbf{k}\sigma} \vec{\tau}_{\sigma\sigma'} c_{\mathbf{k}'\sigma'}$, $\vec{\tau}$ are the Pauli matrices.

$$\begin{aligned} \vec{\tau} &= \vec{\tau}_x + \vec{\tau}_y + \vec{\tau}_z \\ \vec{\tau}_x &= \begin{pmatrix} 0 & 1 \\ 1 & 0 \end{pmatrix} \\ \vec{\tau}_y &= \begin{pmatrix} 0 & -i \\ i & 0 \end{pmatrix} \\ \vec{\tau}_z &= \begin{pmatrix} 1 & 0 \\ 0 & -1 \end{pmatrix} \end{aligned} \tag{2.21}$$

where$[\tau_i, \tau_j] = 2\epsilon_{ijk}\tau_k$, ϵ_{ijk} is a totally antisymmetric tensor. For example

$$\begin{aligned} S_z &= \frac{1}{2}\sum_{\substack{\mathbf{k}\mathbf{k}' \\ \sigma\sigma'}} c^\dagger_{\mathbf{k}\sigma}\vec{\tau}_{\sigma\sigma'}c_{\mathbf{k}'\sigma'} = \frac{1}{2}\sum_{\mathbf{k}\mathbf{k}'}(c^\dagger_{\mathbf{k}\uparrow}\vec{\tau}_{z\uparrow\uparrow}c_{\mathbf{k}\uparrow} + c^\dagger_{\mathbf{k}\downarrow}\vec{\tau}_{z\downarrow\downarrow}c_{\mathbf{k}'\downarrow}) = \frac{1}{2}\sum_{\mathbf{k}\mathbf{k}'}(c^\dagger_{\mathbf{k}\uparrow}c_{\mathbf{k}'\uparrow} - c^\dagger_{\mathbf{k}\downarrow}c_{\mathbf{k}'\downarrow}) \\ S_x &= \frac{1}{2}\sum_{\mathbf{k}\mathbf{k}'}(c^\dagger_{\mathbf{k}'\uparrow}c_{\mathbf{k}\downarrow} - c^\dagger_{\mathbf{k}\downarrow}c_{\mathbf{k}'\uparrow}) = \frac{1}{2}(S^+ + S^-) \\ S_y &= -\frac{i}{2}(S^+ - S^-) \end{aligned} \tag{2.22}$$

The S^+, S^- are the raising and lowering operators for the spin angular momentum, respectively, whereas S_x, S_y, and S_z depict the three cartesian components of spin angular momentum. τ_x, τ_y, and τ_z are the Pauli matrices.

In order to investigate the Kondo Hamiltonian, one has to treat the quantum nature of the spin, hence a diagrammatic technique for spin operators is required. The problem is that there is no Wick's theorem for spin operators, since their commutators are not c-numbers. To circumvent this problem, we use the pseudo-particle approach for which a brief explanation is given in the next subsection.

2.3.2 Pseudo-particle representation

Abrikosov introduced the pseudo-particle representation in 1965, so as to give a fermionic representation for the local spins [23]. Barnes, 10 years later, defined a pseudo-particle representation of the local impurity level as, empty state $|0\rangle$, two singly occupied states $|\sigma\rangle$, $\sigma =\uparrow,\downarrow$, and doubly occupied state $|2\rangle$ [24]. The definition of different pseudo-particle creation operators that create the states when operating on the vacuum is as follows

$$\begin{aligned} |0\rangle &= b^\dagger|vac\rangle \\ |\sigma\rangle &= f^\dagger_\sigma|vac\rangle, \ \ \sigma =\uparrow,\downarrow \\ |2\rangle &= a^\dagger|vac\rangle \end{aligned} \tag{2.23}$$

with two fermionic operators f_σ and two bosonic operators b and a. The creation operator of an electron in the empty or singly occupied d-level reads

$$\begin{aligned} c^\dagger_{d,\sigma} &= f^\dagger_\sigma b + \sigma a^\dagger f_{-\sigma}, \qquad \sigma = \pm 1 \\ f^\dagger_\sigma b|0\rangle &= f^\dagger_\sigma|vac\rangle = |\sigma\rangle \\ a^\dagger f_{-\sigma}|-\sigma\rangle &= a^\dagger|vac\rangle = |2\rangle \end{aligned} \tag{2.24}$$

The fermionic operators f_σ respect the following commutation relations

$$\begin{aligned} \{f_\sigma, f^\dagger_{\sigma'}\} &= \delta_{\sigma\sigma'} \\ \{f_\sigma, f_{\sigma'}\} &= 0 \end{aligned} \tag{2.25}$$

The introduction of pseudo-particles implies an artificially enlarged Fock space. The physical sector is defined by the constraint that the local d-level should be in one of the four states:

$$Q = \sum_\sigma f^\dagger_\sigma f_\sigma + b^\dagger b + a^\dagger a \overset{!}{=} 1 \tag{2.26}$$

For the Kondo model, one has only the singly occupied states and no doubly and zero occupied states, hence the following constraint

$$Q = \sum_{\sigma} f^{\dagger}_{\sigma} f_{\sigma} \overset{!}{=} 1 \tag{2.27}$$

The impurity spin operator can now be written in terms of pseudo-fermions as follows

$$\begin{aligned}
\vec{S} &= \sum_{\sigma} f^{\dagger}_{\sigma\sigma'} \vec{\tau}_{\sigma\sigma'} f_{\sigma'} \text{ for spin-1/2} \\
S_z &= \frac{1}{2}(f^{\dagger}_{\uparrow} f_{\uparrow} - f^{\dagger}_{\downarrow} f_{\downarrow}) \\
S^{+} &= f^{\dagger}_{\uparrow} f_{\downarrow} \\
S^{-} &= f^{\dagger}_{\downarrow} f_{\uparrow}
\end{aligned} \tag{2.28}$$

Thus, the Kondo Hamiltonian in terms of these spin operators has the following form

$$H_K = \sum_{\mathbf{k},\sigma} \varepsilon_{\mathbf{k}} c^{\dagger}_{\mathbf{k}\sigma} c_{\mathbf{k}\sigma} + J \sum_{\substack{\mathbf{k}\mathbf{k}' \\ \sigma\sigma' \\ \tau\tau'}} (\vec{\tau}_{\tau\tau'} \cdot \vec{\tau}_{\sigma\sigma'}) f^{\dagger}_{\tau} f_{\tau} c^{\dagger}_{\mathbf{k}\sigma} c_{\mathbf{k}'\sigma'} \tag{2.29}$$

In order to project onto the physical sector of the Fock space with $Q = 1$, we use the technique proposed by Abrikosov in [23]. Any physical expectation value $\langle A \rangle$ is to be evaluated in the canonical ensemble where $Q = 1$. The idea is to deduce the expectation value from the grand canonical ensemble with respect to Q. The statistical operator is defined as

$$\rho_G = \frac{1}{Z_G} e^{-\beta(H+\lambda Q)} \tag{2.30}$$

with λ associated with the chemical potential and Z_G denoting the grand canonical partition function of the ensemble,

$$Z_G = tr[e^{-\beta(H+\lambda Q)}] \tag{2.31}$$

where the trace extends over the complete Fock space including the sum over $Q = 0, 1, 2$. The expectation value is thus

$$\langle A \rangle = tr[\rho_G A] = \left.\frac{tr[Ae^{-\beta(H)}]}{tr[e^{-\beta(H)}]}\right|_{Q=1} \tag{2.32}$$

$$\begin{aligned}
\langle A \rangle &= \lim_{\lambda \to +\infty} \frac{tr[Ae^{-\beta(H+\lambda Q)}]}{tr[Qe^{-\beta(H+\lambda Q)}]} \\
&= \lim_{\lambda \to +\infty} \frac{\frac{1}{Z_G} tr[Ae^{-\beta(H+\lambda Q)}]}{\frac{1}{Z_G} tr[Qe^{-\beta(H+\lambda Q)}]} \\
&= \lim_{\lambda \to +\infty} \frac{\langle AQ \rangle_G}{\langle Q \rangle_G} \\
&= \lim_{\lambda \to +\infty} \frac{\langle A \rangle_G}{\langle Q \rangle_G} \text{ for } A|Q = 0\rangle = 0
\end{aligned} \tag{2.33}$$

The constrained impurity Green's function in the grand canonical ensemble is given by

$$G = \lim_{\lambda \to +\infty} \frac{G_\lambda}{\langle Q \rangle_G} \tag{2.34}$$

with G_λ given in terms of the pseudo-fermions and the expectation value of Q in the limit as $\lambda \to \infty$ is defined as follows

$$\lim_{\lambda \to +\infty} \langle Q \rangle_G = \lim_{\lambda \to +\infty} \sum_\sigma \langle f_\sigma^\dagger f_\sigma \rangle_G \tag{2.35}$$

Where $f_\sigma^\dagger$ (f_σ) is the usual fermionic creation (annihilation) operator. The diagrammatic simplification due to $\lim_{\lambda \to +\infty}$ gives the following calculation for the bubble diagram.

$$\begin{aligned} F &= \frac{1}{\beta} \sum_{\omega'} G_\sigma^{(0)}(i\omega') G_{\sigma'}^{(0)}(i\omega - i\omega') \\ &= -\oint \frac{dz}{2\pi i} f(z) \frac{1}{z-\lambda} \frac{1}{z + i\omega - \lambda} \\ &= \frac{f(\lambda) - f(\lambda - i\omega)}{i\omega} \end{aligned} \tag{2.36}$$

When $\lambda \to \infty$ then $e^{-\beta\lambda} \to 0$ the distribution function

$$f(\varepsilon + \lambda) = \frac{1}{e^{-\beta(\varepsilon + \lambda)}} \tag{2.37}$$

This implies that the projection to the pseudo-fermion bubbles such as the one in Fig. 2.5 vanishes.

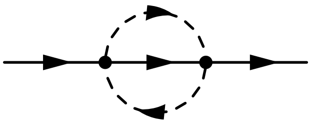

Figure 2.5: An electron selfenergy f-bubble

$$= G_{\mathbf{k}\sigma}(t_{im}) = -\langle \hat{T}\{c_{\mathbf{k}\sigma}(t_{im}) c_{\mathbf{k}\sigma}^\dagger(0)\}\rangle \tag{2.38}$$

$$= G_\sigma(t_{im}) = -\langle \hat{T}\{f_\sigma(t_{im}) f_\sigma^\dagger(0)\}\rangle \tag{2.39}$$

$$G_{\mathbf{k}\sigma}^{(0)}(i\omega) = \frac{1}{i\omega - \varepsilon_p} \tag{2.40}$$

$$G_\sigma^{(0)}(i\nu) = \frac{1}{i\nu - \lambda} \tag{2.41}$$

where $\hat{T}$ is the time ordering operator and t_{im} describes the Euclidean time here. ω and ν both depict the Matsubara frequencies of the conduction electron and impurity, respectively. $G_{\mathbf{k}\sigma}^{(0)}(i\omega)$ and $G_\sigma^{(0)}(i\nu)$ are the free Matsubara Green's functions for electrons and pseudo-fermions, respectively. The dashed line represents the impurity propagator and the full line the conduction electron propagator.

2.3.3 Perturbation theory

After a brief introduction of the Kondo model in the preceding sections, it is now time to carry out an analysis of the Hamiltonian (2.20). The first approach to consider is Kondo's perturbative analysis that gives explanations for the resistivity minimum and explains the low temperature physics down to the Kondo temperature but not beyond. In order to calculate the resistivity of a simple metal with magnetic impurities, we need the scattering amplitude of the electrons in the metal. This scattering amplitude is an element of the T-matrix $\mathcal{T}$, which is usually computed with standard tools of quantum mechanics. Generally, the Hamiltonian is usually in two parts, the kinetic part and the interaction part. The interaction is between the conduction electrons and the impurity spin. Perturbation theory is carried out in J, the exchange interaction between the conduction electron spin and the impurity spin. Knowledge of the T-matrix permits one to calculate the resistivity. When the scattering matrix in first order is considered, one immediately notices that the T-matrix is independent of both the energy and the temperature. As a consequence, the resistivity of the impurity is independent of temperature. Generally, spin independent interactions usually lead to temperature independent contributions to the resistivity. This kind of contributions are termed potential scattering and do not lead to resistivity minimum. The following is a diagram that shows the physical processes described by the first order term in the perturbative expansion.

$$\mathcal{T}^{(1)}_{\mathbf{kk}'\sigma_1\tau_1\sigma_2\tau_2} =$$

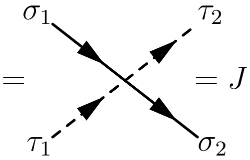

$$= J(\vec{\tau}_{\tau_1\tau_2}\cdot\vec{\tau}_{\sigma_1\sigma_2}) \qquad (2.42)$$

where σ is the conduction electron spin, τ is the spin of the impurity and the solid and dashed lines represent the conduction electron and the impurity propagators, respectively. Since the first order term in perturbation theory does not lead to a resistivity minimum, it is necessary to consider the second order. The following diagrams show the different physical processes taking place during scattering in second order.

$$\mathcal{T}^{(2)}_{\mathbf{kk}'\sigma_1\tau_1\sigma_2\tau_2} =$$

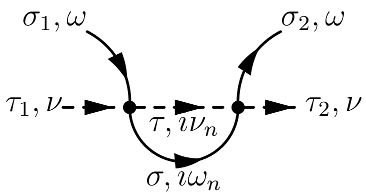

$$+$$

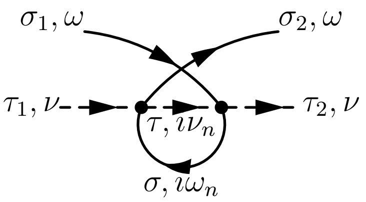

$$(2.43)$$

The above (2.43) represents the second order term in perturbation theory.

$$\begin{aligned}
\mathcal{T}^{(2)}_{\mathbf{kk}'\sigma_1\tau_1\sigma_2\tau_2}(i\omega_n) &= -[(-J)^2\sum_{\tau,\sigma}(\vec{\tau}_{\tau_2\tau}\cdot\vec{\tau}_{\sigma_2\sigma})(\vec{\tau}_{\tau\tau_1}\cdot\vec{\tau}_{\sigma\sigma_1})\cdot\sum_{\mathbf{k}}\frac{1}{\beta}\sum_{\omega_n}G_{\mathbf{k}\sigma}(i\omega_n)\;G_{\tau}(i\nu_n)|_{\lambda\to\infty} \\
&\quad +(-J)^2\sum_{\tau,\sigma}(\vec{\tau}_{\tau_2\tau}\cdot\vec{\tau}_{\sigma\sigma_1})(\vec{\tau}_{\tau\tau_1}\cdot\vec{\tau}_{\sigma_2\sigma})\cdot\sum_{\mathbf{k}}\frac{1}{\beta}\sum_{\omega_n}G_{\mathbf{k}\sigma}(i\omega_n)\;G_{\tau}(i\nu_n)|_{\lambda\to\infty}
\end{aligned} \qquad (2.44)$$

The lines and the symbols are defined as in (2.42), whereas ω_n and ν_n describe the Matsubara frequencies for the conduction electrons and the impurity, respectively. The first term in (2.43) shows how an incoming electron scatters off the impurity into an intermediate state and then scatters again into a final state. This scattering might lead to the flipping of the spin of both the conduction electron and the impurity. The mathematical formula that goes with the first term of (2.43) is the first term in (2.44). The second term in (2.43) describes a much more complicated scattering in which the outgoing electron is first created before the incoming one is annihilated. This diagram also illustrates a many body effect. The formula for this diagram is the second term of (2.44). The first scattering of this diagram creates an electron-hole pair whereas in the second scattering the incoming electron is absorbed by the hole. (2.44) is then computed in order to extract the contributions of both diagrams to the resistivity. With a few mathematical gymnastics, one arrives at an expression that the scattering amplitudes have an explicit temperature dependence. Let *I* and *II* represent the first and second terms of (2.43), respectively.

Energy dependence

We first sum over the different Matsubara frequencies in (2.43) . This can be achieved by transforming the sums into contour integrals. The residue theorem is applied, which changes the sums to complex integrals. This method is necessary and effective because the Matsubara frequencies of the fermions are the poles of Fermi distribution function, $f(\varepsilon_{\mathbf{k}})$. The explicit calculation is given in (2.45) and (2.46) for both second order perturbation theory diagrams. Because of conservation of energy at the vertex for the first term of (2.43), $\omega + \nu = \omega_n + \nu_n$, if $\omega' = \omega + \nu$ then $\nu_n = \omega' - \omega_n$

$$\begin{aligned}
I &\sim \frac{1}{\beta}\sum_{\omega_n} G_{\mathbf{k}\sigma}(i\omega_n)\, G_\tau(i\omega' - i\omega_n)|_{\lambda\to\infty} \\
&= \frac{1}{\beta}\sum_{\omega_n} \frac{1}{i\omega_n - \varepsilon_{\mathbf{k}}} \cdot \frac{1}{i\omega' - i\omega_n - \lambda}\bigg|_{\lambda\to\infty} \\
&= \oint \frac{dz}{2\pi i} f(z) \frac{1}{z - \varepsilon_{\mathbf{k}}} \cdot \frac{1}{i\omega' - z - \lambda}\bigg|_{\lambda\to\infty} \\
&= \sum_{\mathbf{k}} \Big(\frac{f(\varepsilon_{\mathbf{k}})}{i\omega' - \varepsilon_{\mathbf{k}} - \lambda} - \frac{f(i\omega' - \lambda)}{i\omega' - \lambda - \varepsilon_{\mathbf{k}}}\Big)\bigg|_{\lambda\to\infty} \\
&= \sum_{\mathbf{k}} \frac{f(\varepsilon_{\mathbf{k}}) - 1}{i\omega' - \varepsilon_{\mathbf{k}} - \lambda}, \quad i\omega' \to i\omega' + \lambda \\
&= \sum_{\mathbf{k}} \frac{1 - f(\varepsilon_{\mathbf{k}})}{\varepsilon_{\mathbf{k}} - i\omega'} \qquad (2.45)
\end{aligned}$$

The presence of $1 - f(\varepsilon_{\mathbf{k}})$ in (2.45) can only happen if the process shown above was in an initial empty state in the background of the Fermi sea. This occurs with a probability of $1 - f(\varepsilon_{\mathbf{k}})$ while for the second process to be possible in (2.43), the intermediate state has to be occupied with a probability of $f(\varepsilon_{\mathbf{k}})$.

$$\begin{aligned}
II &\sim \frac{1}{\beta}\sum_{\omega_n} G_{\mathbf{k}\sigma}(i\omega_n)\; G_{\tau}(i\omega_n - i\omega')|_{\lambda\to\infty} \\
&= -\oint \frac{dz}{2\pi i} f(z)\frac{1}{z-\varepsilon_{\mathbf{k}}}\cdot \frac{1}{z-i\omega'-\lambda}\bigg|_{\lambda\to\infty} \\
&= \sum_{\mathbf{k}}\Big(\frac{f(\varepsilon_{\mathbf{k}})}{\varepsilon_{\mathbf{k}}-i\omega'-\lambda} - \frac{f(\lambda+i\omega')}{\lambda+i\omega'-\varepsilon_{\mathbf{k}}}\Big)\bigg|_{\lambda\to\infty} \\
&\quad f(\lambda+i\omega') = f(\lambda) \to e^{-\beta\lambda} \to 0;\ i\omega' \to i\omega' - \lambda \\
&= \sum_{\mathbf{k}} \frac{f(\varepsilon_{\mathbf{k}})}{\varepsilon_{\mathbf{k}} - i\omega'}
\end{aligned} \tag{2.46}$$

In both energy dependence calculations, the energy is measured in a way so as to get rid of the λ in the denominator. For the particle-like calculations I, the result is continued analytically by $i\omega' \to i\omega' + \lambda$ whereas for the hole-like calculations II, it is rather $i\omega' \to i\omega' - \lambda$. One can immediately observe that $f(\varepsilon_{\mathbf{k}})$ has an explicit temperature dependence of the scattering amplitudes.

Spin structure

There are also spin indices in (2.43) and we need to work them out. Using spin relations, we work them out as in the following two equations,

$$\begin{aligned}
I &\sim \sum_{\tau,\sigma}(\vec{\tau}_{\sigma_2\sigma}\cdot \vec{\tau}_{\tau_2\tau})(\vec{\tau}_{\tau\tau_1}\cdot \vec{\tau}_{\sigma\sigma_1}) \\
&= \sum_{\tau,\sigma}\sum_{i,j}(\tau^i_{\sigma_2\sigma}\tau^i_{\tau_2\tau})(\tau^j_{\tau\tau_1}\tau^j_{\sigma\sigma_1}) \\
&= \sum_{i,j}(\tau^i\tau^j)_{\tau_2\tau_1}(\tau^i\tau^j)_{\sigma_2\sigma_1} \\
&= \sum_{k} i\varepsilon_{ijk}\tau^k_{\tau_2\tau_1} i\varepsilon_{ijk}\tau^k_{\sigma_2\sigma_1} + 3\cdot \mathbb{1}_{\tau_2\tau_1}\cdot \mathbb{1}_{\sigma_2\sigma_1} \\
&= i^2(\vec{\tau}_{\tau_2\tau_1}\cdot \vec{\tau}_{\sigma_2\sigma_1}) + 3\cdot \mathbb{1}_{\tau_2\tau_1}\cdot \mathbb{1}_{\sigma_2\sigma_1}
\end{aligned} \tag{2.47}$$

$$\begin{aligned}
II &\sim \sum_{\tau,\sigma}(\vec{\tau}_{\tau_2\tau}\cdot \vec{\tau}_{\sigma\sigma_1})(\vec{\tau}_{\tau\tau_1}\cdot \vec{\tau}_{\sigma_2\sigma}) \\
&= \sum_{i,j}(\tau^i\tau^j)_{\tau_2\tau_1}(\tau^j\tau^i)_{\sigma_2\sigma_1} \\
&= \sum_{k} i\varepsilon_{ijk}\tau^k_{\tau_2\tau_1} i\varepsilon_{ijk}\tau^k_{\sigma_2\sigma_1} + 3\cdot \mathbb{1}_{\tau_2\tau_1}\cdot \mathbb{1}_{\sigma_2\sigma_1} \\
&= -i^2(\vec{\tau}_{\tau_2\tau_1}\cdot \vec{\tau}_{\sigma_2\sigma_1}) + 3\cdot \mathbb{1}_{\tau_2\tau_1}\cdot \mathbb{1}_{\sigma_2\sigma_1}
\end{aligned} \tag{2.48}$$

In order to obtain the total contribution of the second order terms, one combines (2.45), (2.46), (2.47), and (2.48) to get the following form

$$\begin{aligned}\mathcal{T}^{(2)}_{\mathbf{k}\mathbf{k}'\sigma_1\tau_1\sigma_2\tau_2} &= -J^2 i^2(\vec{\tau}_{\tau_2\tau_1}\cdot\vec{\tau}_{\sigma_2\sigma_1})\sum_{\mathbf{k}}\frac{1-f(\varepsilon_{\mathbf{k}})}{\varepsilon_{\mathbf{k}}-i\omega'} \\ &\quad +(-)J^2(-)i^2(\vec{\tau}_{\tau_2\tau_1}\cdot\vec{\tau}_{\sigma_2\sigma_1})\sum_{\mathbf{k}}\frac{f(\varepsilon_{\mathbf{k}})}{\varepsilon_{\mathbf{k}}-i\omega'} \\ &\quad + \text{ potential scattering}\end{aligned} \tag{2.49}$$

The term in (2.49) that is independent of the temperature is termed potential scattering and will make a contribution similar to that of the first order scattering perturbation term though smaller by an order of magnitude. Consequently, more attention is paid to the term with a temperature dependence which is the first and second term of (2.49). Combining both terms, we obtain the following form

$$\begin{aligned}\mathcal{T}^{(2)}_{\mathbf{k}\mathbf{k}'\sigma_1\tau_1\sigma_2\tau_2} &= J^2(\vec{\tau}_{\tau_2\tau_1}\cdot\vec{\tau}_{\sigma_2\sigma_1})\sum_{\mathbf{k}}\frac{1-2f(\varepsilon_{\mathbf{k}})}{\varepsilon_{\mathbf{k}}-i\omega'} \\ &\quad + \text{ potential scattering; } i\omega'\to\omega'+i0^+\end{aligned} \tag{2.50}$$

We use the canonical procedure to evaluate (2.50) as a function of energy and temperature. We do an integration over the energy, ε. This is done by transforming the sum over momentum $\mathbf{k}$ into an energy integral using

$$\sum_{\mathbf{k}} \to \int d\varepsilon N(\varepsilon) \tag{2.51}$$

We consider a rectangular and constant density of states over the bandwidth D, consequently the integral becomes

$$\sum_{\mathbf{k}} = N(0)\int d\varepsilon \tag{2.52}$$

Substituting (2.52) in (2.50) one obtains

$$\begin{aligned}\mathcal{T}^{(2)}_{\mathbf{k}\mathbf{k}'\sigma_1\tau_1\sigma_2\tau_2} &= \sum_{\mathbf{k}}\frac{1-2f(\varepsilon_{\mathbf{k}})}{\varepsilon_{\mathbf{k}}-i\omega'} \\ &= N(0)\int_{-D}^{D}\frac{1-2f(\varepsilon)}{\varepsilon-\omega}d\varepsilon N(\varepsilon) \\ &= N(0)\int_{-D}^{D}d\varepsilon N(\varepsilon)\frac{\tanh(\frac{\varepsilon}{2T})}{\varepsilon-\omega} \\ &\approx 2N(0)\ln\frac{D}{D_{\max}(|\omega|,T)} \\ &\approx 2N(0)\ln\frac{D}{T}\end{aligned} \tag{2.53}$$

Where $N(\varepsilon)$ is the density of states and D is the bandwidth. The integral diverges if the bandwidth is infinite and thus sensitive to the value of D. Adding the first order value of perturbation to the above second order term, we get a full expression for the scattering amplitude as follows

$$\mathcal{T}_{\mathbf{k}\mathbf{k}'\sigma_1\tau_1\sigma_2\tau_2} = J(\vec{\tau}_{\tau_2\tau_1}, \vec{\tau}_{\sigma_2\sigma_1})[1 + 2N(0)\ln\frac{D}{T} + \dots] \tag{2.54}$$

The scattering cross section is proportional to $|\mathcal{T}|^2$ which itself is proportional to the electric resistivity $\rho(T)$ which can be written mathematically as follows

$$\rho(T) \propto 1 + 2N(0)J \ln\frac{D}{T} \tag{2.55}$$

This means that the resistivity $\rho(T)$ increases logarithmically as $T \to 0$. This also means a breakdown of perturbation theory when 2nd order is comparable to 1st order in size, that is for

$$1 = 2N(0)J\ln\frac{D}{T} \tag{2.56}$$

and

$$T_K = De^{-\frac{1}{2N(0)J}} \tag{2.57}$$

Below T_K, perturbation theory no longer works and the search for a solution in this regime became known in the literature as the Kondo problem.

2.3.4 Perturbative renormalization group method

The renormalization group (RG) was first introduced in quantum electrodynamics by Gell-Mann and Low in 1954 [25]. It was first applied in solid state physics by Abrikosov and Migdal in 1970 [26] and later on by Fowler and Zawadowski to investigate the Kondo problem infrared divergences [27]. Renormalization group is the basic idea that a change of scale, for example, of the bandwidth, D can be made up for by a corresponding change of the parameters of the physical theory such as, the exchange coupling, J. This leads to different Hamiltonians at different scales describing the physics at the respective scales. The transformation from one Hamiltonian $H(D)$ to $H(D')$ is known as the RG transformation. It should be mentioned that the RG does not form a real group since there is no inverse transformation. When this RG procedure is repeatedly applied, it leads to a family of Hamiltonians $H(D)$. The Hamiltonian H usually contains a series of dimensionless coupling constants g_i which represent the strength of interactions term in them. The scaling equation for the evolution of these coupling constants with the energy cutoff value is given by

$$\frac{\partial g_j}{\partial \ln D} = \beta_j(g_i) \tag{2.58}$$

If the β function is negative, this implies that the relevant coupling constant grows as the energy cutoff is reduced. Whereas a positive β function means an irrelevant coupling constant that decreases as the cutoff is diminished. This kind of scaling process leads to the occurrence of two types of events, namely a crossover and a fixed point. A crossover happens when the cutoff energy scale D becomes smaller than the characteristic energy scale of a particular class of high frequency excitations, then at lower energies, these excitations may only occur through a virtual process. The Hamiltonian changes its structure in order to sustain this change thereby picking up additional terms that simulate the effect of the high frequency virtual fluctuations on the low energy physics. A good example of a crossover is the passage from the Anderson model to the Kondo model. One can notice in the RG treatment of the Anderson model that, when the energy cutoff of the conduction electron band becomes smaller than the energy to produce fluctuations, then a crossover takes place in which real charge fluctuations are eliminated and the physics at lower energy scales is described by the Kondo model. A fixed point is reached if the cutoff energy scale becomes smaller than the lowest energy scale of the problem, implying there are no further changes that can occur in the Hamiltonian. This means that the Hamiltonian remains invariant under the scaling procedure. The β function of all the remaining parameters in the Hamiltonian vanishes. The attribute of the low energy physics are described by the fixed point Hamiltonian. This RG idea is a very general idea and has found applications in a variety of physical theories. Many problems in physics usually involve several energy or length scales. This kind of problems are suitable for the renormalization group method if only a finite number of operators in the Hamiltonian are generated during the RG flow. The Kondo model is an example. In order to understand why the resistivity does not diverge as the temperature approaches zero, we apply the renormalization group technique to the problem. We will start by applying the so-called poor man's scaling method introduced by P. W. Anderson [28]. The rationale behind the scaling method is that by reducing the bandwidth of the conduction electrons D, then the argument of the logarithmic divergent term will also reduce, thereby making the divergence weaker. Just a synopsis of this method will be given here since it can be found easily in almost all books on Kondo physics.

Poor man's scaling

The poor man's scaling is a method in which the evolution of the coupling constant is followed so as to keep physical quantities, like the $\mathcal{T}$-matrix invariant, as the bandwidth of the conduction band is reduced. In the case of the Kondo model, the high energy scale of D is successively removed from the physical properties. This is usually the starting point for the renormalization group method. The reason why this is done is because the physical properties do not depend on the high energy cutoff D, in particular, $\mathcal{T}(D)$ is invariant, where $\mathcal{T}(D)$ is the scattering matrix. The RG procedure is as follows
1) Reduce cutoff $D \to D - \Delta D$. This step is done by integrating out the degrees of freedom in this range as shown in Fig. 2.6.
2) Change coupling constant $J \to J - \Delta J$ such that $\mathcal{T}(D)$ is invariant.
3) Iterate these two steps.
The first two steps are the RG transformations that permit us to map the Hamiltonian $H \to H'$. The third step produces the so called RG flow. The RG equation for the Kondo coupling, J is of the form

$$\frac{dJ}{d\ln D} = -2N(0)J^2 \tag{2.59}$$

where $N(0)$ is the density of states. The detail derivation of (2.59) can be found in [29]. One can understand the consequences that result from the decrease of the bandwidth D, by integrating (2.59). The result of this integration is the following equation

$$\tilde{J}(\tilde{D}) = \frac{J}{1 + 2\rho J \ln(\tilde{D}/D)} \tag{2.60}$$

$\tilde{D}$ is the reduced bandwidth while $\tilde{J}$ is the corresponding coupling. If J is negative, then we have ferromagnetic coupling and, consequently, no divergence. In this case perturbation theory and the scaling work very well as the bandwidth is reduced. This is because the coupling gets smaller and smaller as we scale to a free impurity spin. On the other hand, if J is positive, then we have an antiferromagnetic coupling. Perturbation theory fails at some value of the bandwidth as it is reduced. In other words, we could say that perturbation theory fails at some temperature T. The temperature at which this happens is known as the Kondo temperature. It is also observed that the RG flow diverges when $\tilde{D}$ reaches the Kondo temperature T_K. This means that $\tilde{J}$ has become infinite and so perturbation theory can no longer work. T_K is a scaling invariant. This means that materials with same T_K even if they have different J, $N(0)$, and D will still have the same low-energy properties. T_K is the only relevant energy scale, which means that all temperature dependence of all observables must be universal functions of T/T_K. The divergence of J at $T = T_K$ is an artefact of the approximations made in the calculation and not the true physics. If we go to higher orders of perturbation theory in J, say the third order, then this divergence of the effective coupling $\tilde{J}$ at T_K is removed as shown by Hewson in [29]. This does not help that much since it does not change the fact that there exists a unique relation between T_K/D on the one hand and J on the other hand. K. Wilson, using the numerical renormalization group (NRG) [1], found a full solution of the RG problem, including the strong coupling regime. We will discuss this method in chapter 5.

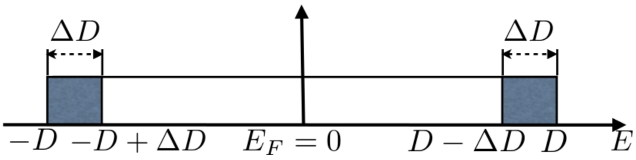

Figure 2.6: Integrating out high energies thereby reducing the Bandwidth.

2.4 Characteristics of single-channel Kondo effect

The single-channel Kondo (1CK) model has a few unique properties that can be used to distinguish it from other models. In this subsection, we look at some of these properties without getting into how they are calculated since we will handle this issue of calculation in chapter 5 using the numerical renormalization group method. We will rather concentrate on how these properties behave as the temperature turns to zero. Some of the properties that we will briefly mention here are the conductivity, specific heat, magnetic susceptibility, entropy and the Wilson ratio.

2.4.1 Fermi liquid

The Landau Fermi liquid theory provides the foundation for the understanding of how interactions between electrons in metals affect the metallic states. This theory gives the basis for understanding metals in terms of weakly interacting electrons. We will not get into the details of this theory but rather just give a brief definition and focus on the properties of the system that comes out of this theory. The basic idea behind the Fermi liquid theory as proposed by Landau is that it consists of a one-to-one correspondence between the eigenstates of the non-interacting electron gas and those of the interacting liquid [30]. P. Nozières was the first to give a Fermi liquid description of the Kondo problem at low temperatures [31]. The impurity spin is screened at low temperatures by the conduction electrons, thereby forming a singlet that scatters the other electrons. There exist weak interactions between the conduction electrons of opposite spin in the neighborhood of the impurity due to the virtual excitations of the singlet to the triplet state. The length scale of these interactions and scattering from the impurity is much larger than the distance between the electrons. The screening is done by electrons close to the Fermi energy. Therefore the impurity does not only cause the scattering of electrons but also the interactions between electrons. Since these interactions do not change at microscopic length scale, it is expected that a Fermi liquid theory should be applicable to it. The effective Fermi energy of this local Fermi liquid is set by the Kondo temperature. We look at such an assertion in the different physical properties below.

Conductivity

The low temperature conductivity of the Kondo problem increases as the temperature increases. The reason for this behavior is that as the temperature is increased, the scattering from the impurity of the conduction electrons becomes less pronounced away from the Fermi energy and so the elastic scattering from the impurity is reduced due to thermal smearing. In addition to the elastic scattering, there is the inelastic scattering since the conduction electrons are interacting thereby adding a Fermi liquid correction to the conductivity. The inelastic scattering rate in a Fermi liquid is proportional to the square of the temperature. The conductivity of this system at small but finite temperature as stated by P. Nozières is as follows

$$\sigma(T) = \sigma(0)(1 + \pi^2\alpha^2 k_B^2 T^2) \tag{2.61}$$

where k_B is the Boltzmann constant and at typical low temperature scale α can be identified with $1/k_B T_K$. The Kondo temperature T_K is the temperature scale for the change of the conductivity. The inverse of the conductivity is called the resistivity and the behavior of the resistivity is illustrated in Fig. 2.1.

Specific heat

The impurity contribution to the specific heat in single-channel Kondo model peaks near T_K as the temperature is decreased and then falls linearly to zero. The reason for this behavior again is due to spin scattering effect that becomes pronounced as the temperature is lowered. The impurity spin is quenched below T_K and so a singlet is formed. The singlet is a bound state that just acts as an inert potential scatterer, restoring the Fermi liquid.

Magnetic susceptibility

For $T > T_K$, the magnetic susceptibility of the 1CK affect increases, as the temperature is lowered, analogous to Curie behavior of a free spin. Below T_K it saturates to a constant value (Pauli susceptibility). This is because the spin degree of freedom is gradually being quenched as the temperature is lowered.

Entropy

The entropy associated with the impurity decreases as the temperature is lowered. It starts out at $S = k_B \ln 2$, since the impurity spin has two possible states in the case of the spin-1/2 single-channel Kondo model.The quenching of the impurity spin happens for temperatures of the order of T_K and S falls to $S(0) = 0$.

Wilson ratio

The Wilson ratio is the ratio of the specific heat coefficient and the Pauli susceptibility. The mathematical formula for the Wilson ratio is

$$R_W = \frac{\chi_{imp}/\chi}{c_{V,imp}/c_V} \tag{2.62}$$

χ_{imp} and $c_{V,imp}$ are the magnetic susceptibility and the specific heat associated with the impurity. This ratio characterizes the extent to which the impurity changes the interactions between the electrons. It is usually one in the case of non-interacting systems. In the case of a static impurity, the conduction electrons only have a change in the potential they feel hence their interactions are not affected. This kind of impurity only affects the density of states at the Fermi level, and since both the specific heat and the susceptibility are proportional to the density of states, the Wilson ratio, $R_W = 1$. In the case of a magnetic impurity the Wilson ratio $R_W = 2$. This is because the magnetic impurity causes interactions between the conduction electrons and since the specific heat does not change with this interactions and only the susceptibility changes hence the change of the value of the Wilson ratio with the presence of a magnetic impurity. This means that the Kondo effect leads to a Fermi liquid behavior at low temperatures. The spin compensated state of a Kondo system at low temperatures can be accounted for by the Fermi liquid theory.

Chapter 3

Two-channel Kondo problem

The 2CK effect has not ceased to amaze physicists ever since it was first proposed by Nozières and Blandin in 1980 [7] because of its exotic non-Fermi liquid ground state with a non-vanishing zero-point entropy. This effect can be observed whenever a discrete, degenerate quantum degree of freedom is exchange-coupled to two conserved flavors of conduction electrons in a symmetrical manner. The two-channel Kondo impurity model is just a particular case of the multichannel Kondo impurity models that have attracted much attention lately due to the fact that, in the overscreened case, they provide us with an unequivocal example of the non-Fermi liquid ground state. In addition, they can be studied using different types of controlled methods and supply us with great testing grounds for theoretical techniques for correlated electron systems. Lastly, they too have experimental bearing on tunneling phenomena in quantum dots as well as in two-level systems (TLS) and also on heavy fermion compounds. So far the physical realization of the 2CK has been clear only in special fine-tuned systems. In this chapter we discuss the physics of the 2CK effect with emphasis on its physical description, renormalization group analysis and some of its properties.

3.1 Physical description

The two-channel Kondo (2CK) model describes the over-screening of a local moment in the presence of two conduction electron channels. In this model, two different conserved flavors of conduction electrons are considered, which are associated with the two-channels. The two-channel Hamiltonian for a magnetic impurity has the following form

$$H_K = \sum_{\mathbf{k}\sigma\alpha} \varepsilon_{\mathbf{k}} c^{\dagger}_{\mathbf{k}\sigma\alpha} c_{\mathbf{k}\sigma\alpha} + J \sum_{\alpha=1}^{2} \mathbf{S} \cdot \mathbf{s}_{\alpha}. \tag{3.1}$$

α is the channel index which runs from 1 to 2 in the case of the two-channel model or from 1 to N in the case of the N-channel model. This model can be generalized to the case of non-magnetic impurities as will be discussed in chapter 4. (3.1) has three possible ground states when $J > 0$. If the spin of the impurity is, say S_I and the number of different channels N, then the following three scenarios can be considered:

Underscreened

In the case where $N < 2S_I$, there are not enough conduction electrons to screen the impurity spin, hence resulting in a finite local moment left behind and consequently a residual entropy as $T \to 0$. This appears to go against the third law of thermodynamics, however, in the presence of more than one impurity this violation can be taken care of. Fig. 3.1 illustrates this underscreening behavior.

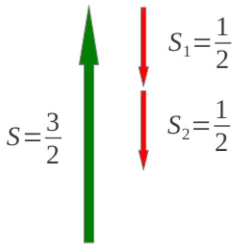

Figure 3.1: When $N < 2S_I$ the impurity spin is undercompensated resulting in a spin-1/2 left behind.

Screened

This is the situation where $N = 2S_I$, the screening of the impurity is exact and hence the ground state is a singlet. The uniqueness of the ground state at $T = 0$ causes the entropy to turn to zero as T turns to zero. Fig. 3.2 shows this underscreening behavior.

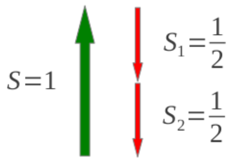

Figure 3.2: When $N = 2S_I$ the impurity spin is compensated and therefore forming a singlet.

Overscreened

The third alternative is the one in which $N > 2S_I$ so that there are more conduction electron spins than are needed by the impurity to be fully compensated hence overcompensation. There is a residual entropy as a result of an effective spin formed between the impurity and the conduction channels. In the case where $S_I = \frac{1}{2}$ and $N = 2$, then the impurity is overcompensated by the presence of two conduction electrons of spin 1/2 each. The ground state will have an effective spin of 1/2 and this will result in an anti-ferromagnetic exchange generated with the electrons off the impurity site. This idea will be dealt with explicitly in the next section where we discuss the renormalization group (RG) analysis. This overscreening behavior is shown in Fig. 3.3.

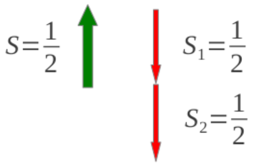

Figure 3.3: When $N > 2S_I$ the impurity spin is overcompensated, consequently an effective spin-1/2 persists.

3.2 Renormalization group analysis

In order to gain deeper understanding of the 2CK problem, we apply the RG techniques to it. This method has already been briefly introduced in chapter 2. Here, we will concentrate on what can be extracted from this model when we apply the RG method. We start our analysis by looking at how the system changes as the coupling constants flow to infinity. We are interested here in the overscreened case where the ground state is non-Fermi liquid. We will thus extend the argument already started above in the overscreened scenario. In Fig. 3.4, one can see that in the free limit, that is at the origin, there is a free spin which scatters both conduction seas of electrons and this results in a logarithmically growing scattering as the temperature is lowered. As the coupling constants J_1 and J_2 of the two channels in Fig. 3.4 grow, the impurity spin has a problem, as it does not "know" which of the channels to form a singlet with, since the symmetry of the problem forbids it from preferring one channel to another. These two-channels therefore overcompensate the impurity spin and thus lead to a three body object that has an effective spin 1/2. At this strong-coupling fixed point, an antiferromagnetic exchange is generated with electrons of the impurity site. These exchange interactions introduce kinetic energy that renders the strong-coupling ($J \to \infty$) fixed point unstable. It can be shown by second order perturbation theory that an effective coupling results at this fixed point and can be defined as follows as in [32]

$$\tilde{J} = \gamma \frac{t^2}{J}, \tag{3.2}$$

where t is the effective hybridization required for an electron to hop in and out of the impurity site, while J, is the binding energy at the impurity site, and γ is just a number whose value is 30/46 as calculated in [32]. This is because at the strong-coupling fixed point the kinetic energy of the impurity is negligible. Fig. 3.4 gives an illustration of this behavior. One can see that because of the fact that the strong coupling regime is unstable, the effective model flows back to the weak coupling limit where $J = 0$. Since the weak coupling fixed point is unstable due to the Kondo effect, this means that both strong and weak coupling limits are unstable. Therefore, there must be a non-trivial fixed point at an intermediate coupling strength. This is the red dot in the middle of the diagonal in Fig. 3.5. If one of the coupling constants J_1 and J_2 is slightly stronger, then the system will flow to the single-channel Kondo fixed point of the stronger coupling constant as illustrated in Fig. 3.4. Fig. 3.5 illustrates the stability of the 2CK fixed point, showing scaling trajectories. This non-trivial fixed point produces a ground state with non-zero entropy and has a non-Fermi liquid energy spectrum. Unlike in the compensated case mentioned above, there is a non-integer degeneracy of the ground state [5]. So there is always a residual entropy that comes from the degeneracy of the impurity. This degeneracy of the ground state can be lifted by applying a finite external magnetic field to it. In the next section, we will shed more light on some of the ideas put forth in this section.

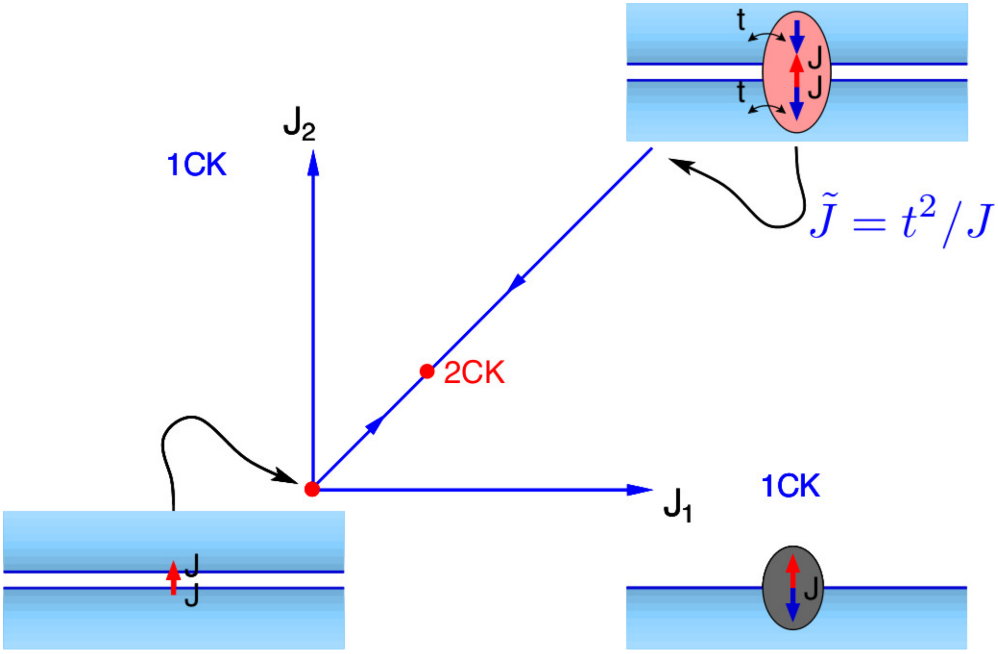

Figure 3.4: 2CK RG analysis for both strong and weak coupling constants showing the duality behavior, which is one of the characteristics of the 2CK model. The blue lines are the scaling trajectories for the case of an impurity with spin 1/2. Picture is courtesy of Johann Kroha.

3.3 Characteristics of two-channel Kondo effect

In this section, some of the properties of the 2CK that makes it different from other models are briefly explained. We will not get into the details of how some of these properties are calculated, since the perturbation theory is completely analogous to the 1CK case and these calculations can be found practically in all standard reviews on the 2CK effect, for example in [33].

3.3.1 Duality of weak and strong coupling regimes

Kolf and Kroha have shown in [32] that the 2CK effect exhibits a duality between the weak and the strong coupling regimes. They showed that the crossover scale from the weak coupling regime to the 2CK non-Fermi liquid behavior can be obtained by perturbative analysis in the coupling constants around the weak and strong coupling fixed points. With this approach the Kondo temperature for small coupling constants can be calculated using the expression

$$T_K^{(wc)} = De^{-\frac{1}{2MN(0)J}} \tag{3.3}$$

where D is the half bandwidth, M the number of conduction electron channels, $N(0)$ is a constant density of states, and J the coupling constant. From (3.3), it can be noticed that T_K increases with increase in the coupling constant. On the other hand, when the

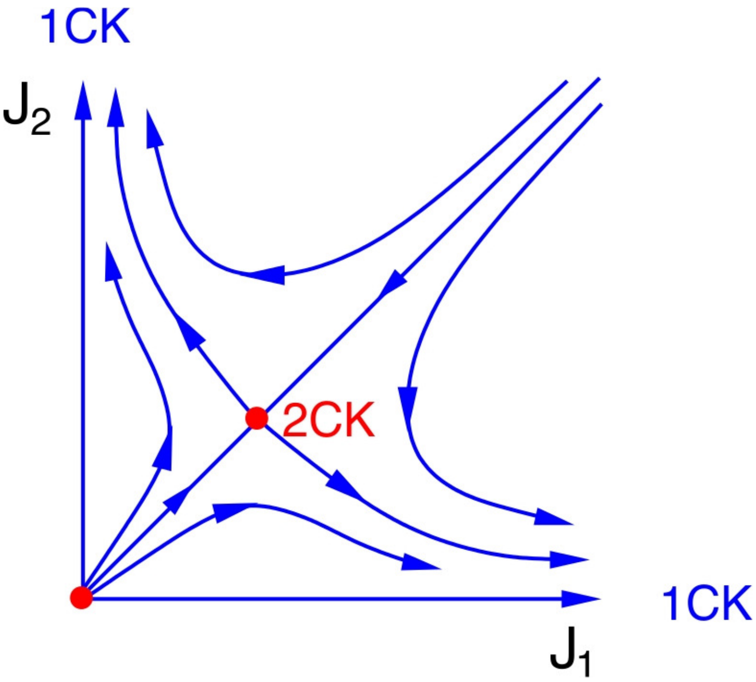

Figure 3.5: 2CK RG analysis for both strong and weak coupling constants showing the stability of the 2CK fixed point. The blue lines are the scaling trajectories for an impurity with spin 1/2. Picture is courtesy of Johann Kroha.

coupling constant is large, then by just using second order perturbation theory with the effective coupling $\tilde{J}$ as in (3.2), one gets the Kondo temperature as follows

$$T_K^{(sc)} = De^{-\frac{\gamma N(0)J}{2M}} \tag{3.4}$$

Unlike in the weak coupling regime, T_K decreases with an increase in the coupling constant as can be seen in (3.4). The duality relation in the coupling constant is of the form

$$J \leftrightarrow \frac{1}{\gamma J} \tag{3.5}$$

One can immediately see that there is a duality between the weak and the strong coupling regime as shown in Fig. 3.4. Hence the 2CK effect has an intermediate fixed point that flows from both below and above. Because of this behavior there is a mapping of the flow below and that from above. This duality is one of the properties of the 2CK and could possibly explain why no broad distribution of T_K is observed in experimental conductance anomalies of nanoconstrictions with 2CK signatures as hinted in [32]. We will come back to this duality behavior in chapter 6 when we analyze the partially broken SU(3) Kondo model. For a detailed analysis on this duality behavior see [32]

3.3.2 Non-Fermi liquid

The recent discovery of metals that apparently fall outside the framework of our conventional theory of metals has led to the new excitement in this area of physics. Non-Fermi liquid systems show physical properties which cannot be understood in terms of weakly interacting electrons, hence their low temperature behavior do not follow the power-laws in temperature that are observed in Fermi liquids. Some of the examples of these systems are metals close to a quantum critical point; this is because the scattering of quasi-particles near a phase transition is singular and, therefore, the systems no longer behave as prescribed in the Fermi liquid theory. The second example are Luttinger liquids which are one dimensional metals. The electrons in one dimensional metals are usually unstable and consequently decay into spinons and holons, spin and charge excitations, respectively. The last but not least of these non-Fermi liquid systems is the two-channel Kondo model which we have already explained above. The change of the physical properties of non-Fermi liquids with temperature are completely different from those obtained in the case of Fermi liquids. Thus, we will briefly give a few examples of the different physical properties as they vary with temperature.

Resistance

The resistivity of the 2CK effect behaves as follows

$$\rho(T) \sim 1 - c\left(\frac{T}{T_K}\right)^{1/2} \tag{3.6}$$

where c is a constant of order one. This behavior of the resistivity in the 2CK case is clearly different from the typical Fermi liquid one in which the resistivity shows a T^2 behavior [13].

Specific heat

The specific heat of 2CK impurity diverges as the temperature turns to zero. It is

$$\frac{c(T)}{T} = -\frac{A}{T_K}\ln\frac{T}{bT_K} + B \tag{3.7}$$

where A and b are constants and B is a temperature-independent crystal-field background in c/T [14].

Entropy

As the temperature decreases the entropy of the 2CK drops and at very low temperatures there is a residual entropy which is as a result of the fact that the ground state is degenerate. The expression of the entropy is normally the derivative of the free energy with respect to temperature. The derivative is as follows

$$S = -\frac{\partial F}{\partial T} \tag{3.8}$$

where F and T are the free energy and temperature, respectively. The zero point entropy is given by

$$S(0) = k_B \ln\sqrt{2} \tag{3.9}$$

This basic idea of the impurity entropy is very central to this thesis, because it gives useful information on the nature of the impurity in the partially broken SU(3) Kondo model. In the ordinary spin-1/2 2CK effect, the entropy of the impurity decreases from $\ln 2$, reflecting the two degrees of freedom of the free spin down to $\frac{1}{2}\ln 2$ at low temperatures as if a $\sqrt{2}$-fold degenerate degree of freedom were left. This object is represented by the real part of the Majorana fermion (half-fermionic excitations) and it remains free at low temperatures, consequently, disrupts the local Fermi liquid that is present in the case of the single-channel. We will see in chapter 6 that this behavior depends on the nature of the impurity and that interesting physics can be squeezed out of the model just by looking at the behavior of the impurity entropy as the temperature drops. The impurity entropy behavior is affected by the presence of a strong magnetic field, since it lifts the degeneracy of the impurity. These magnetic field effects will also be looked into in chapter 6.

Magnetic susceptibility

The magnetic susceptibility also diverges for $T \to 0$ as

$$\chi(T) \sim -\frac{1}{T_K} \ln \frac{T}{T_K} \tag{3.10}$$

The divergence of the magnetic susceptibility is due to the presence of an effective spin even at very low temperatures.

Wilson ratio

Since both the magnetic susceptibility and the specific heat diverges as $T \to 0$, to obtain the Wilson ratio, for example in the case of the numerical renormalization group (NRG) method, one fits both quantities with the logarithmic form as explained in [50]. The calculations show that the Wilson ratio of the 2CK, $R_W = 8/3$.

Chapter 4

Non-magnetic Kondo impurities in metals

Contrary to the believe in the past that the Kondo effect could only be observed in the case of magnetic impurities, it has been shown that whenever the impurity has a localized, discrete, degenerate quantum degree of freedom that exchange-couples to the conduction band electrons, the Kondo effect is manifested. Jun Kondo [34, 35] had suggested that an atom jumping between two equivalent positions in a metal is dressed by the conduction electrons and consequently may form a Kondo effect. Kondo had shown that the scattering process in which the atom changes its position has non-commutative angular dependence and that this non-commutative case leads to logarithmic contributions to the electrical resistivity. He showed that this exists even in the leading logarithmic approximation [34] and the result was obtained in fourth order approximation. Kondo then exploited the similarity between this kind of non-magnetic impurity problem and the magnetic impurities in dilute alloys. In this kind of system the role of the impurity spin is taken over by the equivalent sites of the jumping impurity, and the spin polarization in the conduction sea is replaced by the angular dependence of the screening. In the case of the non-magnetic impurity, the two-channel Kondo model results by virtue of the degeneracy of the conduction band electrons. In this chapter, we outline briefly the experimental motivation of this work, then give a synopsis of the two-level systems Kondo model and last but not least the partially broken SU(3) Kondo model which was proposed in [2], to explain all the experimental features of the Ralph and Buhrman experiments [3]. It is for reasons of space and relevance to this thesis that we will deal only with the two models mentioned above.

4.1 Experimental motivation

There have been many experimental observations of the 2CK effect signatures such as in heavy fermion compounds and in designed quantum dot systems. One of the recently most interesting observations has been those of Ralph and Buhrmann [3], in which they reported conductance anomalies in apparently simple copper point contacts. These results show one of the salient 2CK signatures near zero bias (zero-bias conductance anomalies with $\sqrt{V}$ behavior, where V is the voltage), which includes the theoretically expected scaling behavior [44, 45]. Ralph and Buhrmann suggested that many of the logarithmic zero-bias peaks seen in point contacts and tunnel junctions which can not be explained by magnetic impurities are due to the Kondo effect in two-level systems. They were however unable to fully explain the sharp features at slightly higher biases in the differential conductance especially the dependence of these transition on the magnetic field and temperature.

4.1.1 Experimental procedure

In order to have a better idea of the motivation of this work, it is necessary to give the scheme of the experimental setup as detailed in [36]. Just an outline of the experimental procedure is given here so that one can have a feeling for the physical relevance of this work. The development of the fabrication technique for nano point contacts has made it possible to study scattering in very small metal constrictions. In their experiment, Ralph and Buhrman used nano point contacts that were fabricated using electron beam lithography and reactive ion etching to form in a silicon nitride membrane a hole of diameter of about 6 nm. This was carried out in an ultrahigh vacuum and at room temperature. The membrane was then rotated to expose both sides while evaporating the metal to fill the hole and thus a metal constriction formed as in Fig. 4.1. This device is of interest because the mean free path of the electrons is much larger than the diameter of the constriction. In the copper samples they used, the mean free path was 180 nm at 4.2 K. Because of this when a voltage is applied across the constriction, there is a generation of a strongly non-equilibrium electron distribution. Since energy dependent scattering mechanisms lead to V-dependent resistance signal, this provides a means of spectroscopic studies as explained by Wolf in [37] and Duif et al. in [38]. They measured the V-dependent differential conductance curve for the unannealed copper nanobridge.

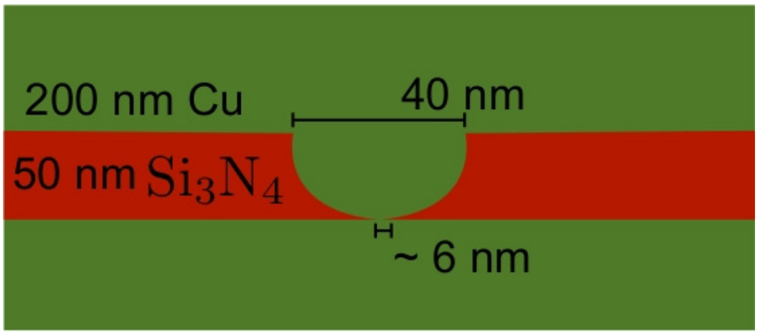

Figure 4.1: The cross-section of metal point contact. The very small constriction at the lower side of silicon nitride determines the region over which an applied voltage drops [39].

4.1.2 Experimental result

The results they obtained for the differential conductance fall in the domain of zero-bias anomalies (the minimum of resistance at zero bias) that have long been observed in point contacts [40] and tunneling devices [37]. They noticed that a dramatic and unanticipated effect occurs away from zero bias in the unannealed copper samples. These were spikes in the differential conductance. Furthermore, they observed that this spike appears in V-symmetric pairs and occurred only on samples which also show a zero-bias dip in the conductance as shown in Fig 4.2. They also observed that these signals were similar to those resulting from Kondo scattering from magnetic impurities in the absence of an applied magnetic field. They noted that the magnetic field dependence of their results shows that the source of the scattering is from non-magnetic impurities. These results, as already highlighted in the introductory part of this section, led to the introduction of various theoretical models to explain all the experimental features of these results, as will be seen in the next section.

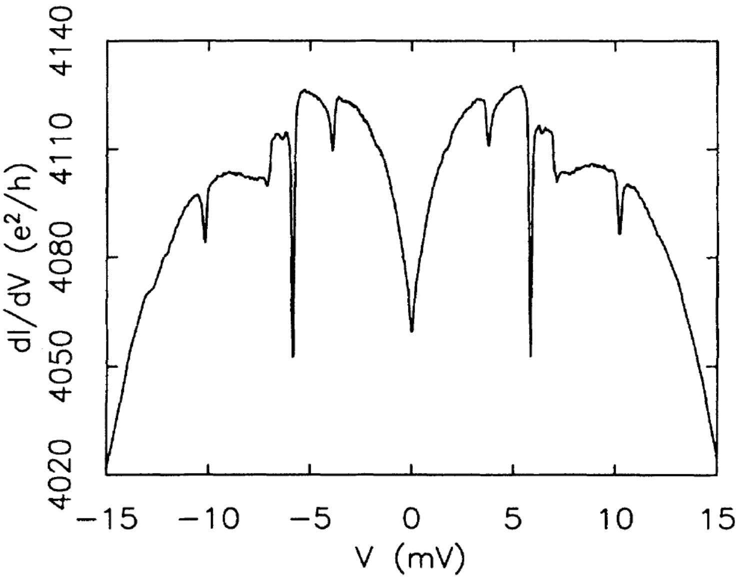

(a)

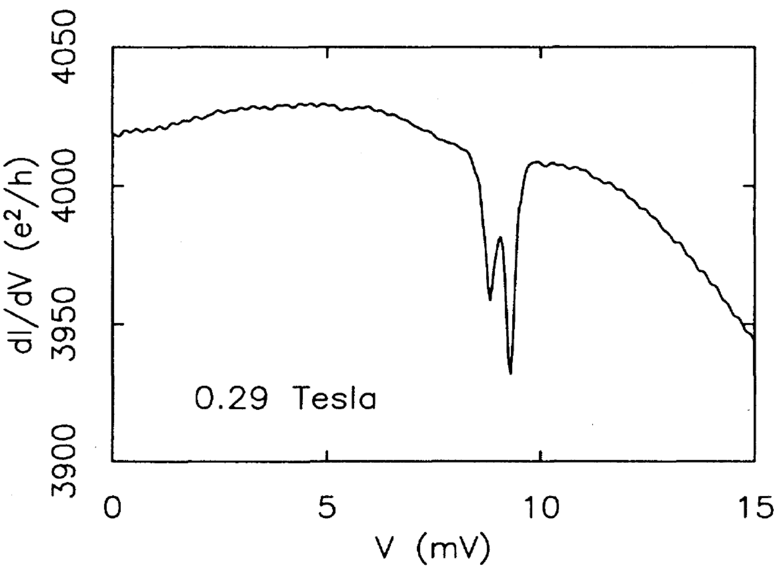

(b)

Figure 4.2: Differential conductance of a copper nano-constriction versus voltage [3].

4.2 Models

In this section we discuss the models that attempt to explain the experimental features of Ralph and Buhrman's experiment. We start with the two-level system Kondo model that explains the zero bias anomalies but has the limitation that it can not explain the magnetic field and temperature dependence of differential conductance at higher bias. Then we move on to the partially broken SU(3) Kondo model which explains all the experimental features of the Ralph and Buhrman's experiment as detailed in [2].

4.2.1 Two-level systems

Two-level systems (TLS) were motivated by experiments like point contact spectroscopy [41]. Simply put, a TLS is a system that has two possible states. Examples of such systems are the spin-1/2 particle such as an electron, in which its spin can have values of $+1/2$ or $-1/2$ in units of $\hbar$ (Planck constant divided by 2π), and a particle that sits in one of the two minima of a double-well potential and tunnels between them. The particle in the double well could be an atom, an ion, an electron, a proton or a muon. The degree of freedom here is the positions of the atom in the well either left or right. TLS have been proposed by Vladár and Zawadowski [42] as a model to explain Kondo signatures in measurements of the resistivity in disordered materials without magnetic impurities. In the following we will consider this somewhat more closely.

Physical description

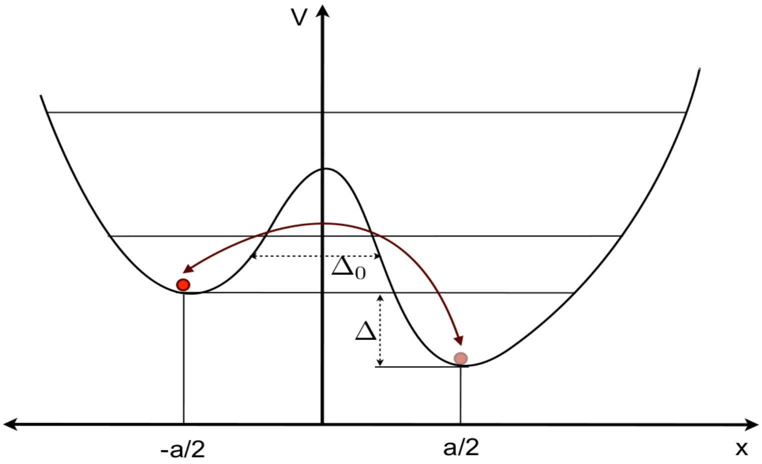

Figure 4.3: TLS in which Δ_0 is the tunneling rate between the two minima while Δ is the energy splitting between the two positions.

Fig. 4.3 shows the TLS in which an atom sits in one of the two wells. The center of the two wells is separated by a displacement vector $\vec{a}$. The lines are the localized levels of each well. The next excited level has energy which is above the barrier and so is not localized in either of the wells. To draw an analogy of this system with that of the usual spin-1/2 Kondo model, the spin flipping in this case is the tunneling of the particle between the wells assisted by the electrons in the conduction band. There are generally two types of TLS, namely, slow TLS and fast TLS [43] where the tunneling time is longer or shorter than the coherence time, respectively. Vladár and Zawadowski had interpreted the signatures close to zero bias and the enhanced conductance in Ralph and Buhrman's experiment as a result of the presence of fast TLS [42].

Two-level system Hamiltonian

The TLS Hamiltonian is given by

$$H_{TLS} = \sum_{\mathbf{k},\sigma} \varepsilon_{\mathbf{k}} c^{\dagger}_{\mathbf{k}\sigma} c_{\mathbf{k}\sigma} + \frac{1}{2} \sum_{n=x,y,z} \Delta^n \tau^n + \frac{1}{N} \sum_{\mathbf{k},\mathbf{k}',\sigma} [V^0_{\mathbf{k},\mathbf{k}'} c^{\dagger}_{\mathbf{k},\sigma} c_{\mathbf{k}',\sigma} + \sum_{n=x,y,z} V^n_{\mathbf{k},\mathbf{k}'} \tau^n c^{\dagger}_{\mathbf{k},\sigma} c_{\mathbf{k}',\sigma}], \quad (4.1)$$

where the first term represents the kinetic energy in which $c^{\dagger}_{\mathbf{k}\sigma}$ ($c_{\mathbf{k}\sigma}$) creates (annihilates) electrons in the conduction band with wave vector $\mathbf{k}$ and real magnetic spin σ while $\varepsilon_{\mathbf{k}}$ is the excitation energy of the free electron measured from the chemical potential. The second term is the atomic degree of freedom of the TLS where τ^n are the Pauli matrices for $n = x, y, z$. The energy splitting between the two wells is represented by Δ^z and the other Δ components are the tunneling matrix elements responsible for spin flip with no help from other excitations. The y-component of Δ vanishes when the wave function of the atom in the two wells is real. Consequently, $\Delta^z = \Delta$, $\Delta^x = \Delta_0$, and $\Delta^y = 0$. The third and fourth terms represent the interactions between the TLS and conduction electrons. The third is just a potential scattering term and of little importance for the Kondo physics unless the total scattering strength is large as explained in [46], whereas the fourth term is the one responsible for the screening of the TLS by electrons of the conduction sea due to the scattering of these electrons from the atom in either of the minima when $V^n = V^z$. This term is also responsible for electron scattering that induces transitions between the two minima when $V^n = V^{x,y}$, and this is known as electron assisted tunneling. It should be mentioned that the real spin σ is conserved in the coupling of the TLS but plays the role of the channel flavor in connecting the TLS problem to the 2CK model.

Merits and demerits of the two-level system

Since the suggestion of the model based on TLSs by Anderson et al. [47] and Phillips [48], the TLSs have been able to successfully explain thermal conductivity in disordered solids which cannot be described by phonon excitations as well as the low-temperature behavior of specific heat [49]. In spite of all its merits, the TLS fails to explain some of the features in Ralph and Buhrman's experiment, which are the signatures that occur at non-zero bias. It was shown by Aleiner, Altshuler, Galperin, and Shutenko [17] that, for 2CK physics to occur in TLS, the energy splitting must be small as compared to the Kondo temperature. This is not generally the case. This result put a serious dent on hopes of the TLS being a realistic model for the 2CK. Taking into account the above-mentioned shortcomings of the TLS, it was necessary to continue the search for a realistic model for the 2CK model. It is in this light that we talk about the partially broken SU(3) Kondo model in the next section which takes care of the essential deficiencies of the TLS.

4.2.2 Partially broken SU(3) Kondo model

In this section we present the model that is investigated in this thesis which is the partially broken SU(3) Kondo model. The partially broken SU(3) Kondo model is a quantum impurity model consisting of three local orbitals embedded in a metal with partially broken SU(3) symmetry. That is, two of the local levels are degenerate, while the third one is split off by a level spacing Δ_0, and conduction electron scattering off the impurity may induce transitions between any of the three local orbitals. This model has been proposed in [2] as a physical realization of the 2CK effect and may be realized physically by an ion, e.g., a proton, bound in an interstitial space of a copper fcc host lattice. In this system, the three impurity levels are formed by the unique ground state with orbital angular momentum $m = 0$ and an excited doublet of angular momentum states $m = -1, +1$ which is degenerate due to mirror symmetry (parity) of the host lattice, see Fig. 4.4(a) and Fig. 4.4(b). We neglect higher excited angular momentum states that result from higher Brillouin zones. In this model the Kondo degrees of freedom are the degenerate excited doublet $m = -1, +1$. This excited doublet is accountable for the pseudospin-flip processes, that is the transitions between the lattice angular momentum of the impurity and that of the conduction sea electrons. The magnetic spin of conduction sea electrons are conserved after scattering in our model due to the fact that the impurity in this model is non magnetic. As a result of this, the magnetic spin of the conduction electrons serve as the channel or flavor index in this model. Therefore, two channels result naturally because of the degeneracy of the conduction electrons magnetic spin.

The obvious problem with our model is that the degenerate states are not the ground states. This means that at low temperatures these degenerate states are frozen out and only the unique ground state is left behind in the case of the isolated impurity, hence Kondo physics cannot occur. However, when interactions are incorporated into the model, they have the effect of lowering the energy of the excited doublet. It has been shown by Arnold et al. in [2], that when the renormalization group (RG) scheme is applied to this model, one sees that the excited doublet are renormalized downward in such a way that a crossover occurs in which the degenerate states becomes the ground states. A degenerate ground state is a necessary condition for resonance scattering to happen and thus Kondo physics.

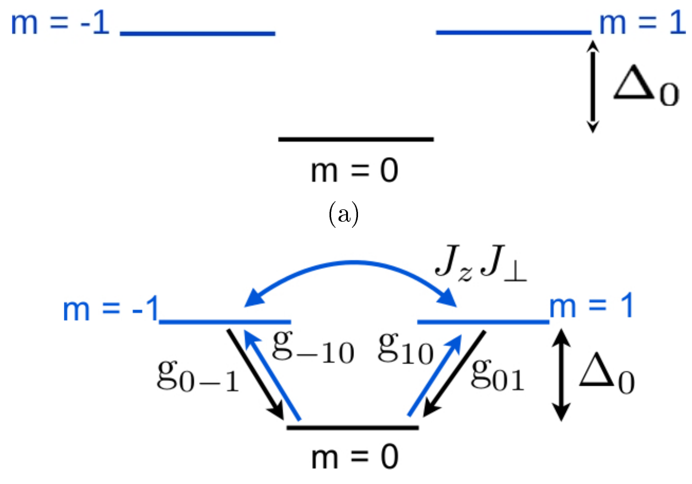

(a)

(b)

Figure 4.4: (a) Level scheme of the SU(3) impurity, (b) Definition of the coupling constants of the local level transitions.

The Hamiltonian

The partially broken SU(3) Kondo model Hamiltonian is defined as follows [2],

$$\begin{aligned}\mathcal{H} &= \sum_{\mathbf{k}\sigma m} \varepsilon_{\mathbf{k}} c^{\dagger}_{\mathbf{k}\sigma m} c_{\mathbf{k}\sigma m} + \Delta_0 \sum_{m=\pm 1} f^{\dagger}_m f_m \\ &\quad + \sum_{\sigma} \left[\frac{1}{2} J_z \, S_z s^{\sigma}_z + J_{\perp} \left(S_{1,-1} s^{\sigma}_{-1,1} + S_{-1,1} s^{\sigma}_{1,-1} \right) \right] \\ &\quad + \sum_{\sigma} \sum_{\substack{m,n=-1,1 \\ n-m \in \pm 1}} \left[g^{(n)}_{m0} \, S_{m,0} s^{\sigma}_{n-m,n} + H.c \right] \\ &\quad + \sum_{\sigma} \sum_{m \pm 1} 2 g^{(0)}_{mm} S_{m,m} s^{\sigma}_{0,0} \end{aligned} \tag{4.2}$$

Here the first term is the conduction electron kinetic energy, the second one is the degenerate local doublet with the level spacing Δ_0 above the impurity ground state $m = 0$. The third, fourth, fifth, and sixth terms describe the interactions between the impurity ion and the electrons of the conduction band. These are the transitions between the local levels induced by the conduction electrons scattering, where the capital $S_{m,n}$ operators denote the SU(3) generators in the impurity Hilbert space and lower-case $s_{m,n}$ operators denote the generators of SU(3) in the conduction electron Hilbert space. The transitions due to the unbroken SU(2) symmetry in the degenerate subspace of excited levels $m = \pm 1$ are written explicitly as the third and forth terms in (4.2). The coupling constants J_z, $J_{\perp}$, and $g^{m_i}_{m_f m_i}$ are defined in Fig. 4.4(b).

The coupling constants J_z, $J_{\perp}$, are responsible for the downward renormalization of Δ_0 and therefore play a great role in order for the Kondo effect to be manifested. This is because the couplings J are in charge of resonance scattering of the degenerate states $m = \pm 1$. The couplings $g^{n_i}_{m_f m_i}$ are accountable for the ground-to-excited states transitions and potential scattering in this model and, therefore, have counter effects to the Kondo effect. The subscripts in $g^{n_i}_{m_f m_i}$ simply indicate that the impurity scatters from an initial state m_i to a final state m_f whereas the superscript n_i is the initial state of the conduction electron. The fact that only transitions in which angular momentum is conserved are considered, makes it possible to directly deduce the final state of the conduction electron if the other three states are known. The ground-to-excited states scattering terms are the terms in which the initial state in the coupling $g^{n_i}_{m_f m_i}$ is different from the final state. In the case where $m_f = m_i$, we have potential scattering. The effect of Δ_0 to the Kondo effect is pretty straight forward. Large values of Δ_0 makes it difficult for the Kondo effect to be realized whereas smaller values make it easier, of course depending on the other couplings. Detailed studies of how these different coupling interfere with the Kondo effect is dealt with in chapter 6.

It is important to note that the defect dynamics is subject to the following constraint which projects onto the physical Fock space in which the impurity states are singly occupied, $\hat{Q} = \sum_{m=0,\pm 1} f^{\dagger}_m f_m = 1$, where $f^{\dagger}_m$ (f_m) is the creation (annihilation) operator for the impurity in the different states labeled by m as mentioned above.

Merits of the partially broken SU(3) Kondo model

We are already aware of the shortcomings of the TLSs as detailed above. Unlike the TLSs, the partially broken SU(3) Kondo model always have a degenerate level which is necessary for the Kondo effect to manifest. The Kondo temperature is not reduced by charge screening effects [19]. This is because in this model the Kondo screening happens due to space-inversion symmetric roton doublets which alters the phase but not the charge distribution of the system. This implies that the charge density and Kondo degree of freedom are independent unlike in the case of the TLS where this spatial charge distribution is coupled to the Kondo degree of freedom. Therefore, in this model the Kondo temperature T_K is not affected by charge screening. Another advantage of this model is that for 2CK effect to be observed one does not need transitions through higher excited states in order to make T_K larger than the energy of the excited doublet. This enhancement of T_K over the level splitting is inhibited by the alternating parity of the higher excited states [17]. The reason why the partially broken SU(3) Kondo model do not need the T_K enhancement is because its excited-state doublet is degenerate by space inversion symmetry. This means that two 2CK behavior in this model can be interrupted only if the space inversion symmetry is broken, for instance, by lattice distortion or by applying a strong magnetic field to it.

Chapter 5

Numerical renormalization group method

Our main goal in this chapter will be to give a brief description of the numerical renormalization group (NRG), which is a non-perturbative technique first invented by K. Wilson in the 70's to solve the Kondo problem [1]. It has since been extended to solve generally other quantum impurity problems [50]. The NRG was initially conceived for magnetic impurity systems, where the degree of freedom of the impurity is the magnetic spin. While Wilson is credited for inventing the NRG method and applying it to the single-channel Kondo model, Cragg et al. [8] was the first to apply the NRG to the more exotic two-channel Kondo model and provided the first confirmation of the non-trivial fixed point that Noziéres and Blandin had earlier proposed [7]. Cragg's calculations were done with strong bare coupling values that were all isotropic. Later on Pang and Cox [9] did a more comprehensive calculation using a wider parameter range that permitted for the first time to see transitions from weak coupling to strong coupling regimes in both isotropic and anisotropic cases. We only give a synopsis of the NRG method here, while the details on the method are discussed in the appendix.

5.1 Numerical renormalization group strategy

In this section we present the essential steps and tricks of the numerical renormalization group method to solve the quantum impurity problem.

5.1.1 Logarithmic discretization of the conduction band

The logarithmic discretization was conceived by Wilson to reflect the exponentially small energy scale evident in the behavior of perturbation theory for the Kondo problem. The basic idea of the NRG is to discretized the conduction band of bandwidth $2D$ logarithmically [1] via a discretization parameter Λ ($\Lambda > 1$). The logarithmic discretization of the conduction band $[-D < \varepsilon_k < D]$ in energy, that is a division into intervals $D^+ = [\Lambda^{-(N+1)}, \Lambda^{-N}]$ and $D^- = [-\Lambda^{-N}, -\Lambda^{-(N+1)}]$ for positive and negative parts respectively. The conduction band is logarithmically discretized because the impurity couples to all energies. Details on this discretization scheme can be found in the appendix A.

5.1.2 Mapping onto a semi infinite chain

In order to make the logarithmically discretized conduction band part of the Hamiltonian numerically treatable, it is necessary to convert it into a tridiagonal form. This can be achieved by applying the tridiagonalization procedure proposed in [51], which is known in the literature as the Lanczos procedure. A brief outline of the Lanczos procedure is given in appendix A. The Kondo Hamiltonian now has the following form

$$H_K = J\mathbf{S_d}\cdot\mathbf{s_0} + \sum_{N=0,\sigma}^{\infty}[\epsilon_N c^{\dagger}_{N\sigma}c_{N\sigma} + t_N(c^{\dagger}_{N\sigma}c_{N+1\sigma} + c^{\dagger}_{N+1\sigma}c_{N\sigma})] \tag{5.1}$$

with $\mathbf{s_0} = c^{\dagger}_{0,\sigma}\vec{\sigma}_{\sigma\mu}c_{0,\mu}$ and the localized Wannier state generated by $c_{0,\sigma} = \sum_k c_{k,\sigma}$, where the electronic impurity is replaced by a localized spin-1/2 described by the spin operator $\mathbf{S_d}$. $c^{\dagger}_N$ is the operator that corresponds to the $N-th$ site of conduction sea part of the chain whereas ϵ_N and t_N are the chain parameters for the on-site energies and the hopping matrix elements, respectively. Wilson considered a flat conduction band which means $\epsilon_N = 0$ and

$$t_N = \frac{1}{2}(1+\Lambda^1)\Lambda^{-N/2}\frac{1-\Lambda^{-N-1}}{\sqrt{(1-\Lambda^{-2N-1})(1-\Lambda^{-2N-3})}}. \tag{5.2}$$

5.2 Iterative diagonalization

It is at this point that the renormalization group (RG) character of the method gets involved. All the above transformations were necessary to get the Hamiltonian into the right form, that is, the semi-infinite chain in which the coefficients fall off exponentially as one moves along the chain. This falling off along the chain is a necessary ingredient for the iterative diagonalization. For details of the iterative diagonalization, see appendix A.

5.2.1 Renormalization group transformation

A renormalization group transformation relates effective Hamiltonians on successive energy scales $\Lambda^{-N/2}$ and $\Lambda^{-(N+1)/2}$. It is convenient to rescale the Hamiltonian directly by defining $H_N = \tilde{H}_N/D_N$ where $D_N = D\Lambda^N/2$ is the bandwidth in the $N-th$ iteration. One can relate H_N to H_{N+1} through the recursion relation

$$H_{N+1} = \Lambda^{1/2}H_N + \sum_{\sigma}(c^{\dagger}_{N,\sigma}c_{N+1,\sigma} + H.c) \equiv \Re[H] \tag{5.3}$$

This transformation is exact up to the discretization error associated with Λ. If one were to treat subsequent H_N by numerical diagonalization, the memory and work needed would increase exponentially because the number of degrees of freedom grow by a factor of four in the spin-1/2 impurity single-channel case at each step. Wilson suggested to keep only a certain number of the lowest lying eigenstates of H_N at each step.

5.2.2 Application of symmetries

The use of symmetries in the NRG is very important because it helps to reduce the dimension of the Hamiltonian matrices to be diagonalized by separating them into block matrices [52]. The symmetries do not only improve on the efficiency (speed and memory) of the NRG calculations but they also avoid the situation where numerical round-off errors induce accidental symmetry breaking. If this accidental symmetry breaking is significant, then this could lead to faulty results. Both discrete symmetries such as parity or particle-hole symmetries and continuous symmetries such as SU(2) and U(1) symmetries are considered. The discrete ones are factored in by projecting basis states to the invariant subspaces with well defined parity or particle-hole quantum number using suitable projection operators. The continuous ones are factored in by constructing the basis states using Lie group representation theory in particular the Clebsch-Gorden coefficient and the Wigner-Eckart theorem. By taking into account all the symmetries of a model we make a formerly intractable problem tractable on the computer. For details on how the basis construction of the U(1) symmetry is done in our NRG calculation, see appendix C.

Spin symmetry

It is possible in an isotropic model to employ the SU(2) group for spin rotations and use the S_z component and the total spin S^{tot}. The S^{tot} and S_z^{tot} both commute with the Hamiltonian and, consequently are conserved quantities. When a magnetic field is applied, the spin SU(2) symmetry is broken, while the U(1) resulting from S_z is unaffected, as long as the field is in the same direction as the S_z. The U(1) from S_z is broken when there is another magnetic field in the x or y direction and also when there is the chance for spin-flip processes along the chain [33]. The total S_z component is,

$$S_z = \sum_{n=1,\sigma,\alpha}^{\infty} \sigma f^{\dagger}_{n,\sigma,\alpha} f_{n,\sigma,\alpha} + S_z^{imp} \tag{5.4}$$

where N, α, and σ, are the number of electrons, the number of channels that exchange-couple to the impurity, and the magnetic spin, respectively. S_z^{imp} is the z-component of the total spin of the impurity.

Charge symmetry

Since electrons are neither annihilated nor created by the Hamiltonian, this implies that the total charge of the system remains unchanged. The total charge is therefore a good quantum number. The U(1) charge operator on the impurity is as follows

$$Q = \sum_{n=1,\sigma,\alpha}^{\infty} (f^{\dagger}_{n,\sigma,\alpha} f_{n,\sigma,\alpha} - 1) \tag{5.5}$$

The subscripts in (5.5) are the same as in (5.4) and $f^{\dagger}_{n,\sigma,\alpha}$ ($f_{n,\sigma,\alpha}$) is fermionic creation (annihilation) operator, respectively.

5.2.3 Numerical scheme

Here we present the numerical renormalization group method algorithm which is as follows:
1) The Hamiltonian H_N is numerically diagonalized using optimized standard routines from the LAPACK library [53] and the lowest eigenvalues and corresponding eigenvectors are retained.

2) The eigenvectors from 1) are used to transform all relevant operators on the N-site system to the new basis. This is achieved through similarity transformation using the BLAS library routines [54].
3) H_{N+1} is formed from H_N using the following relation

$$H_{N+1} = \Lambda^{1/2} H_N + \sum_{\sigma} (c^{\dagger}_{N,\sigma} c_{N+1,\sigma} + h.c.),$$

that is adding a site to the chain H_{N+1} in the expanded product basis.
4) Process 1) to 3) is repeated, replacing H_{N+1} with H_N until when the lowest lying spectrum of eigenvalues for successive H_N is unchanged.
This process is illustrated schematically in Fig. A.3 in appendix A.

5.2.4 Renormalization group flow and fixed Points

The behavior of the system can be understood by searching for the fixed points. In the case of the single-channel Kondo problem, both fixed points are found for $J = 0$ and $J = \infty$. At $J = 0$ the impurity is decoupled from the conduction band and the excitation energies are those from the non-interacting tight binding band extending from 0 to N. For $J = \infty$ the impurity forms an infinitely tightly bound singlet with the site 0 of the tight binding chain. The excitation energies relative to the ground states are therefore of a chain extending from 1 to N. The nature of the spectrum depends on whether N is even or odd. We notice that the strong coupling fixed point is stable, because it has no relevant operators while that of the weak coupling fixed point is unstable, because it has relevant operators. From the output of our code we can notice that the renormalization group flows from the unstable $J = 0$ fixed point to the stable fixed point $J = \infty$.

5.3 Computation of physical properties

In this subsection we look at how the different physical properties of the Kondo model can be calculated. The physical properties of a system are properties that can be measured and whose values describe the state of the system. We will show how to calculate static thermodynamic quantities such as susceptibility, heat capacity, and entropy. Beside computing the thermodynamic quantities, we will also show how to calculate more elusive dynamical quantities such as the spectral function, which is a quantity that makes it very easy to interpret experimental results.

5.3.1 Thermodynamic properties

As mentioned above we look at the static thermodynamic quantities like the entropy, specific heat, and charge susceptibility of the Kondo model. These quantities can easily be calculated once we have the energy spectrum of the system. With the energy spectrum we can calculate the partition function Z. As we know from statistical physics, once we have the partition function we can calculate all other thermodynamic properties of a given system. The truncation of the Hamiltonian does not affect the calculation of thermodynamic properties as long as the energies thrown away are of values much higher than $k_B T$ above the ground state. This is because theses energies are suppressed exponentially. In general the contribution of the impurity to the thermodynamic quantities is what we are interested in and this can be derived from the impurity free energy $F_{imp} = -\beta \ln(Z/Z_{cb})$, where $\beta = (k_B T)^{-1}$ and Z_{cb} is the partition function of the non-interacting system, where *cb* stands for the conduction band. The partition function is defined as follows

$$Z_N(T) = \mathrm{Tr}\, e^{-\beta H_N} = \sum_i e^{-\beta E_i^N} \tag{5.6}$$

where N is the iteration number in the NRG scheme.

Entropy

The entropy can be obtained in thermodynamics from the relationship $E = F + TS$ where E is the energy, F the free energy, T the temperature, and S the entropy. From this expression one can get that

$$\frac{S}{k_B} = \frac{E - F}{k_B T} = \beta E - \beta F = \beta E + \ln Z, \tag{5.7}$$

where the energy is defined as

$$E = \langle H \rangle = \frac{\mathrm{Tr}(H e^{-\beta H})}{\mathrm{Tr}\, e^{-\beta H}}. \tag{5.8}$$

Specific heat

One can obtain the specific heat from the second derivative of the free energy. The specific heat is a very interesting quantity experimentally, the specific heat due to the impurity can be calculated in the NRG method using the following equation

$$C_{imp} = C_{total} - C_{cb} \tag{5.9}$$

C_{total} denotes the specific heat of the composite system (impurity and conduction band) while C_{cb} is that of the conduction band without the impurity. C_{total} and C_{cb} are calculated as follows

$$\frac{C_l(T)}{k_B} = \frac{\beta^2}{Z} \left(\sum_i E_i^2 e^{-\beta E_i} - (\sum_i E_i e^{-\beta E_i})^2 \right) \tag{5.10}$$

where the subscript l could either be *total* or *cb* and E_i are the eigenenergies of the system.

Susceptibility

The magnetic susceptibility can be calculated using the formula,

$$\chi_{imp}(T) = \beta (g\mu_B)^2 \left(\frac{1}{Z} \sum_i S_{z,i}^2 e^{-\beta E_i} - \frac{1}{Z_{cb}} \sum_i S_{z,cb,i}^2 e^{-\beta E_i} \right) \tag{5.11}$$

g is the electronic gyromagnetic factor, S_z the z-component of the total spin, and μ_B is the Bohr magneton. Z is the partition function of the combined system, impurity and conduction electrons. The contribution of the impurity to the susceptibility of the system is obtained in the preceding equation. The first term represents the combined system while the second one is just that of the conduction electron.

5.3.2 Dynamical properties

The importance of the dynamical properties cannot be overemphasized, considering that in many experiments transport quantities are measured instead of thermodynamic quantities. The calculation of the spectral function was the first chief extension of the NRG in calculating dynamical properties [55, 56]. Some examples of dynamical properties are local single-particle spectral function, dynamical spin susceptibility, and charge susceptibility. One can also use the dynamical properties to distinguish between inelastic and elastic contributions to the cross-section of scattering. The above quantities can be calculated both at zero and at non-zero temperatures. As examples for the dynamical properties in this section we will propose the spectral function and the dynamical spin susceptibility.

Spectral function

The spectral function is the most experimentally interesting quantity. It is the energy resolution for a particle in a given quantum state. The spectral function gives an indication of how well the excitation created by adding a particle in a quantum state can be described by a free non-interacting particle. The spectral function for non-interacting free electrons is usually a delta function whereas that for interacting systems differs from a delta function but may still be a peak function. The impurity spectral function is defined as follows

$$A_\sigma(\omega, T) = -\frac{1}{\pi} Im G_\sigma(\omega, T). \tag{5.12}$$

One can immediately see from the preceding equation that, the spectral function is defined in terms of the imaginary part of the Green's function G. ω and T are the frequency and temperature respectively, while $G_\sigma(\omega, T)$ denotes the retarded impurity Green's function defined as

$$G(t) = -i\theta(t)\langle [d(t), d^\dagger(0)]_+ \rangle, \tag{5.13}$$

where $\theta(t)$ is the Heaviside function which is 0 for all variables less than zero and 1, when otherwise, while t is the time. $d_\sigma^\dagger(0)$ and $d_\sigma(t)$ are the ordinary fermionic operators in which an electron is created at time zero and destroyed at time t, respectively. $d_\sigma(t) = e^{i\hat{H}t} d_\sigma(0) e^{-i\hat{H}t}$ in the time evolution picture which is the Heisenberg representation, where $\hat{H}$ is the Hamiltonian operator. For finite systems and arbitrary temperatures it is convenient to write the retarded Green's function in the Lehmann's representation as follows

$$A_N(\omega, T) = \frac{1}{Z_N(T)} \sum_{n,m} |\langle n|d_\sigma^\dagger|m\rangle|^2 (e^{-\beta E_n} + e^{-\beta E_m}) \delta(\omega - (E_m - E_n)) \tag{5.14}$$

The spectral function at $T = 0$ is easy to calculate as compared to its non-zero temperature counterpart and is defined as

$$A_N(\omega, T = 0) = \frac{1}{Z_N(0)} \sum_n |\langle n|d_\sigma^\dagger|0\rangle|^2 \delta(\omega - E_n + E_0) + |\langle 0|f_\sigma^\dagger|n\rangle|^2 \delta(\omega + E_n - E_0) \tag{5.15}$$

E_0 is the ground state energy whereas E_n is the energy of the $n - th$ excited level. In the zero temperature case all transitions are from the ground state $|0\rangle$ to the excited states. The data we obtain from the above formula is discrete because it is just a set of positions and δ-function weights. To compare this result with continuous experimental spectra results, we need to broaden them [57]. This broadening can be done using functions like the Gaussian or the logarithmic Gaussian distributions which have widths comparable to that of the conduction bandwidth. We do not give any details of this broadening in thesis since no direct use is made of it. It is only mentioned here in order to give a complete picture of what can be obtained using the NRG technique.

Spin susceptibility

This is the response of a system to an applied magnetic field. The spin susceptibility is given in linear response theory as follows

$$\chi(t) = -i\langle\psi_0|\hat{T}S^z_{imp}(t)S^z_{imp}(0)|\psi_0\rangle \tag{5.16}$$

where $\hat{T}$ is the time ordering operator. Like in the case of the spectral function it can also be expressed in the Lehmann representation. The expression in the simple case of $T = 0$ is defined as

$$\chi(\omega) = \pi\sum_n |\langle n|S^z_{imp}|0\rangle|^2\delta(\omega - (E_n - E_0)) \tag{5.17}$$

The spin susceptibility calculated above is then broadened so it can be compared to experimental results.

5.4 Numerical renormalization group results analysis

In this section we look at the basic NRG output which are the eigenvalues of the system and discuss all the physics that one can deduce from it. Unlike in real space renormalization group where the behavior of the system is described in terms of the flowing coupling constants, in the NRG, the behavior of the system is followed in terms of the lowest lying eigenvalues. We will first look at the spectra of single-channel Kondo model numerical renormalization group calculation and then move on to the more complicated two-channel Kondo model.

5.4.1 Single-channel Kondo effect spectra

The spectra for 1CK for an odd number of shells differs from that of an even number of shells [33]. So generally we obtain a spectra that has an odd-even alternation. The reason to account for this is that, whenever we have an even number of shells, there are odd number of electrons and vice versa. With this we notice that the Fermi level passes through the gap above a non-degenerate Fermi sea. The finite size of the impurity makes it possible to define asymptotic scattering states which are responsible for the even-odd effect. This explains why we obtain a simple effective Hamiltonian to describe the fixed point. One can clearly see the crossover from one fixed point to another in the 1CK spectra. The crossover in the case of even iterations occurs at large iteration numbers to look like the spectra for small, odd iteration numbers. On the other hand for the case of the odd iteration crosses over at larger iteration number to look like the spectra for small even iteration number. This crossover scale can be quantified with the Kondo temperature T_K. Another property of the 1CK spectra is the constant level spacing of the levels. The reversal of the spectra for even and odd iteration shows that there is a uniformity of the level spacing and consequently a one-to-one correspondence between the large iteration even spectra to that of small iteration odd spectra and vice versa. This means that the low temperature spectrum is a Fermi liquid. Because electrons merely decouple from the impurity at high temperature, hence the high temperature spectrum is that of a Fermi gas. It could be summarized by saying that there is a $\pi/2$ phase shift between the even and odd iterations. This $\pi/2$ phase shift means that a bound state has been formed between the impurity and an electron of the conduction sea. The NRG energy flows for the spin-1/2 1CK model are given in Fig. 5.1(a) and Fig. 5.1(b). This calculation was carried out at zero temperature and convergence was reached after about 25 iterations. The number of states kept for this calculation was 512 and both the U(1) charge and the z-component of the total spin symmetries were made used of.

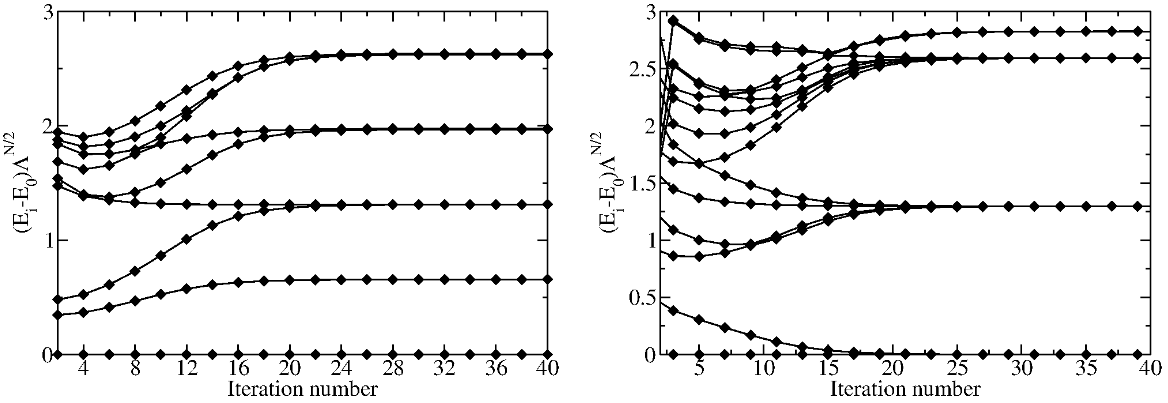

(a)

(b)

Figure 5.1: (a) Finite size NRG energy spectrum at zero temperature. Even energy flows for the following parameters; coupling constant $J = 0.2$, $\Lambda = 2$, (b) Odd energy flow for the same parameters.

5.4.2 Two-channel Kondo effect spectra

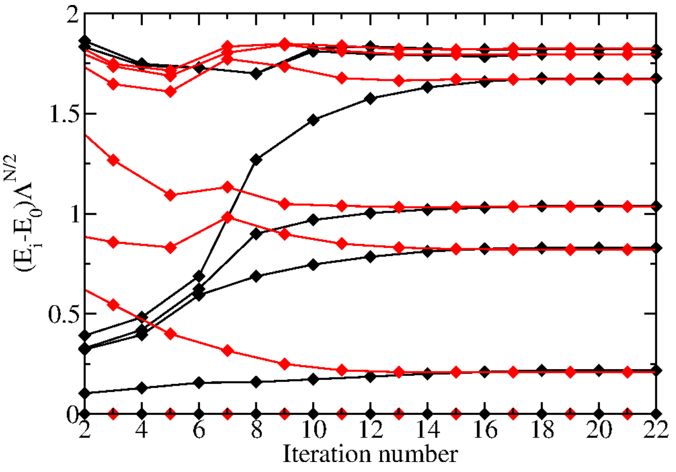

Figure 5.2: Finite NRG spectrum for lowest lying levels for the isotropic spin-1/2 2CK model. The coupling strength $J = 0.2$ and the discretization parameter $\Lambda = 3$.

The 2CK spectra is remarkably different from the 1CK spectra. It is more complicated and has a non-trivial fixed point. Unlike in the 1CK case, the even and odd iterations flow to the same value in the region of the fixed point. The energy level spacing is not uniform. This leads to the statement that the quantum numbers of the free states can not be that of a Fermi liquid. Fig. 5.2 shows the NRG finite spectrum at zero temperature for the spin-1/2 2CK model, where the red and black lines are the odd and even iterations, respectively. This 2CK NRG spectrum was first explained by Cragg et al. in [8]. It can be observed in Fig. 5.2 that there is an even-odd alternation for the first few iterations and the reason for this is the nearness to the non-interacting fixed point. The spectrum ultimately flows to the two-channel fixed point as the number of iterations increase. The impurity in the 2CK is dressed and has an infinite size, thereby making it impossible to define asymptotic scattering states with respect to it. Asymptotic scattering states are states that at the fixed point, are infinitely close to the Fermi level. Because of the absence of these states the calculation does not show any even-odd effect. We use the spectra presented here as a benchmark to compare the spectra of the model that we are investigating in this thesis. This comparison helps us to identify the fixed point in the model under investigation here.

Chapter 6

Application of the numerical renormalization group to the partially broken SU(3) Kondo model

In this chapter we use the numerical renormalization group (NRG) method exposed in chapter 5 to solve the partially broken SU(3) Kondo model explained in chapter 4. We modify the NRG scheme proposed by Wilson [1] to suit our purpose. We start by describing the approach to attain this goal and then present both the single- and two-channel Kondo results. We show that the partially broken SU(3) Kondo model has the usual characteristics of the Kondo effect. In this regard we look at the impurity contribution to the entropy of the system in both 1CK and 2CK scenarios. Another important thing here is to present the phase diagram of the model of both 1CK and 2CK cases which distinguishes between the potential scattering and the Kondo effect phases. Lastly, the duality behavior of 2CK is investigated and also the effects of small magnetic fields applied to the impurity.

6.1 Approach

A detailed explanation on how we use the NRG method to solve the partially broken SU(3) Kondo model is described in this section. We show how the starting Hamiltonian is constructed and how we move from the algebraic Hamiltonian to the matrix form that is required for the NRG computation. The basis states are also built up and the iterative structure of the Hamiltonian is shown. This detailed explanation is done only for 1CK and the general idea extrapolated to the 2CK case.

6.1.1 Single-channel Kondo

The single-channel case of the partially broken SU(3) Kondo model arises when the electrons of the conduction band are all of the same flavor or all polarized in the same direction. Using the Hamiltonian in (4.2) we construct the matrix form of the starting Hamiltonian. Let us start with a few definitions of the operators needed for this purpose. Let $d_m^\dagger$ (d_m) be the creation (annihilation) operator for the impurity in the different states

$m = -1, 0, +1$. The SU(3) operators of the impurity are defined as follows

$$\begin{aligned} S_z &= d_1^\dagger d_1 - d_{-1}^\dagger d_{-1} \\ S_{mn} &= d_m^\dagger d_n. \end{aligned} \tag{6.1}$$

The SU(3) operators acting on the conduction band Fock space are lower-case s_z and s_{mn}. They are obtained by substituting $c_m = \sum_k c_{\mathbf{k}\sigma m}$ in (6.1) where c_m is the fermionic operators acting on the conduction band electrons. The representation chosen here is the one in which the SU(3) shows an unbroken symmetry of the SU(2) subgroup in the states $m = -1, +1$. (4.2) can now be rewritten in the NRG discretized form using these different operators and the following form is obtained

$$\mathcal{H} = \sum_{i=1}^{3} \sum_{n} \xi_n (c_{n+1,i}^\dagger c_{n,i} + h.c) + \Delta_0 \sum_{m=\pm 1} d_m^\dagger d_m + H_{int} \tag{6.2}$$

where H_{int} is the interaction term which has the numeric form

$$\begin{aligned} H_{int} \;=\; & 2g_{00}^{0} d_0^\dagger d_0 c_0^\dagger c_0 + 2g_{00}^{1} d_0^\dagger d_0 c_1^\dagger c_1 + 2g_{00}^{-1} d_0^\dagger d_0 c_{-1}^\dagger c_{-1} + 2g_{00}^{0} d_1^\dagger d_1 c_0^\dagger c_0 \\ & + 2g_{00}^{0} d_{-1}^\dagger d_{-1} c_0^\dagger c_0 + g_{10}^{0} d_1^\dagger d_0 c_{-1}^\dagger c_0 + g_{-10}^{0} d_{-1}^\dagger d_0 c_1^\dagger c_0 + g_{10}^{1} d_1^\dagger d_0 c_0^\dagger c_1 \\ & + g_{-10}^{-1} d_{-1}^\dagger d_0 c_0^\dagger c_{-1} + g_{01}^{-1} d_0^\dagger d_1 c_0^\dagger c_{-1} + g_{0-1}^{1} d_0^\dagger d_{-1} c_0^\dagger c_1 + g_{01}^{0} d_0^\dagger d_1 c_1^\dagger c_0 \\ & + g_{0-1}^{0} d_0^\dagger d_{-1} c_{-1}^\dagger c_0 + J_\perp (d_1^\dagger d_{-1} c_{-1}^\dagger c_1 + d_{-1}^\dagger d_1 c_1^\dagger c_{-1}) \\ & + \frac{1}{2} J_z (d_1^\dagger d_1 c_1^\dagger c_1 + d_{-1}^\dagger d_{-1} c_{-1}^\dagger c_{-1}) - \frac{1}{2} J_z (d_1^\dagger d_1 c_{-1}^\dagger c_{-1} + d_{-1}^\dagger d_{-1} c_1^\dagger c_1) \end{aligned} \tag{6.3}$$

The starting Hamiltonian is the impurity levels and the interaction term only, since the on-site energy $\varepsilon_n = 0$ for reasons already mentioned in chapter 5, hence the Hamiltonian term from the conduction site is not included and this Hamiltonian is denoted here as

$$H_0 = \Delta_0 \sum_{m=\pm 1} d_m^\dagger d_m + H_{int} \tag{6.4}$$

Since our system respects the constraint that the impurity is singly occupied, the matrices defining the impurity have this constraint built into them. These matrices $d_m^\dagger d_m$ are given in the original undiagonalized basis of the Hilbert space as follows

$$d_{-1}^\dagger d_{-1} = \left(\begin{array}{c|c|c} \mathbb{1} & 0 & 0 \\ \hline 0 & 0 & 0 \\ \hline 0 & 0 & 0 \end{array}\right), \quad d_0^\dagger d_0 = \left(\begin{array}{c|c|c} 0 & 0 & 0 \\ \hline 0 & \mathbb{1} & 0 \\ \hline 0 & 0 & 0 \end{array}\right), \quad d_1^\dagger d_1 = \left(\begin{array}{c|c|c} 0 & 0 & 0 \\ \hline 0 & 0 & 0 \\ \hline 0 & 0 & \mathbb{1} \end{array}\right) \tag{6.5}$$

$$d_{-1}^\dagger d_0 = \left(\begin{array}{c|c|c} 0 & \mathbb{1} & 0 \\ \hline 0 & 0 & 0 \\ \hline 0 & 0 & 0 \end{array}\right), \quad d_{-1}^\dagger d_1 = \left(\begin{array}{c|c|c} 0 & 0 & \mathbb{1} \\ \hline 0 & 0 & 0 \\ \hline 0 & 0 & 0 \end{array}\right), \quad d_0^\dagger d_1 = \left(\begin{array}{c|c|c} 0 & 0 & 0 \\ \hline 0 & 0 & \mathbb{1} \\ \hline 0 & 0 & 0 \end{array}\right) \tag{6.6}$$

where $\mathbb{1}$ is an 8×8 unit matrix. Thus the starting Hamiltonian for the NRG procedure is a 24×24 matrix. It consists of the impurity and the first site of the Wilson chain.

Number	States
1	$\vert 0\rangle$
2	$c^\dagger_{-1}\vert 0\rangle$
3	$c^\dagger_{0}\vert 0\rangle$
4	$c^\dagger_{1}\vert 0\rangle$
5	$c^\dagger_{-1}c^\dagger_{0}\vert 0\rangle$
6	$c^\dagger_{1}c^\dagger_{0}\vert 0\rangle$
7	$c^\dagger_{-1}c^\dagger_{1}\vert 0\rangle$
8	$c^\dagger_{-1}c^\dagger_{1}c^\dagger_{0}\vert 0\rangle$

Table 6.1: The eight possible basis states on the first site of the Wilson chain in the 1CK case.

The 24 basis states of this Hamiltonian are the product states of the three impurity states $m = 0, -1, +1$ and the eight possible states at the first site of the Wilson chain which are given in Table 6.1. The above Hamiltonian, H_0 is then diagonalized numerically using Lapack routines, and the output are the eigenvalues and the eigenvectors. The eigenenergies are sorted with respect to increasing energies and only the low lying levels are kept since we are only interested in the low temperature physics. The Hilbert space grows by a factor of 8 with the addition of a new site. This means that after adding a few sites the Hilbert space becomes so large that it can no longer be kept in the computer. The way around this is to truncate it and keep only the low lying states which justifies the sorting of the eigenenergies. One then uses the eigenvectors from H_0 to rotate all the operators one is interested in to the new basis and then sort them with respect to the eigenvalues of H_0. With this, one is ready to build up H_1 which is the Hamiltonian obtained by adding a new site to the Hamiltonian H_0. The matrix form is as follows

$$H_1 = \begin{array}{c} \\ |0\rangle_1 \\ c^\dagger_{-1}|0\rangle_1 \\ c^\dagger_{0}|0\rangle_1 \\ c^\dagger_{1}|0\rangle_1 \\ c^\dagger_{0}c^\dagger_{-1}|0\rangle_1 \\ c^\dagger_{1}c^\dagger_{-1}|0\rangle_1 \\ c^\dagger_{1}c^\dagger_{0}|0\rangle_1 \\ c^\dagger_{1}c^\dagger_{0}c^\dagger_{-1}|0\rangle_1 \end{array} \begin{array}{c} \begin{array}{cccccccc} |0\rangle_1 & c^\dagger_{-1}|0\rangle_1 & c^\dagger_{0}|0\rangle_1 & c^\dagger_{1}|0\rangle_1 & c^\dagger_{0}c^\dagger_{-1}|0\rangle_1 & c^\dagger_{1}c^\dagger_{-1}|0\rangle_1 & c^\dagger_{1}c^\dagger_{0}|0\rangle_1 & c^\dagger_{1}c^\dagger_{0}c^\dagger_{-1}|0\rangle_1 \end{array} \\ \begin{pmatrix} \Lambda^{\frac{1}{2}}H_0 & -\xi_0\tilde{c}^\dagger_{0-1} & -\xi_0\tilde{c}^\dagger_{00} & -\xi_0\tilde{c}^\dagger_{01} & \mathbf{0} & \mathbf{0} & \mathbf{0} & \mathbf{0} \\ -\xi_0\tilde{c}_{0-1} & \Lambda^{\frac{1}{2}}H_0 & \mathbf{0} & \mathbf{0} & \xi_0\tilde{c}^\dagger_{00} & \xi_0\tilde{c}^\dagger_{01} & \mathbf{0} & \mathbf{0} \\ -\xi_0\tilde{c}_{00} & \mathbf{0} & \Lambda^{\frac{1}{2}}H_0 & \mathbf{0} & -\xi_0\tilde{c}^\dagger_{0-1} & \mathbf{0} & \xi_0\tilde{c}^\dagger_{01} & \mathbf{0} \\ -\xi_0\tilde{c}_{01} & \mathbf{0} & \mathbf{0} & \Lambda^{\frac{1}{2}}H_0 & \mathbf{0} & -\xi_0\tilde{c}^\dagger_{0-1} & -\xi_0\tilde{c}^\dagger_{00} & \mathbf{0} \\ \mathbf{0} & \xi_0\tilde{c}_{00} & \xi_0\tilde{c}_{0-1} & \mathbf{0} & \Lambda^{\frac{1}{2}}H_0 & \mathbf{0} & \mathbf{0} & -\xi_0\tilde{c}^\dagger_{01} \\ \mathbf{0} & \xi_0\tilde{c}_{01} & \mathbf{0} & -\xi_0\tilde{c}_{00} & \mathbf{0} & \Lambda^{\frac{1}{2}}H_0 & \mathbf{0} & \xi_0\tilde{c}^\dagger_{00} \\ \mathbf{0} & \mathbf{0} & \xi_0\tilde{c}_{01} & -\xi_0\tilde{c}_{00} & \mathbf{0} & \mathbf{0} & \Lambda^{\frac{1}{2}}H_0 & -\xi_0\tilde{c}^\dagger_{0-1} \\ \mathbf{0} & \mathbf{0} & \mathbf{0} & \mathbf{0} & -\xi_0\tilde{c}^\dagger_{01} & \xi_0\tilde{c}^\dagger_{00} & -\xi_0\tilde{c}^\dagger_{0-1} & \Lambda^{\frac{1}{2}}H_0 \end{pmatrix} \end{array} \tag{6.7}$$

$\xi_0\tilde{c}_{0m}$, $\xi_0\tilde{c}^\dagger_{0m}$, $\Lambda^{\frac{1}{2}}H_0$, and $\mathbf{0}$ are all 24×24 matrices, where $\xi_0\tilde{c}_{0m}$ are the transformed fermionic operators of the new site that were acting in the previous site. $\Lambda^{\frac{1}{2}}H_0$ are diagonal matrices and $\mathbf{0}$ are simply zero matrices. This means that the dimension of the Hamiltonian H_1 is 192×192. Following the same procedure as above the eigenenergies and eigenvectors of H_1 are obtained by diagonalizing it. For H_2 to be constructed, $c^\dagger_{1m}$ needs to be determined first because it is necessary for the continuation of the iteration. Generally these operators are given in the original basis of the Hilbert space and are usually as follows

$$c^\dagger_{-1} = \begin{array}{c} \\ |0\rangle \\ c^\dagger_{-1}|0\rangle \\ c^\dagger_0|0\rangle \\ c^\dagger_1|0\rangle \\ c^\dagger_0c^\dagger_{-1}|0\rangle \\ c^\dagger_1c^\dagger_{-1}|0\rangle \\ c^\dagger_1c^\dagger_0|0\rangle \\ c^\dagger_1c^\dagger_0c^\dagger_{-1}|0\rangle \end{array} \begin{array}{c} \begin{array}{cccccccc} |0\rangle & c^\dagger_{-1}|0\rangle & c^\dagger_0|0\rangle & c^\dagger_1|0\rangle & c^\dagger_0c^\dagger_{-1}|0\rangle & c^\dagger_1c^\dagger_{-1}|0\rangle & c^\dagger_1c^\dagger_0|0\rangle & c^\dagger_1c^\dagger_0c^\dagger_{-1}|0\rangle \end{array} \\ \begin{pmatrix} 0 & 0 & 0 & 0 & 0 & 0 & 0 & 0 \\ \mathbb{1} & 0 & 0 & 0 & 0 & 0 & 0 & 0 \\ 0 & 0 & 0 & 0 & 0 & 0 & 0 & 0 \\ 0 & 0 & 0 & 0 & 0 & 0 & 0 & 0 \\ 0 & 0 & -\mathbb{1} & 0 & 0 & 0 & 0 & 0 \\ 0 & 0 & 0 & -\mathbb{1} & 0 & 0 & 0 & 0 \\ 0 & 0 & 0 & 0 & 0 & 0 & 0 & 0 \\ 0 & 0 & 0 & 0 & 0 & 0 & \mathbb{1} & 0 \end{pmatrix} \end{array} \tag{6.8}$$

$$c^\dagger_{0} = \begin{array}{c} \\ |0\rangle \\ c^\dagger_{-1}|0\rangle \\ c^\dagger_0|0\rangle \\ c^\dagger_1|0\rangle \\ c^\dagger_0c^\dagger_{-1}|0\rangle \\ c^\dagger_1c^\dagger_{-1}|0\rangle \\ c^\dagger_1c^\dagger_0|0\rangle \\ c^\dagger_1c^\dagger_0c^\dagger_{-1}|0\rangle \end{array} \begin{array}{c} \begin{array}{cccccccc} |0\rangle & c^\dagger_{-1}|0\rangle & c^\dagger_0|0\rangle & c^\dagger_1|0\rangle & c^\dagger_0c^\dagger_{-1}|0\rangle & c^\dagger_1c^\dagger_{-1}|0\rangle & c^\dagger_1c^\dagger_0|0\rangle & c^\dagger_1c^\dagger_0c^\dagger_{-1}|0\rangle \end{array} \\ \begin{pmatrix} 0 & 0 & 0 & 0 & 0 & 0 & 0 & 0 \\ 0 & 0 & 0 & 0 & 0 & 0 & 0 & 0 \\ \mathbb{1} & 0 & 0 & 0 & 0 & 0 & 0 & 0 \\ 0 & 0 & 0 & 0 & 0 & 0 & 0 & 0 \\ 0 & \mathbb{1} & 0 & 0 & 0 & 0 & 0 & 0 \\ 0 & 0 & 0 & 0 & 0 & 0 & 0 & 0 \\ 0 & 0 & 0 & -\mathbb{1} & 0 & 0 & 0 & 0 \\ 0 & 0 & 0 & 0 & 0 & -\mathbb{1} & 0 & 0 \end{pmatrix} \end{array} \tag{6.9}$$

$$c^\dagger_{1} = \begin{array}{c} \\ |0\rangle \\ c^\dagger_{-1}|0\rangle \\ c^\dagger_0|0\rangle \\ c^\dagger_1|0\rangle \\ c^\dagger_0c^\dagger_{-1}|0\rangle \\ c^\dagger_1c^\dagger_{-1}|0\rangle \\ c^\dagger_1c^\dagger_0|0\rangle \\ c^\dagger_1c^\dagger_0c^\dagger_{-1}|0\rangle \end{array} \begin{array}{c} \begin{array}{cccccccc} |0\rangle & c^\dagger_{-1}|0\rangle & c^\dagger_0|0\rangle & c^\dagger_1|0\rangle & c^\dagger_0c^\dagger_{-1}|0\rangle & c^\dagger_1c^\dagger_{-1}|0\rangle & c^\dagger_1c^\dagger_0|0\rangle & c^\dagger_1c^\dagger_0c^\dagger_{-1}|0\rangle \end{array} \\ \begin{pmatrix} 0 & 0 & 0 & 0 & 0 & 0 & 0 & 0 \\ 0 & 0 & 0 & 0 & 0 & 0 & 0 & 0 \\ 0 & 0 & 0 & 0 & 0 & 0 & 0 & 0 \\ \mathbb{1} & 0 & 0 & 0 & 0 & 0 & 0 & 0 \\ 0 & 0 & 0 & 0 & 0 & 0 & 0 & 0 \\ 0 & \mathbb{1} & 0 & 0 & 0 & 0 & 0 & 0 \\ 0 & 0 & \mathbb{1} & 0 & 0 & 0 & 0 & 0 \\ 0 & 0 & 0 & 0 & \mathbb{1} & 0 & 0 & 0 \end{pmatrix} \end{array} \tag{6.10}$$

The symbol $\mathbb{1}$ is a 24×24 identity matrix and the 0 are 24×24 zero matrices too. These three fermionic operators are rotated to the new site using the eigenvectors from the diagonalized Hamiltonian. During each iteration, the Hamiltonian is diagonalized, the eigenenergies sorted in increasing order, the system truncated, a new site added to the Wilson chain, and finally, the fermionic operators acting on this site are set up. To check for convergence in the NRG, the low lying eigenenergies of the system are plotted against the iteration number. The convergence of these eigenenergies indicates that the strong coupling fixed point has been reached. For details on how this is actually calculated, see appendix B.

6.1.2 Two-channel Kondo

As already mentioned in chapter 4, the two-channel scenario arises from the model under investigation in this thesis by virtue of the degeneracy of the conduction band electrons since the impurity is non-magnetic. To build up the NRG scheme for this case is quite demanding since the impurity space is comprised of three fermionic operators corresponding to the three impurity levels. Correspondingly, the conduction electrons carry a three-fold

SU(3) degree of freedom, represented by the orbital degrees of freedom, $m = -1, 0, +1$, and in addition a two-fold degree of freedom of the magnetic spin, $\sigma = \downarrow, \uparrow$. Thus there are six conduction electron operators per lattice site. As a consequence, three Wilson chains, one for each of the orbital degrees of freedom are needed for the NRG. Moreover, each of these Wilson chains come in two flavors, the magnetic electron spin, which is conserved in the interactions of the Hamiltonian. Collecting all the degrees of freedom mentioned above implies that in each iteration of the NRG the Hilbert space grows by a factor of 64. The 64 different states are obtained from different fermionic operators acting on the vacuum state as shown in Table 6.2. This makes the NRG algorithm for this extraordinarily demanding, both in terms of memory and computing time. For the technical details on the build up of the NRG scheme for the two 2CK case, see appendix B.

States	Number of states
$\|0\rangle$	1
$c^\dagger_{m\sigma}\|0\rangle$	6
$c^\dagger_{m\sigma}c^\dagger_{m\sigma}\|0\rangle$	15
$c^\dagger_{m\sigma}c^\dagger_{m\sigma}c^\dagger_{m\sigma}\|0\rangle$	20
$c^\dagger_{m\sigma}c^\dagger_{m\sigma}c^\dagger_{m\sigma}c^\dagger_{m\sigma}\|0\rangle$	15
$c^\dagger_{m\sigma}c^\dagger_{m\sigma}c^\dagger_{m\sigma}c^\dagger_{m\sigma}c^\dagger_{m\sigma}\|0\rangle$	6
$c^\dagger_{m\sigma}c^\dagger_{m\sigma}c^\dagger_{m\sigma}c^\dagger_{m\sigma}c^\dagger_{m\sigma}c^\dagger_{m\sigma}\|0\rangle$	1

Table 6.2: The number of basis states obtained by acting the different fermionic operators on the vacuum state.

6.2 Results of the single-channel case

The first results obtained from an NRG run are the eigenenergies of the system, which when plotted against the iteration number, gives us information on the different fixed points of the system. In the case of the single-channel model there is this alternation between the odd-even iteration as already explained in chapter 5.

6.2.1 Flow diagrams

The flow diagrams permit us to make a statement on whether the system has reached the 1CK fixed point or not. Fig. 6.1 shows a typical flow of the even iterations of eigenenergies in which the lowest lying energy levels varies with the length of the chain. The energies are scaled by a factor of $D\Lambda^{N/2}$, where D is the bandwidth and Λ the discretization parameter as already discussed in chapter 5. These eigenenergies show the basic physics of the Kondo problem. One can notice that after a few iterations the system crosses over to another regime. The system starts up at the weak coupling regime and then between iteration number 10 and 20 the system crosses over to the strong coupling regime where it then flows to the stable fixed point at iteration number greater than 20. The energy levels are equally spaced which indicates that we are dealing with a Fermi liquid. The odd iterations have the same structure, but for the fact that they are phase shifted by $\pi/2$. At the fixed point the impurity degrees of freedom are completely screened. A knowledge of these eigenenergies provides the necessary ingredient for the calculation of the different physical properties of the system and enables us to map out a phase diagram of the Kondo fixed point and the potential scattering regime as will be illustrated in the next subsection. The fixed point value of the eigenenergies is changed in the presence of a potential scattering term in the Hamiltonian as lucidly explained by Kondo using perturbative techniques in [58] and by Cragg and Lloyd in [59] using the NRG. Kondo explains that there even exist a critical value for the potential scattering which when exceeded, a reverse Kondo effect is observed instead of the usual one. In this regime the resistivity decreases with the decreasing temperature as a consequence of the strong potential scattering.

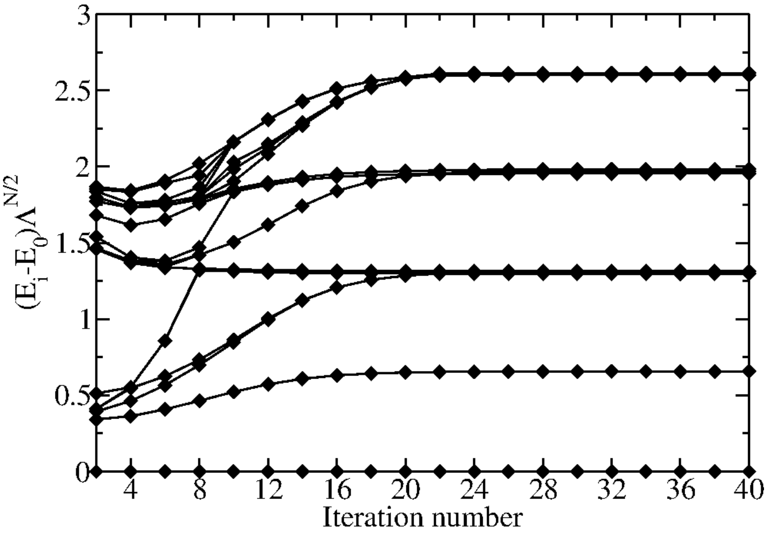

Figure 6.1: NRG energy flows for the 1CK partially broken SU(3) model lowest lying many particle levels for the following parameters: $J = 0.2$, $g = 0.002$, $\Delta_0 = 0.001$ and $\Lambda = 2$.

6.2.2 Phase diagrams

The flow to the 1CK or the potential scattering fixed points for different set of parameters can be summarized in the phase diagram. In the 1CK scenario, one can easily identify this by just looking at even-odd alternations of the energies. One compares the energies in this case with energies at zero couplings. In the case of zero couplings the energies are just those of the interacting system, and looking at the Wilson chain one knows how many electrons were added to the chain. This is simply just taken to be the iteration number of the NRG calculation. Since the energies of a chain depend on whether the number of electrons are even or odd then in the case where the system flows to strong coupling, it contains one electron less than in the non interacting case of zero coupling. This is because the first electron forms a singlet with the impurity and hence decouples from the other conduction electrons. This means that the odd iteration number energies in the case of the non-interacting case become the even iteration number energies in the case of the strong coupling and vice versa. We use this simple criterion to produce the phase diagram in Fig. 6.2. Whenever some set of parameters is chosen in each phase, the system will flow to the corresponding phase. This reinforces the earlier prediction by Arnold et al. in [2] for the 2CK calculations that the flow of the system to the 2CK fixed point is mainly driven by the coupling constant J. We have given just one phase line here that corresponds to the ratio $g/J = 0.01$. The influence of the ground-to-excited states scattering constant g on the flow of the system from the non-interacting fixed point to the Kondo fixed point will be explored in the 2CK scenario. The is because it is the model we are more interested in and also because we can easily compare our results to those in [2]. In Fig. 6.2, one sees an offset in the ordinate when it is compared to the 2CK phase diagram in [2]. This offset has nothing to do with the physics but rather it is just due to the numerics, since the NRG method always needs some finite couplings that can enable the system to flow to the Kondo fixed point in a finite number of iterations. If we could iterate the system for an infinite number of iterations then the offset will go away and our results will agree exactly with the analytic ones of the perturbative renormalization group (PRB) method in [2]. This phase diagram shows that the 1CK effect occurs in a wide parameter range in this partially broken SU(3) Kondo model.

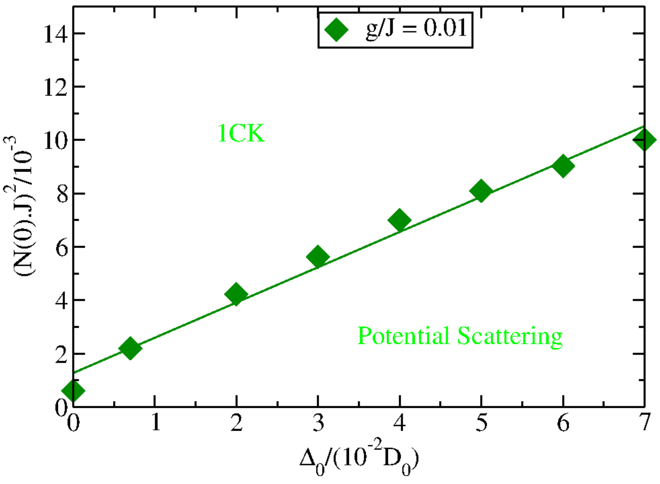

Figure 6.2: Phase diagram separating single-channel Kondo and potential scattering regimes in the phase space of the level spacing Δ_0 and the dimensionless coupling strength $(N(0)J)^2$. To the right of the line, the system shows only potential scattering while to the left the system shows 1CK effect.

6.2.3 Entropy

The entropy of the impurity is obtained from the NRG using the following expression

$$S_{imp}(T) = S_{imp,cb}(T) - S_{cb}(T) \tag{6.11}$$

where $S_{imp}(T)$ is the impurity entropy at a certain temperature T, $S_{imp,cb}(T)$ the combined entropy of the impurity and the conduction band, and $S_{cb}(T)$ is the entropy of the conduction band. Two NRG runs are required to obtain the impurity entropy. The first run is the combined case where the coupling constant is non-zero and the second case is when the coupling constants are set to zero so one gets only the contribution of the conduction band. This conduction band contribution is then subtracted from the combined case as done in (6.11). Fig. 6.3(a) shows the entropy of the impurity on the ordinate and the ratio of the temperature to the Kondo temperature on the abscissa which tells us that the entropy tends to zero below T_K. The actual expression for the different terms in (6.11) are given in (5.7). A careful look at (5.7) shows that one has to calculate averages

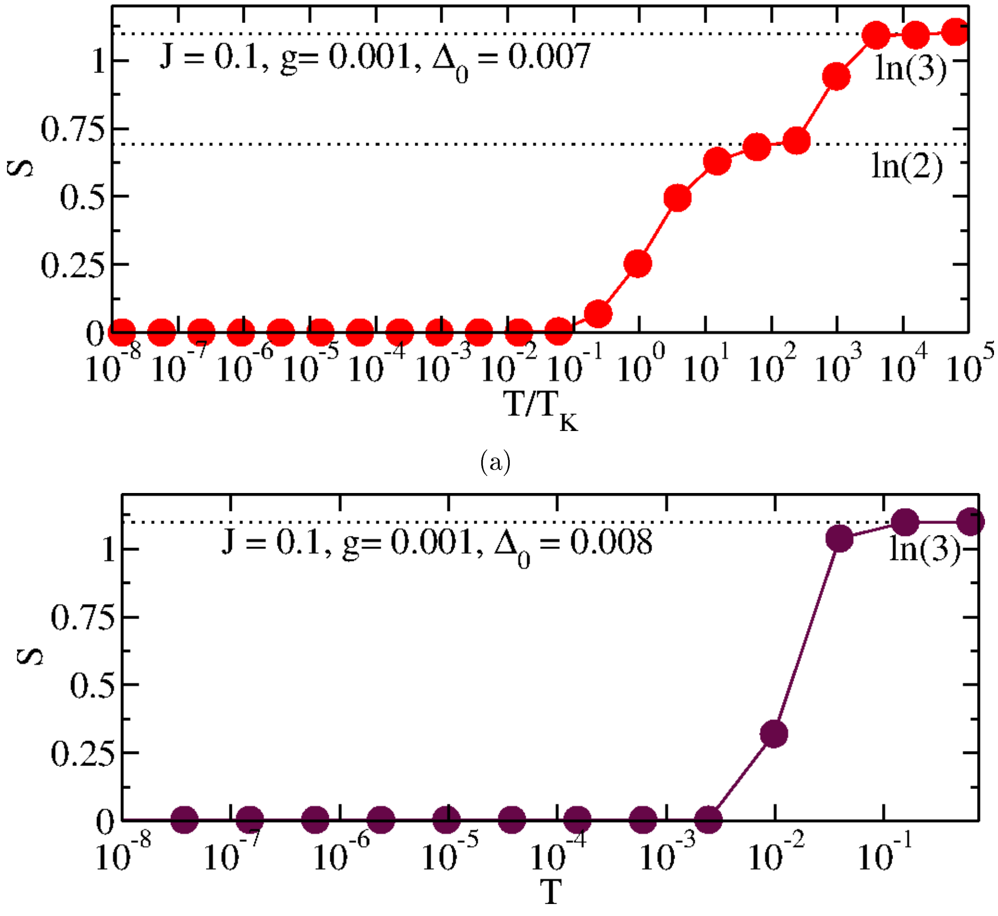

(a)

(b)

Figure 6.3: The variation of the impurity entropy without magnetic field in the 1CK scenario as the temperature decreases for the following general parameters: $J = 0.1$ and $\Lambda = 4$, (a) Impurity entropy when there is a flow to the 1CK regime for $g/J = 0.01$ and $\Delta_0 = 0.007$, (b) The entropy of the impurity in the potential scattering phase for $g/J = 0.01$ and $\Delta_0 = 0.008$. For details of the explanation of these figures, see text.

using the Boltzmann weights. The inverse temperature value is crucial for this calculation since its value for this calculations depends on both the discretization parameter Λ and the number of states kept in each NRG iteration. One has to make sure that the inverse temperature β in use is the right one and works well for the Λ value and the number of states kept so that one gets the right entropy behavior for the impurity. It is a demanding computation in terms of computing time in the case of 2CK. Details of this calculations are given in appendix C.

The entropy of the impurity for zero Kondo coupling is simply the logarithm of the ground state degeneracy of the free impurity; which means that in our case where the impurity has three levels in an isolated state, its entropy is $S(T) = \ln 3$ for $T \gg \Delta_0$ and $S(0) = \ln 1$ for $T \ll \Delta_0$, since the excited states are frozen out at low temperatures. The entropy is given in units where $k_B = 1$. The ground state degeneracy is reduced under renormalization from the non-interacting fixed point to the infrared stable fixed point. The reason for this behavior has been intuitively explained by Affleck in [60] to be related to the fact that when lower energy scales are investigated, approximately degenerate levels of impurities display small splittings, thereby reducing the degeneracy. The entropy of the impurity gives us the strongest evidence yet of the crossover of the degenerate doublet to become the ground states, while the singlet state is decoupled. This can be seen in Fig. 6.3(a) which shows that at high temperature ($T \gg \Delta_0$), all three levels contribute to the entropy of the impurity, hence ln3. As the temperature is decreased, the degenerate doublet is renormalized downward and becomes the ground states, consequently the entropy changes to ln2 and, hence the plateau. It can be seen in Fig. 6.3(a) that the crossover energy scale from ln3 to ln2 plateau is of the order of Δ_0. Kondo physics then sets in and the doublet is screened and the entropy of the impurity becomes ln1 due to the complete screening in the 1CK effect scenario. It can also be observed that the crossover energy scale from ln2 to ln1 is equal to the Kondo temperature.

On the other hand, when the level spacing is increased leaving the coupling strength constant, then the coupling strength is no longer strong enough to drive down the excitation of the degenerate doublet to at least zero. Therefore the 1CK effect is never manifested. This is because the ground state remains non-degenerate and only potential scattering occurs, and so the system just flows from ln3 to ln1, as shown in Fig. 6.3(b).

6.3 Results of the two-channel case

6.3.1 Flow diagrams

The flow to the 2CK fixed point in the NRG method, as already briefly explained in chapter 5, can be visualized by looking at the flow of the eigenvalues with respect to the number of iterations [1]. Unlike in the 1CK case, where there is an odd-even alternation in the energy levels and a uniform spacing of the energy levels, the energy levels in the 2CK flow to the same point and are non-uniformly spaced [9]. In Fig. 6.4(a) a selected number of energy levels have been plotted to elucidate the preceding sentence. We consider different parameter sets given by the coupling constants of the interacting Hamiltonian and the initial level spacing Δ_0 to show how the 2CK fixed point is reached. The three major parameters of the model are the coupling strength J, ground-to-excited state transitions g, and the level spacing Δ_0. We show that, when the level spacing is large, then the 2CK is never reached because the excited doublet never renormalizes downward enough

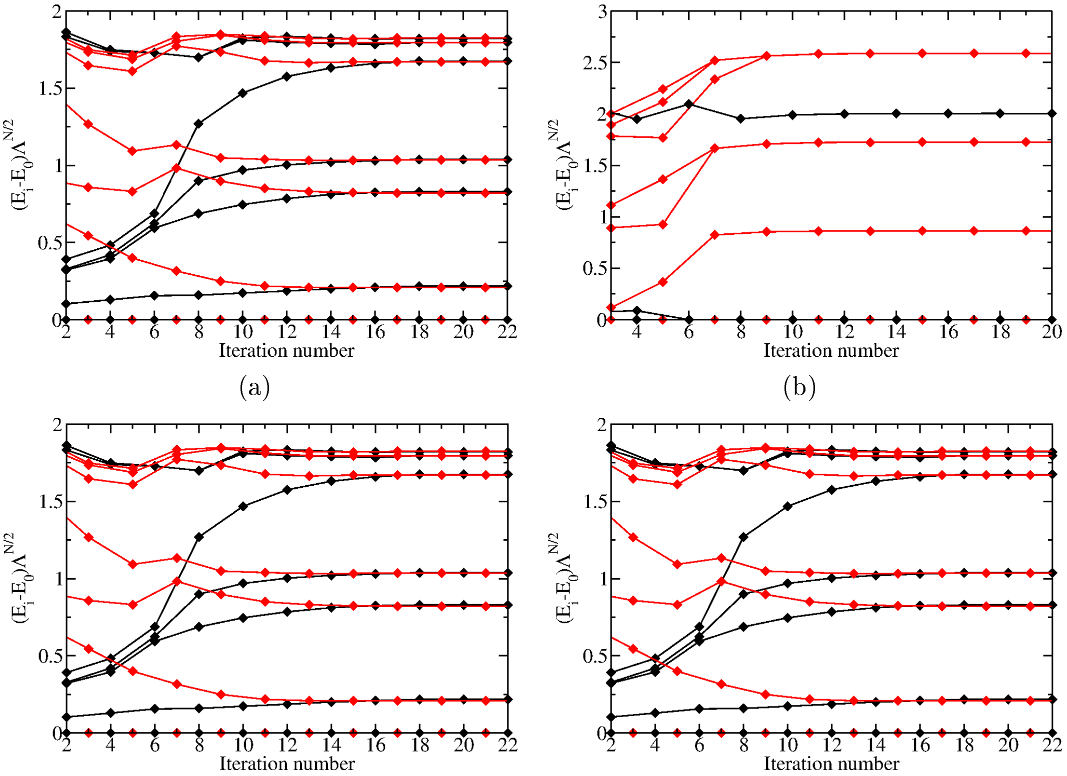

(a) (b) (c) (d)

Figure 6.4: NRG energy levels for the following general parameters: $J = 0.2$, $g = 0.002$, and $\Lambda = 4$ (a) when $\Delta_0 = 0.13$, it shows a 2CK fixed point because both the odd-even iterations flow to the same fixed point and the energy levels have a non-uniform spacing. The odd iterations are the red lines whereas the black lines are for the even iterations and (b) When $\Delta_0 = 0.14$, the coupling is no longer strong enough to renormalize Δ_0 down to at least zero or negative for the flow to the 2CK fixed point to be attained. Consequently the odd and even iterations flow to different fixed points and the energy levels are equally spaced. (c) When $\Delta_0 = -0.14$, the system flows to the 2CK fixed point directly since there is no need for the downward renormalization as the degenerate doublet is already the ground states. (d) For $\Delta_0 = -1.0$ the same flow is obtained as in $\Delta_0 = 0.13$ and $\Delta_0 = -0.14$ for the same reason as in (c).

to become the ground state. When the level splitting in Fig. 6.4(a) is increased by 0.01, leaving the coupling J constant, one can immediately see that the system does not flow to the 2CK fixed point since the even and the odd iterations flow to different points (see Fig. 6.4(b)). The reason for this behavior is because the interactions become insufficient to renormalize down the degenerate doublet to become the ground states. If J is increased, then the system can again flow to the 2CK fixed point.

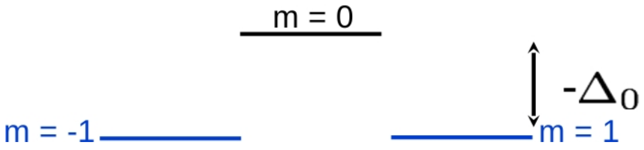

Figure 6.5: Level scheme of the impurity for $\Delta_0 < 0$

When the level spacing is negative, the degenerate doublet is already the ground states and the singlet the excited state. In this case the Kondo effects occurs without need for the downward renormalization of Δ_0 since the system ground states is degenerate from the onset of the RG procedure. The level scheme of the impurity when the level spacing $\Delta_0 < 0$ is shown in Fig. 6.5. Fig. 6.4(c) and Fig. 6.4(d) show that the Kondo effect is insensitive to Δ_0 as long as $\Delta_0 < 0$. This behavior of the system confirms the conjecture in [2] that Δ_0 is renormalized downward when it is positive and that this downward renormalization is mainly driven by the coupling strength J.

6.3.2 Phase diagrams

The above behavior in Fig. 6.4(a) and Fig. 6.4(b) is summarized in a phase diagram, see Fig. 6.6, where we have plotted the dimensionless $(N(0)J)^2$ versus the level splitting Δ_0. The different points on the phase diagram are instable fixed points which separate the 2CK regime from that of the potential scattering. The larger the energy splitting is, the more strong interactions are required to renormalize down the doublet states in order for the system to flow to the 2CK fixed point. The offset seen in the 1CK case also appears in the 2CK case. The reason for this offset has been explained in the 1CK phase diagram and also applies here in the 2CK phase diagram. This phase diagram effectively confirms that the partially broken SU(3) Kondo model has a 2CK fixed point in a wide parameter range namely in the upper part of the phase diagram.

Effect of different parameters on the crossover

We look at the role played by the different parameters in the Hamiltonian in order for the 2CK effect to be realized. There are in general three different couplings involved in the Hamiltonian of the partially broken SU(3) Kondo Hamiltonian namely g_{mn} whose role varies depending on whether $m = n$ or $m \neq n$. When $m = n$ then the coupling g_{mn} is just a potential scatterer and its effect on the renormalization of level spacing is weak. When $m \neq n$, g_{mn} becomes responsible for the ground-to-excited states scattering in the system and therefore its effect on the crossover is stronger than that of the potential scattering terms. The bigger the value of this coupling the larger the potential scattering phase as shown in Fig. 6.6.

The next set of couplings that plays a crucial role for the 2CK effect to be observed

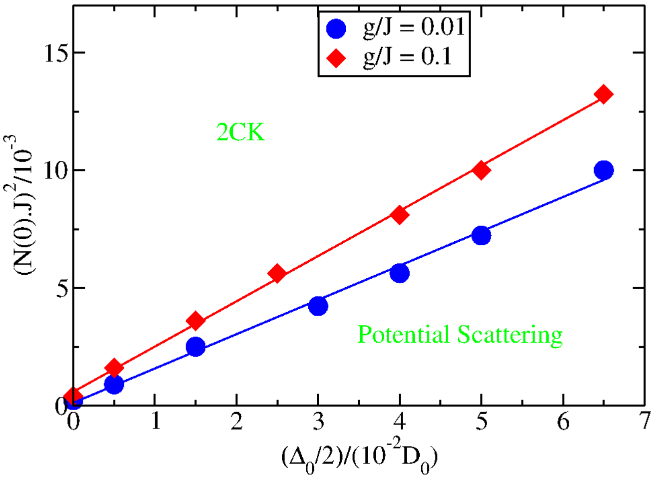

Figure 6.6: Phase diagram separating 2CK and potential scattering regimes in the phase space of the level spacing Δ_0 and the dimensionless coupling strength $(N(0)J)^2$. To the right of each of the lines the system shows only potential scattering while to the left the system shows 2CK effect.

are $J_\perp$ and J_z. $J_\perp$ and J_z are the couplings mainly in charge of the renormalization of the level spacing. The isotropic case occurs when $J_\perp = J_z/2$ and the anisotropic case when $J_\perp \neq J_z/2$. The 2CK fixed point does not “know” whether the system is isotropic or anisotropic. This has been shown by Pang and Cox in [9] and in our NRG calculations for this model we find the same behavior. The phase diagram presented in Fig. 6.6 is realized for the isotropic case.

The last but not least of the parameters is the level spacing Δ_0 which is the energy of the degenerate doublet $M = \pm 1$. If $\Delta_0 > 0$ then the degenerate pseudospin states $M = \pm 1$ are not the ground state therefore making it impossible for the Kondo effect to occur due to the fact that it can not be energetically occupied as the temperature tends to zero. Hence no resonance scattering can occur which is necessary for the Kondo effect. Contrary to the picture painted in the preceding sentence, 2CK effect is still observed even when $\Delta_0 > 0$. This is possible, if the level spacing Δ_0 is renormalized to at least zero or a negative value during the RG flow. The degenerate doublet becomes the ground states of the system. The downward renormalization of Δ_0 is mostly driven by the coupling constants $J_\perp$ and J_z. It turns out that Δ_0 covers a wide range depending on the choice of the initial coupling constants. If $\Delta_0 = 0$ then we have the full SU(3) Kondo model. The case of $\Delta_0 < 0$ is similar to the spin-1/2 2CK model since no downward renormalization is required for Δ_0 because the degenerate doublet ground states are already the ground states. In this situation the value of Δ_0 no longer influences the phase diagram and therefore almost the entire plane of negative Δ_0 and positive J^2 is in the 2CK regime.

6.3.3 Duality and non-monotonicity of the Kondo temperature

It has been shown in [32] that the Kondo temperature T_K dependence on bare coupling constant J peaks at $J = 0.6D$ and that T_K decays exponentially on both sides. The maximum is of the order of the band cutoff $T_K \approx D$. The T_K value never reaches the value of the band cutoff due to the presence of potential scattering which has the effect of reducing T_K. Non-Fermi liquid behavior is observed for all energies below T_K. The

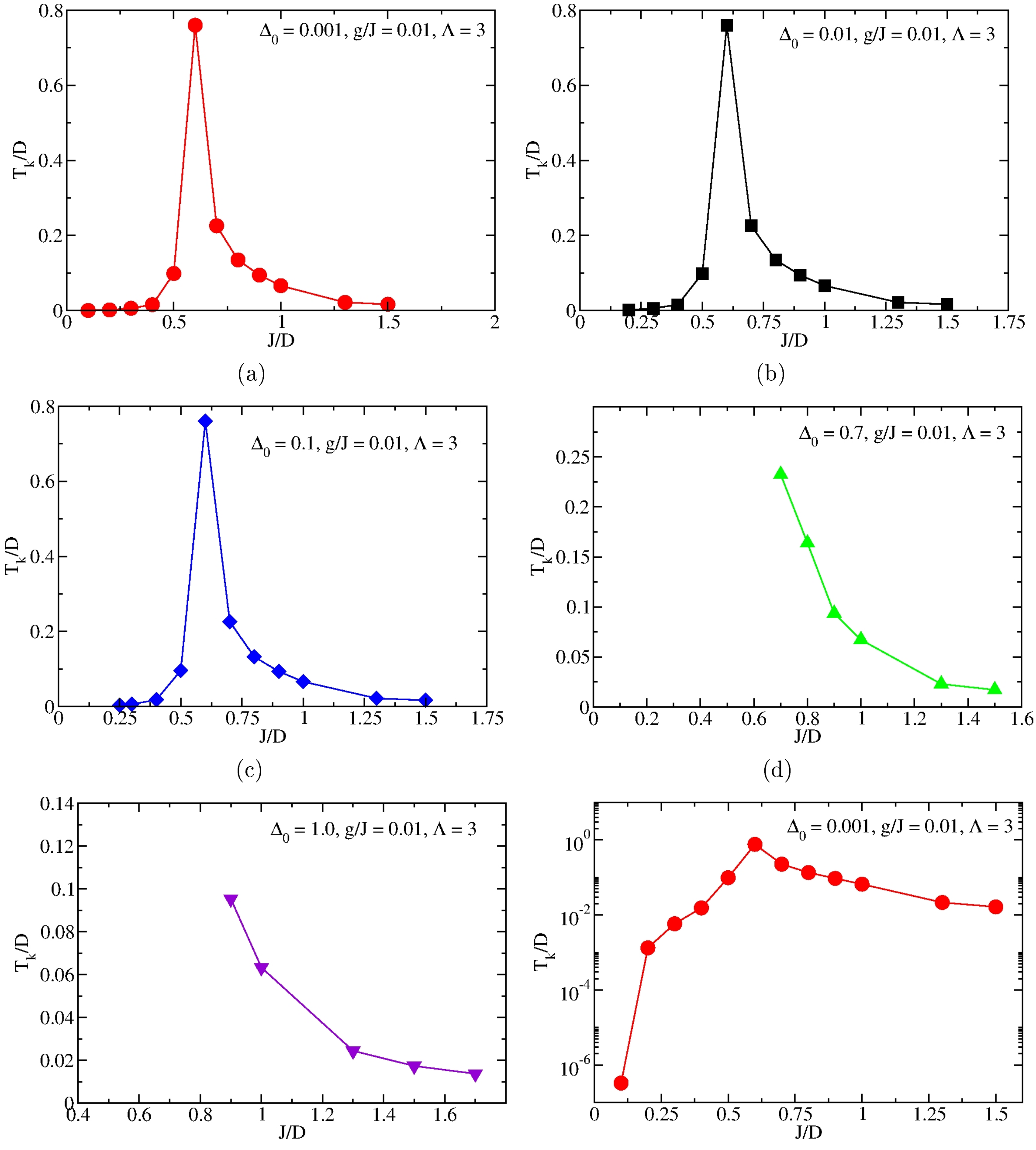

(a) (b) (c) (d) (e) (f)

Figure 6.7: T_K dependence on coupling strength for the following common parameters: $g/J = 0.01$, $\Lambda = 3$, (a) At $\Delta_0 = 0.001$ the system needs a very small minimum coupling constant in order to reach the 2CK regime and we start at $J = 0.1$, (b) For $\Delta_0 = 0.01$ the minimum coupling is $J = 0.2$, (c) while for $\Delta_0 = 0.1$, minimum $J = 0.25$, (d) $\Delta_0 = 0.7$, is the critical Δ_0 where T_K decreases for any coupling that flows to the 2CK regime and $J = 0.7$ is the minimum coupling constant. (e) For $\Delta_0 = 1.0$ the minimum coupling is $J = 0.9$, (f) is the log plot of T_K against the bare coupling constant.

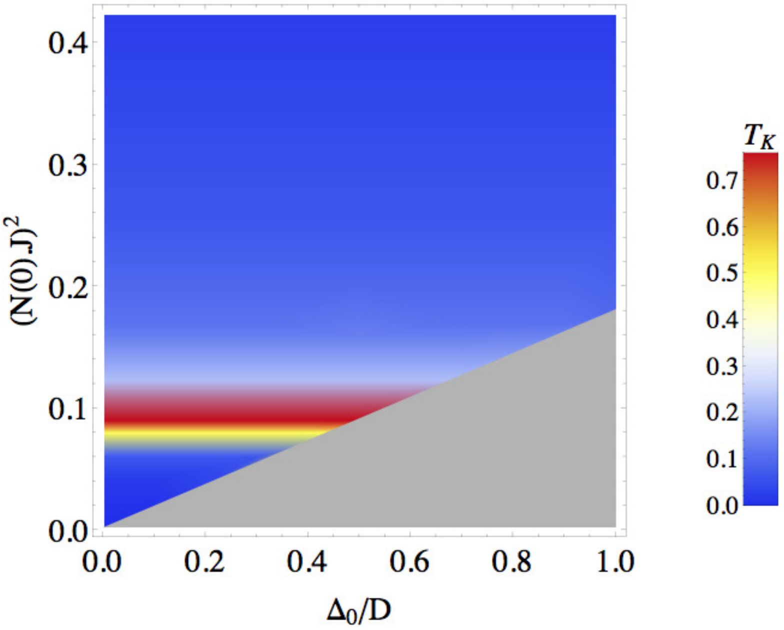

Figure 6.8: The change of T_K on the surface of J^2 and Δ_0 which shows that for certain values of Δ_0, T_K peaks at the red color and decays exponentially on both sides, whereas for certain values it only decreases. The gray part of the plot is the region where the Kondo temperature T_K is not defined and it corresponds to the potential scattering phase already mentioned in the phase diagram. For detailed explanation on this, see text.

partially broken SU(3) Kondo model shows an exponential increase and decrease of T_K for small and large coupling constant J, respectively when the level spacing $\Delta_0 < 0.7$ as shown in Fig. 6.7(a), Fig. 6.7(b), and Fig. 6.7(c) and an exponential decrease of T_K for $\Delta_0 \geq 0.7$ values as shown in Fig. 6.7(d) and Fig. 6.7(e). While Fig. 6.7(f) shows a log plot of T_K against the bare couplings. One sees that T_K values are the same in all the figures irrespective of the value of Δ_0 as long as the couplings are strong enough for the 2CK effect to be observed. A careful look at Fig. 6.7(a), Fig. 6.7(b), Fig. 6.7(c), Fig. 6.7(d), and Fig. 6.7(e), shows that the first data point is shifted from left to right as Δ_0 is increased. This simply tells us that large Δ_0 requires a large J value. The raison d'etre for this behavior is that, whenever the coupling is strong enough to renormalize Δ_0 down to at least zero or negative values then the system is able to flow to the 2CK regime. Consequently T_K can be calculated. These T_K plots confirm the fact that T_K depends only on the coupling constant and not the level spacing in this model. Unlike in the TLS where T_K is somehow tied to the level spacing as already expounded in chapter 4. The Kondo temperature is calculated here using standard procedure of the NRG method. It is determined as the energy scale where the NRG first excited energy level reaches its fixed point value within, for instance 10%. There are other methods to calculate T_K but the complexity of the level flow makes it difficult to use them.

One observes that for $\Delta_0 \geq 0.7$, the system is always in the regime where T_K decreases as the bare coupling increases. This could be explained by the fact that a level crossing occurs when the couplings have already grown large such that we are already in the regime where T_K decreases with increase in the bare coupling. The above explanation is supported by the fact that when $\Delta_0 < 0.7$, the results in [32] are recovered.

Fig. 6.8 shows a density plot of the variation of T_K with coupling constant and the level spacing. The Kondo temperature T_K is color coded, while the x and y-axes are the level spacing and the dimensionless coupling, respectively. The sidebar beside shows the numeric values of T_K with respect to the colors in the 2CK phase. T_K peaks at the red color and its minimum is at blue. The gray part of the plot is the potential scattering phase where the Kondo temperature T_K is not defined. The important physics that can be read off Fig. 6.8 is that T_K is translational invariant from left to right. This means that Δ_0 has no influence on T_K as long as the coupling strength is strong enough to renormalize it down to at least zero or negative. The density plot of Fig. 6.8 shows that the partially broken SU(3) rotational impurity model exhibit for low energies a duality between the weak and strong bare Kondo coupling for level spacing $\Delta_0 < 0.7$. The physics of this behavior has been explicitly explained in chapter 3. The fact that this duality behavior is indeed seen in the model under investigation here further reasserts Arnold et al.'s proposal of this model as a realistic model for the 2CK effect [2].

6.3.4 Entropy

The calculation of thermodynamic quantities using the NRG technique has already been dealt with in chapter 5. Here we focus more on the physics that is obtained from these calculations and what we can learn from it. As we have already learned in subsection 6.2.3 about the 1CK entropy, the entropy of the impurity always reduces with the RG flow. It is therefore necessary for us to concentrate on how the impurity entropy changes as the temperature is lowered in the 2CK scenario in both the partially broken SU(3) and full SU(3) symmetry of the model in question. In Fig. 6.9(a) and Fig. 6.9(c) we show the entropy as a function of T/T_K for the SU(3) Kondo model. We rather show in Fig. 6.9(b) the entropy as a function of T since the Kondo regime is not reached with the couplings used. The value of T_K is obtained using the following formula

$$T_K \approx D\Lambda^{-N/2} \tag{6.12}$$

where N is the iteration number where the energies cross over to the 2CK fixed point. How the value of N is obtained has been explained above in section 6.3.3 about 2CK duality behavior. The NRG calculations are carried out keeping 2000 states in each step and using the discretization parameter $\Lambda = 4$. A comparatively large value of $\Lambda = 4$ is used and the reason for this is because it considerably reduces the number of states that are kept in each NRG iteration step. It has been shown in [50] that this Λ value is still acceptable for the calculation of static thermodynamic properties.

As already discussed in the section on 1CK entropy, the inverse temperature value depends on the value of Λ and the number of states kept. Detailed information about this can be found in [50]. Here we use inverse temperature β values from 1.2 to 1.5. The values of β within this range give us physically reasonable results for the entropy calculations. For numerical details on how the entropy is calculated using the NRG, see Appendix D.

One sees in Fig. 6.9(a) the partial quenching of the impurity pseudo spin by the Kondo effect as the temperature is decreased down to the order of T_K. There are three plateaus in Fig. 6.9(a), the first one is when the impurity is free at temperature ($T \gg \Delta_0$), so that the three levels all contribute to the entropy before the RG procedure. When RG is applied, there is a flow in which the two excited doublet are renormalized downward and eventually cross over the singlet state to become the ground states. The energy scale of this crossover as shown in Fig. 6.9(a) is of the order of Δ_0. The second plateau is then

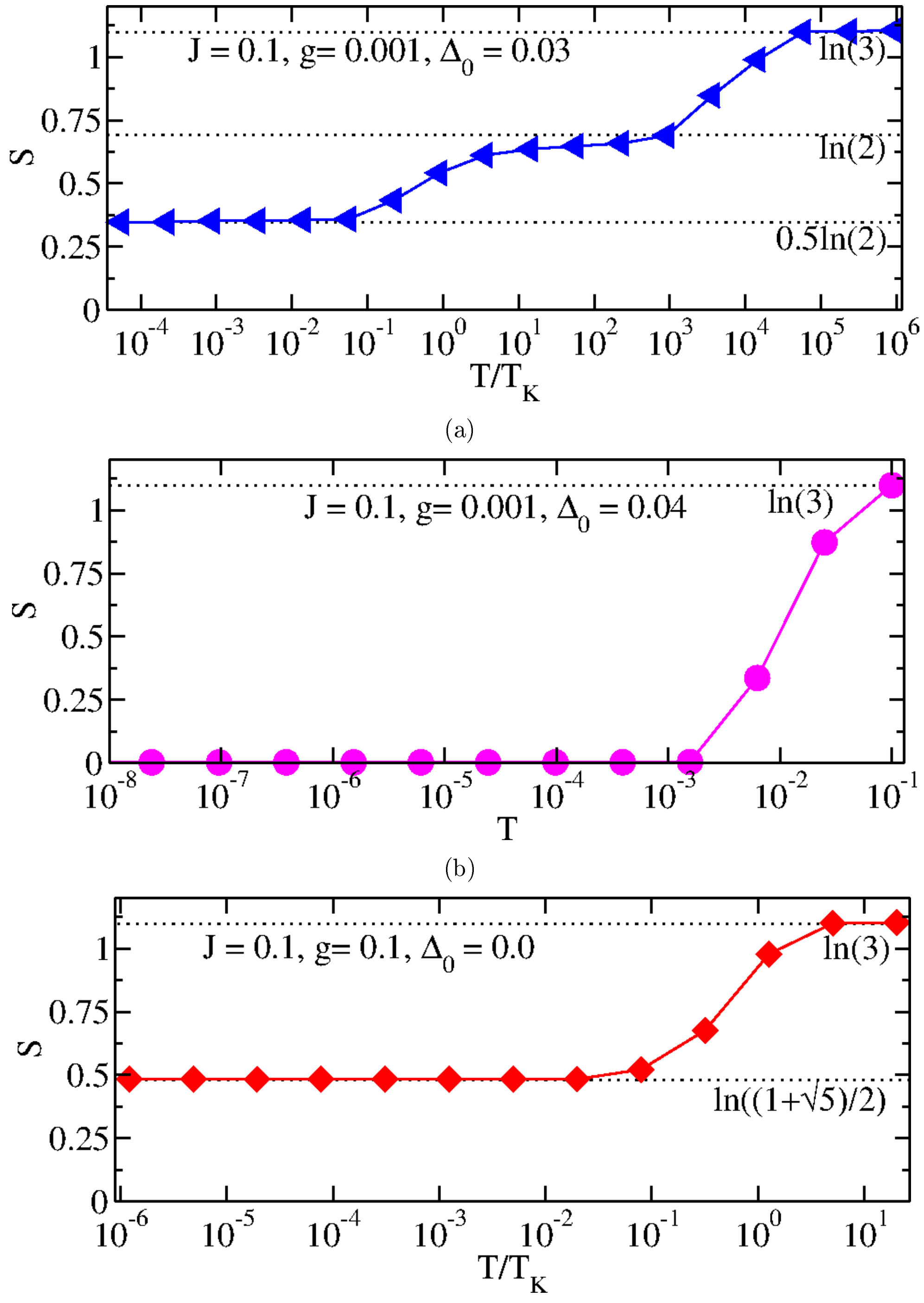

(a)

(b)

(c)

Figure 6.9: The impurity entropy without magnetic field in the 2CK scenario for the following general parameter: $J = 0.1$, $\Lambda = 4$, (a) Impurity entropy when there is a flow to the 2CK regime for $g/J = 0.01$ and $\Delta_0 = 0.03$, (b) The entropy of the impurity in the potential scattering phase for $g/J = 0.01$ and $\Delta_0 = 0.04$, (c) Entropy of impurity in a full SU(3) symmetric case when $\Delta_0 = 0.0$ and $g = J$. For details of the explanation of these figures, see text.

that of the new ground states from the doublet and it is at ln2 as shown in Fig. 6.9(a). As the temperature continues to decrease, then at energies of the order of T_K, Kondo screening sets in and the impurity is partially screened leading to a residual entropy of $\frac{1}{2}$ln2 which can be seen in Fig. 6.9(a); hence the third plateau.

In Fig. 6.9(b), one can evidently see that the entropy of the impurity flows from ln3 to ln1. The reason for this is because the coupling constant is not strong enough to renormalize Δ_0 downward to at least zero. The coupling constant value in Fig. 6.9(b) is the same as in Fig. 6.9(a). The Δ_0 value has been increased by 0.01 thereby making it impossible for the crossover of the doublet states to occur and the singlet state remains the unique ground state consequently no 2CK effect is observed. The system remains in the potential scattering regime. Because no 2CK effect is perceived in the case of Fig. 6.9(b) so we plot the entropy as a function of temperature rather than the ratio T/T_K as in Fig. 6.9(a) and Fig. 6.9(c).

Last but not least on this section on entropy is the case where the partially broken symmetry is lifted by setting $\Delta_0 = 0$. In this case the impurity has a ground state of three degenerate levels. Fig. 6.9(c) shows that as the RG is applied the impurity entropy flows from ln3 down to $\ln(\frac{1+\sqrt{5}}{2})$ which is the expect value when three levels are screened in the 2CK effect as deduced in conformal field theory (CFT).

6.3.5 The effect of magnetic fields on the fixed point

In this subsection we investigate how small magnetic fields affect the stability of a fixed point in the partially broken SU(3) Kondo model. We focus our attention only on the 2CK case because we can easily compare our results to the perturbative renormalization group (PRG) results of the effect of magnetic field on this model as shown in [19]. When a small magnetic field is applied on the impurity, the excited doublet is split by the Zeeman effect that is, its degeneracy is apparently lifted. The impurity levels with magnetic field look as in Fig. 6.10. The Hamiltonian is also modified so as to factor in the effect of the magnetic field by adding the following term to (4.2)

$$\frac{B_0}{2}\sum_{m=\pm1} m f_m^{\dagger} f_m \tag{6.13}$$

The effect of the magnetic field on the fixed point have been studied by Ballmann in [61] in details. In [61], Ballmann looks at the flows of the states $m = \pm 1$ when they are slightly split by the magnetic field. She calculated the self-energy of the impurity levels during the renormalization group (RG) process, which changes with the flow. The imaginary part of the self-energy describes the life time effects; she could show that the

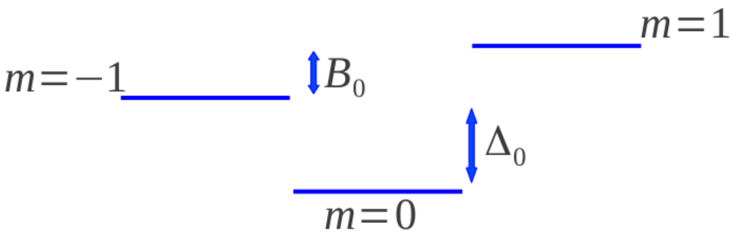

Figure 6.10: Level scheme of the impurity with a magnetic field.

life time of the levels $m = \pm 1$ turns to zero as the temperature is lowered in the course of the RG flow whereas that of $m = 0$ becomes finite. With the preceding statement one can make a statement on whether the degenerate levels did cross over or not to become the ground states. With the NRG method used here, we rather look at the behavior of the entropy of the impurity as the temperature is lowered. This approach is much better since we deal with many-bodies unlike the self-energy impurity levels approach that is used in [61]. We apply small magnetic fields to the impurity and look at how the fixed point is affected by this. We have already discussed the behavior of the entropy of the impurity as the system flows from high temperature down to very low temperature. We have seen that whenever the 2CK effect is observed, the impurity entropy flows to $\frac{1}{2}\ln 2$ at low temperature and when the 2CK effect is not observed then the system flows to the potential scattering regime where the ground state is the singlet $m = 0$. In this scenario the entropy flows to zero since $\ln 1 = 0$.

When a small magnetic field of the order of $10^{-4}D_0$ ($B_0 > T_K$), where $D_0 = 1eV$ is the half bandwidth at the start of the RG scheme, is applied to the impurity at one of the fixed points in Fig. 6.6 with the following parameters; $J = 0.1$, $g/J = 0.01$, and $\Delta_0 = 0.03$, the system flows away from the 2CK phase into the potential scattering phase. However, when the coupling strength is increased to $J = 0.13$ with the other parameters remaining constant, then the system flows back to the 2CK phase. One can therefore conclude that this model still shows 2CK behavior even under the influence of the magnetic field as long as the coupling constants are strong enough to enhance the crossover to occur. When $B_0 < T_K$ the fixed point is not affected by the magnetic field and the fixed point is still reached as in the case of no magnetic field with the same couplings. The reason for this is that the energy scale from the magnetic field is lower than that from T_K and hence 2CK fixed point is not perturbed by this magnetic field. The crossover of the levels is pivotal for the occurrence of the 2CK effect in the model. This means that in the phase diagram, Fig. 6.6, the presence of the magnetic field simply shifts the phase lines to the left. In Fig. 6.11(a) and Fig. 6.11(b) we show the entropy contribution of the impurity to the system in the presence of a small magnetic field and the corresponding parameters mentioned above. In Fig. 6.11(a) one sees that the impurity entropy flows from ln3 directly to ln1 without passing through ln2 as in the case where there is a crossover. When there is no crossover the degenerate doublet never becomes the ground states and can not be energetically occupied at low temperature hence no resonance scattering. The system ends up with the singlet ground state that just acts as a potential scatterer. Hence the entropy flows directly from ln3 to ln1. But when the coupling strength is slightly increased by 0.03 as in Fig. 6.11(b), then the impurity contribution to the system shows again the behavior that attests to the fact that the 2CK effect indeed happens. As previously mentioned above in the course of the renormalization process the impurity entropy reduces from that of the free impurity to that of the ground state as the temperature tends to zero. This behavior explains the plateaus in the impurity entropy as the temperature is lowered.

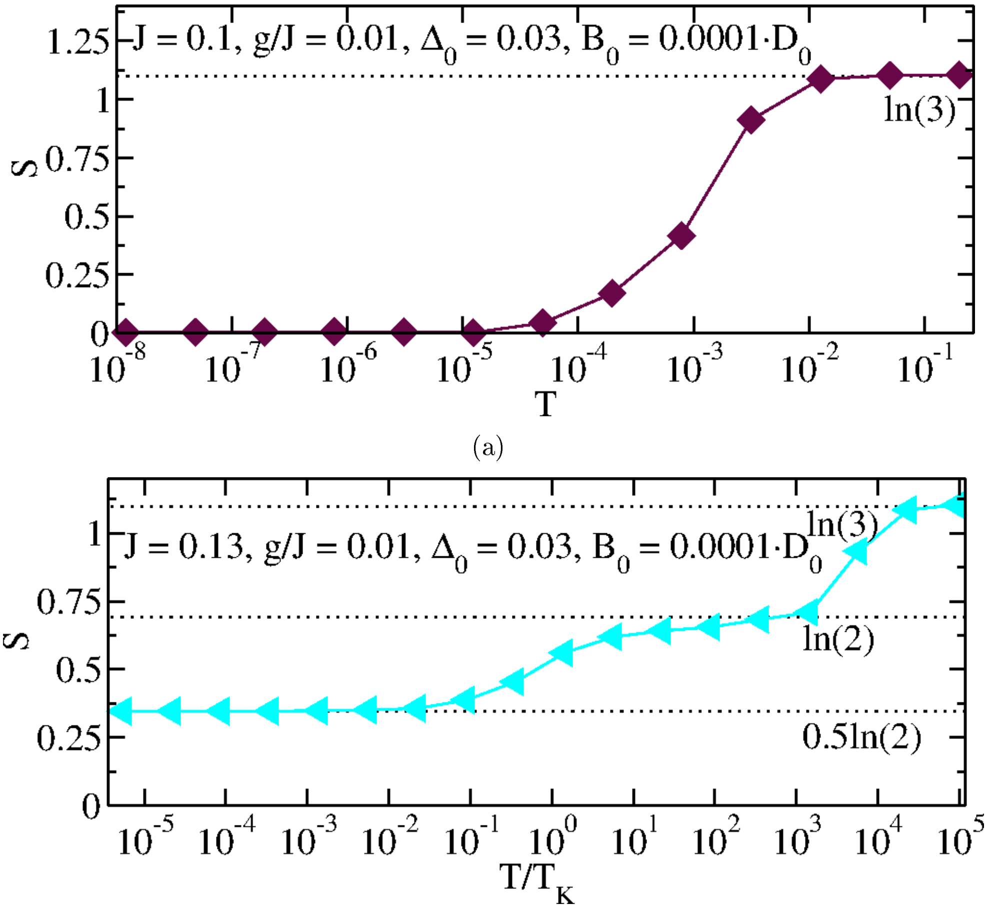

(a)

(b)

Figure 6.11: The impurity entropy with magnetic field in the 2CK scenario for the following general parameter: $B_0 = 0.0001$ and $\Lambda = 4$,(a) The entropy of the impurity in the potential scattering phase for $J = 0.1$, $g/J = 0.01$, and $\Delta_0 = 0.03$, (b) Impurity entropy when there is a crossover to the 2CK regime for $J = 0.13$, $g/J = 0.01$, and $\Delta_0 = 0.03$. For details of the explanation of these figures, see text.

Chapter 7

Conclusion and Outlook

This thesis has centered around the application of the numerical renormalization group (NRG) to the partially broken SU(3) Kondo model. For a better understanding of the thesis, we started up by giving a very broad introduction of the Kondo effect and some of the methods used to comprehend this interesting physics. Furthermore, we briefly presented non-magnetic impurity Kondo models like the two-level system (TLS) and the partially broken SU(3) Kondo model. We also dealt with the NRG method in order to facilitate the comprehension of the reason of the application of this particular method to the model in question in this work.

We have confirmed that the partially broken SU(3) rotational impurity model has a two-channel Kondo fixed point in a wide parameter regime. We have shown that the phase diagram obtained by the NRG calculations qualitatively agrees with that obtained with the perturbative renormalization group (PRB) method in [2]. We have also shown that the Kondo temperature T_K dependence on the bare coupling constant J peaks at $J = 0.6$ and decays exponentially on both sides of the peak. This duality behavior is a characteristic of the two-channel Kondo (2CK) effect. However, we have also demonstrated that this duality behavior is only seen when $\Delta_0 < 0.7$ since both small and strong couplings J are able to down-renormalize the energy level spacing Δ_0 to at least zero. For $\Delta_0 \geq 0.7$, the couplings J necessary to downward renormalize Δ_0 are already in the strong coupling regime where T_K decreases with increase in coupling strength.

We have also shown that the single-channel Kondo (1CK) behavior of this model agrees with the spin-1/2 impurity case of the Kondo model. In addition, we have calculated the impurity contribution to the entropy of the system in both the single- and two-channel cases, which has shed more light on the crossover of the excited doublet. The impurity entropy flows from high temperature down to low temperature passing through a plateau at $S(T_K < T < \Delta_0) = k_B \ln 2$ after starting out at $S(T \gg \Delta_0) = k_B \ln 3$ and flows down to $S(0) = k_B \ln 1$ in the 1CK scenario, while in the 2CK case, it flows to $S(0) = \frac{1}{2} k_B \ln 2$. In the case where $\Delta_0 = 0$, the entropy flows from $S(T \gg \Delta_0) = k_B \ln 3$ directly to $S(0) = k_B \ln(\frac{1+\sqrt{5}}{2})$ in the 2CK. The preceding behavior of the entropy is all in the situation in which the system reaches the Kondo fixed point. When the system does not reach the 2CK fixed point, the entropy flows from $S(T \gg \Delta_0) = k_B \ln 3$ straight to $S(0) = k_B \ln 1$. This has therefore vindicated the prediction by Arnold et al. in [2] that a crossover occurs during the course of RG in which the degenerate excited states cross over the singlet state at low temperatures to become the ground states. This crossover behavior is clearly seen in the impurity entropy as the temperature is lowered down to zero. We have also shown that the fixed point in the partially broken SU(3) model is quite unstable to small magnetic fields and that the magnetic fields shift the phase lines in the phase diagram to the left.

We have equally shown that when $\Delta_0 < 0$ in the partially broken SU(3) Kondo model, then it behaves exactly as the spin-1/2 2CK Kondo. This is because for $\Delta_0 < 0$, the degenerate states are already the ground states and so resonance scattering sets in as the temperature is decreased. The energy flows of the system elucidate this idea very well as they are identical to those of the spin-1/2 Kondo model.

The code we wrote for this work has just two kinds of symmetries, that is the total charge U(1) and the z-component of the total spin S_z U(1). This helps to reduce the Hilbert space but still it takes a lot of time for us to get results. As an outlook, it will be necessary to add more symmetries to the code so that the computing time and memory required for running the code is greatly reduced. One could add the total spin symmetry which is very delicate and is broken by the presence of magnetic fields. This means that the addition of this symmetry will hinder the study of small magnetic field effects on the fixed point of this model. Nevertheless, its benefits are enormous because it will greatly reduce the time for a complete run of the NRG scheme. One could equally figure out more symmetries of the model that could be made use of, hence making the entire problem more easily tractable. This could enable the calculation of the spectral function and other physical properties of the model to be compared with experiments.

Appendix A

Numerical renormalization group details

The numerical renormalization group (NRG) details have been worked out by Wilson for the Kondo model in [1]. For the sake of completeness we show how he derived the NRG equations and also give the rationale behind the assumptions he made. The following Kondo model Hamiltonian is used to derive the different equations

$$\begin{aligned} H_K &= J_K \mathbf{S}_d \cdot \mathbf{s}_0 + \sum_{\mathbf{k},\sigma} \varepsilon_{\mathbf{k}} c^\dagger_{\mathbf{k},\sigma} c_{\mathbf{k},\sigma} \\ &= H_i + H_c \end{aligned} \tag{A.1}$$

H_i is the interaction term whereas H_c is the kinetic term of the conduction band electrons, where $\mathbf{s}_0 = c^\dagger_{0,\sigma} \vec{\sigma}_{\sigma\mu} c_{0,\mu}$ and a localized Wannier state generated by $c_{0,\sigma} = \sum_k c_{k,\sigma}$. $\mathbf{S}_d$ is the electronic impurity spin operator which is a localized spin-1/2.

A.1 Logarithmic discretization

We follow the explicit approach described in [50] to demonstrate how the discretization of the conduction band is carried out. The continuous nature of the conduction band makes computer calculations intractable. The way around this is to discretize the conduction band. The major issue is usually the choice of the discretization scheme to use. Wilson used the logarithmic discretization scheme because it resolves low energy states with high accuracy while also taking the high energy states into consideration. The logarithmic discretization of the conduction band also leads to coefficients that fall off exponentially as more electrons are added to the Wilson chain. The idea of the Wilson chain will be explained in the next section. Fig. A.1 shows how the conduction band is split into intervals. The following approximation is used to replace the continuum band with a discrete one

$$H_c = \int_{-1}^{+} d\varepsilon\, \varepsilon c^\dagger_{\varepsilon,\sigma} c_{\varepsilon,\sigma} \approx \sum_{n=0}^{\infty} (\varepsilon_{-n} c^\dagger_{-n,\sigma} c_{-n,\sigma} + \varepsilon_n c^\dagger_{n,\sigma} c_{n,\sigma}), \tag{A.2}$$

where $c^\dagger_{\varepsilon,\sigma}$ ($c_{\varepsilon,\sigma}$) are the creation (annihilation) operators on conduction sea, respectively, whereas ε_n is the on-site energy on the corresponding n-site of the conduction sea. The parameter $\Lambda > 1$ defines a set of intervals with the following discretization points

$$x_n = \pm\Lambda, \;\; n = 0, 1, 2.... \tag{A.3}$$

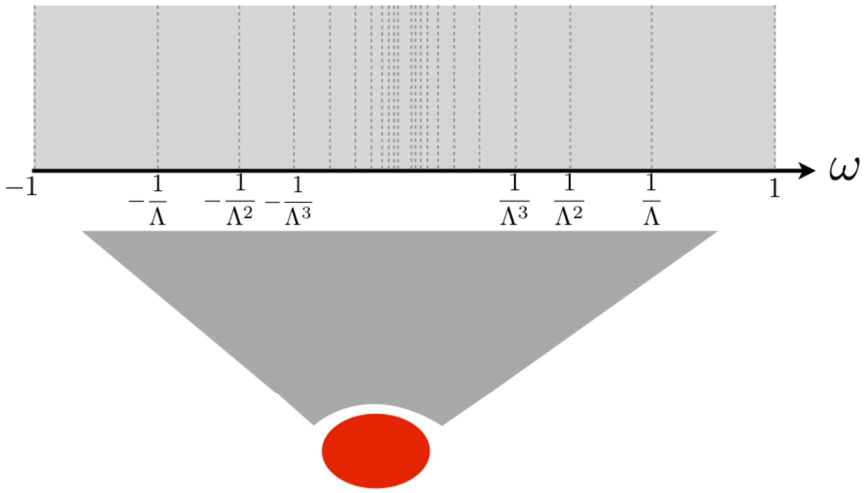

Figure A.1: The logarithmic discretization of the conduction band. The red oval represents the impurity that couples to all the different energies scales of the conduction band. This set of logarithmic intervals is ushered in via the NRG discretization parameter Λ.

Each of the intervals has a width

$$d_n = \Lambda^{-n}(1-\Lambda^{-1}) \tag{A.4}$$

In order to analyze this discrete intervals, a complete orthonormal basis set of functions is introduced in each of the intervals.

$$\psi^{\pm}_{np}(\varepsilon) = \begin{cases} \frac{1}{\sqrt{d_n}} e^{\pm i\omega_n p\varepsilon} & \text{for } x_{n+1}<\pm\varepsilon<x_n, \\ 0 & \text{outside this interval} \end{cases} \tag{A.5}$$

p is an integer value from $-\infty$ to $+\infty$ and plays the role of the Fourier harmonic index and $\omega_n = 2\pi/d_n$ is the fundamental frequency of each interval. The conduction electrons operators $c_{\varepsilon\sigma}$ are now expanded in this new basis.

$$c_{\varepsilon\sigma} = \sum_{np}[a_{np\sigma}\psi^{+}_{np}(\varepsilon) + b_{np\sigma}\psi^{-}_{np}(\varepsilon)] \tag{A.6}$$

where $a_{np\sigma}$, $b_{np\sigma}$ constitute a complete set of new operators and are labeled with respect to the interval n and p, the harmonic index. The above expression of $c_{\varepsilon\sigma}$ is then substituted in (A.1) and one thus obtains the following Hamiltonian

$$\begin{aligned} H_K = {} & \frac{1}{2}(1+\Lambda^{-1})\sum_{np}\Lambda^{-n}(a^{\dagger}_{np\sigma}a_{np\sigma} - b^{\dagger}_{np\sigma}b_{np\sigma}) \\ & + \frac{(1-\Lambda^{-1})}{2\pi i}\sum_{n}\sum_{p\neq p'}\Lambda^{-n}(a^{\dagger}_{np\sigma}a_{np'\sigma} - b^{\dagger}_{np\sigma}b_{np'\sigma})e^{\frac{2\pi i(p-p')}{1-\Lambda^{-1}}} \\ & + Jc^{\dagger}_{0,\sigma}\sigma_{\sigma\mu}c_{0,\mu}.\mathbf{S} \end{aligned} \tag{A.7}$$

The operators $a_{np\sigma}$, $b_{np\sigma}$ and their hermitian conjugates obey the usual anticommuntation rules for fermions. $a_{np\sigma}$ acts in the positive range whereas $b_{np\sigma}$ in the negative range of the intervals. In terms of the new operators the localized state has the following expression

$$c^{\dagger}_{0,\sigma} = (1-\Lambda^{-1})^{1/2}\sum_{n}\Lambda^{-n/2}(a^{\dagger}_{0p\sigma} + b^{\dagger}_{0p\sigma}) \tag{A.8}$$

This is where the approximation comes in, by neglecting all the terms with $p \neq 0$. This means that all higher terms in the Fourier series are dropped, which physically means that only one electron per logarithmic interval is kept. This approximation is logical since the impurity only couples indirectly to states with $p \neq 0$ and so this coupling is weak and can thus be neglected. Neglecting these states is equivalent to neglecting the off-diagonal matrix elements, which are proportional to $(1 - \Lambda^{-1})$ and the approximation becomes valid as $\Lambda \rightarrow 1$. The discretization parameter Λ is always adjusted correctly in order to obtain reasonable results. If Λ is too close to unity then the system will not converge sufficiently quickly and if it is large compared to unity then the error due to the logarithmic discretization becomes huge. For practical NRG calculations for the single channel case one generally choses $\Lambda = 2$ and for the two-channel case $\Lambda = 3$.

A.2 Mapping onto a semi infinite chain

A.2.1 Lanczos procedure

The Lanczos procedure is used to transform the kinetic energy part of the conduction band to a new set of operators. It takes it from the diagonal form to the tridiagonal form. This goal is attained by constructing a sequence of orthogonal states generated by repeatedly applying the kinetic part of the Kondo Hamiltonian to the vacuum state as shown below

$$|1\rangle = \frac{1}{t_0}[H_c|0\rangle - |0\rangle\langle 0|H_c|0\rangle] \tag{A.9}$$

$$|n+1\rangle = \frac{1}{t_n}[H_c|n\rangle - |n\rangle\langle n|H_c|n\rangle - |n-1\rangle\langle n-1|H_c|n\rangle] \tag{A.10}$$

Using the expression for H_c and dropping the spin index for simplicity, one obtains

$$H_c = \sum_{n=0}^{\infty}[\epsilon_n c_n^{\dagger} c_n + t_n(c_n^{\dagger} c_{n+1} + H.c)] \tag{A.11}$$

where $\epsilon_n = \langle n|H_c|n\rangle$ and $t_n = \langle n+1|H_c|n\rangle$ are the Lanczos coefficients which depend on the dispersion. For most cases, these Lanczos coefficients do not fall off with n. The falling off of this coefficients is a behavior necessary for the convergence of the NRG scheme. This problem is solved by the logarithmic discretization of the conduction band which ensures that these coefficients fall off exponentially with n.

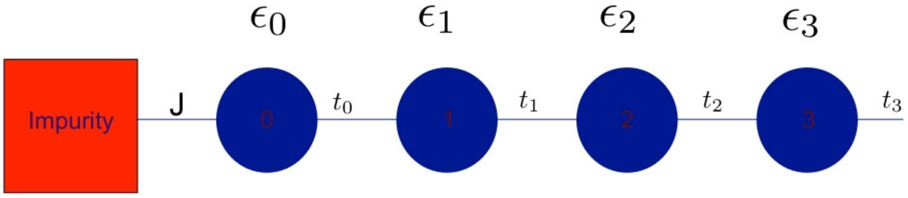

Figure A.2: The Wilson chain with the first site in red being the impurity and the blue sites are the conduction electron. ϵ are the on-site energies while t are the hopping matrix elements between two sites.

A.3 Iterative diagonalization

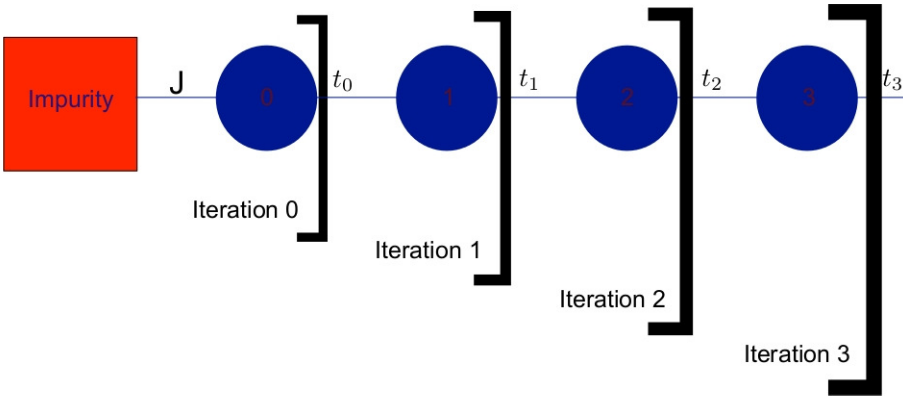

Figure A.3: Iterative diagonalization of the Wilson chain with neighboring sites coupled to one another. The impurity couples to the first conduction electron and the chain parameters are ε_n and t_n

The renormalization group (RG) scheme is illustrated in Fig. A.3 where the iteration starts up with the impurity and an electron on the first site of the chain. This Hamiltonian is diagonalized. The Hamiltonian say H_N is now coupled to the $(N+1)-th$ site of the Wilson chain consequently setting up the Hamiltonian, H_{N+1} in which the diagonalization procedure is also carried out on it. This gives us a series of Hamiltonians that approaches H_K as $N \rightarrow \infty$

$$H_K = \lim_{N \to +\infty} \Lambda^{-(N-1)/2} H_N \tag{A.12}$$

where the Hamiltonian H_N is made up of the first N sites of the Wilson chain and has the form

$$H_N = \Lambda^{(N-1)/2} \left(J\mathbf{S_d} \cdot \mathbf{s_0} + \sum_{N=0,\sigma}^{N} [\epsilon_N c^{\dagger}_{N\sigma} c_{N\sigma} + t_N (c^{\dagger}_{N\sigma} c_{N+1\sigma} + c^{\dagger}_{N+1\sigma} c_{N\sigma})] \right) \tag{A.13}$$

The role of $\Lambda^{(N-1)/2}$ is to suppress the N dependence of the hopping matrix elements t_{N-1} between the last two sites of H_N. This rescaling is important because it ensures that the energies obtained are of order 1. Knowing H_N enables us to set up the iteration equation as follows

$$H_{N+1} = \sqrt{\Lambda} H_N + \sum_{\sigma} [\epsilon_{N+1} c^{\dagger}_{N+1\sigma} c_{N+1\sigma} + t_N (c^{\dagger}_{N\sigma} c_{N+1\sigma} + c^{\dagger}_{N+1\sigma} c_{N\sigma})] \tag{A.14}$$

(A.14) shows how two successive Hamiltonians are related in the Wilson chain which leads to the following recursion relationship

$$H_{N+1} = R(H_N) \tag{A.15}$$

where R is the RG transformations.

Appendix B

Calculation of starting matrices for the numerical renormalization group procedure

We have considered only the two U(1) symmetries of the model that are generated by the charge operators, Q and the z-component of the total spin, S_z. The multiplets of the Hamiltonian are classified according to these quantum numbers, Q and S_z. The hopping operators are not related by symmetries and one has to keep track of three operators in the 1CK case (since the electrons are polarized) and six operators in the 2CK case (degeneracy of electron magnetic spin) namely $c^{\dagger}_{-1\uparrow}$, $c^{\dagger}_{0\uparrow}$, $c^{\dagger}_{1\uparrow}$, $c^{\dagger}_{-1\downarrow}$, $c^{\dagger}_{1\downarrow}$, $c^{\dagger}_{1\downarrow}$. The initial block states and the matrix elements of the hopping operators must be constructed before the start of the computation since they serve as input data for the NRG procedure. The first step in this regards is to identify all the states of the system at the beginning. To do this, one takes a vacuum state $|0\rangle$ and then acts the above mentioned operators to it. This operation is explicitly carried out below to show how these states are created. It turns out that for the 1CK and 2CK cases, there are 8 and 64 possible states at each site hence the Hilbert space grows by a factor of 8 and 64 upon the addition of a new site, respectively. The input NRG Hamiltonian has a dimension of 24×24 and 192×192 for 1CK and 2CK since the impurity has three states and each of these states couples to the 8 and 64 states of the conduction electron site, respectively.

B.1 Single-channel Kondo case

The possible basis states in the 1CK scenario are the following $|0\rangle$, $c^{\dagger}_{-1}|0\rangle$, $c^{\dagger}_{0}|0\rangle$, $c^{\dagger}_{1}|0\rangle$, $c^{\dagger}_{-1}c^{\dagger}_{0}|0\rangle$, $c^{\dagger}_{1}c^{\dagger}_{0}|0\rangle$, $c^{\dagger}_{-1}c^{\dagger}_{1}|0\rangle$, $c^{\dagger}_{-1}c^{\dagger}_{1}c^{\dagger}_{0}|0\rangle$. If the above basis states are denoted by say $|u\rangle$ then the fermionic operators are obtained by the following computation

$$c^{\dagger}_{m\sigma} = \ {}_{n}\langle u|c^{\dagger}_{m\sigma}|u\rangle_{n} \tag{B.1}$$

where n is a positive integer. Using (B.1) one obtains the following hopping operators

$$c^\dagger_{-1} = \begin{array}{c|cccccccc} & |0\rangle & c^\dagger_{-1}|0\rangle & c^\dagger_0|0\rangle & c^\dagger_1|0\rangle & c^\dagger_0 c^\dagger_{-1}|0\rangle & c^\dagger_1 c^\dagger_{-1}|0\rangle & c^\dagger_1 c^\dagger_0|0\rangle & c^\dagger_1 c^\dagger_0 c^\dagger_{-1}|0\rangle \\ \hline |0\rangle & 0 & 0 & 0 & 0 & 0 & 0 & 0 & 0 \\ c^\dagger_{-1}|0\rangle & 1 & 0 & 0 & 0 & 0 & 0 & 0 & 0 \\ c^\dagger_0|0\rangle & 0 & 0 & 0 & 0 & 0 & 0 & 0 & 0 \\ c^\dagger_1|0\rangle & 0 & 0 & 0 & 0 & 0 & 0 & 0 & 0 \\ c^\dagger_0 c^\dagger_{-1}|0\rangle & 0 & 0 & -1 & 0 & 0 & 0 & 0 & 0 \\ c^\dagger_1 c^\dagger_{-1}|0\rangle & 0 & 0 & 0 & -1 & 0 & 0 & 0 & 0 \\ c^\dagger_1 c^\dagger_0|0\rangle & 0 & 0 & 0 & 0 & 0 & 0 & 0 & 0 \\ c^\dagger_1 c^\dagger_0 c^\dagger_{-1}|0\rangle & 0 & 0 & 0 & 0 & 0 & 0 & 1 & 0 \end{array} \tag{B.2}$$

$$c^\dagger_{0} = \begin{array}{c|cccccccc} & |0\rangle & c^\dagger_{-1}|0\rangle & c^\dagger_0|0\rangle & c^\dagger_1|0\rangle & c^\dagger_0 c^\dagger_{-1}|0\rangle & c^\dagger_1 c^\dagger_{-1}|0\rangle & c^\dagger_1 c^\dagger_0|0\rangle & c^\dagger_1 c^\dagger_0 c^\dagger_{-1}|0\rangle \\ \hline |0\rangle & 0 & 0 & 0 & 0 & 0 & 0 & 0 & 0 \\ c^\dagger_{-1}|0\rangle & 0 & 0 & 0 & 0 & 0 & 0 & 0 & 0 \\ c^\dagger_0|0\rangle & 1 & 0 & 0 & 0 & 0 & 0 & 0 & 0 \\ c^\dagger_1|0\rangle & 0 & 0 & 0 & 0 & 0 & 0 & 0 & 0 \\ c^\dagger_0 c^\dagger_{-1}|0\rangle & 0 & 1 & 0 & 0 & 0 & 0 & 0 & 0 \\ c^\dagger_1 c^\dagger_{-1}|0\rangle & 0 & 0 & 0 & 0 & 0 & 0 & 0 & 0 \\ c^\dagger_1 c^\dagger_0|0\rangle & 0 & 0 & 0 & -1 & 0 & 0 & 0 & 0 \\ c^\dagger_1 c^\dagger_0 c^\dagger_{-1}|0\rangle & 0 & 0 & 0 & 0 & 0 & -1 & 0 & 0 \end{array} \tag{B.3}$$

$$c^\dagger_{1} = \begin{array}{c|cccccccc} & |0\rangle & c^\dagger_{-1}|0\rangle & c^\dagger_0|0\rangle & c^\dagger_1|0\rangle & c^\dagger_0 c^\dagger_{-1}|0\rangle & c^\dagger_1 c^\dagger_{-1}|0\rangle & c^\dagger_1 c^\dagger_0|0\rangle & c^\dagger_1 c^\dagger_0 c^\dagger_{-1}|0\rangle \\ \hline |0\rangle & 0 & 0 & 0 & 0 & 0 & 0 & 0 & 0 \\ c^\dagger_{-1}|0\rangle & 0 & 0 & 0 & 0 & 0 & 0 & 0 & 0 \\ c^\dagger_0|0\rangle & 0 & 0 & 0 & 0 & 0 & 0 & 0 & 0 \\ c^\dagger_1|0\rangle & 1 & 0 & 0 & 0 & 0 & 0 & 0 & 0 \\ c^\dagger_0 c^\dagger_{-1}|0\rangle & 0 & 0 & 0 & 0 & 0 & 0 & 0 & 0 \\ c^\dagger_1 c^\dagger_{-1}|0\rangle & 0 & 1 & 0 & 0 & 0 & 0 & 0 & 0 \\ c^\dagger_1 c^\dagger_0|0\rangle & 0 & 0 & 1 & 0 & 0 & 0 & 0 & 0 \\ c^\dagger_1 c^\dagger_0 c^\dagger_{-1}|0\rangle & 0 & 0 & 0 & 0 & 1 & 0 & 0 & 0 \end{array} \tag{B.4}$$

The operators for the different transitions of the impurity levels are already given in (6.5) and (6.6).

B.2 Two-channel Kondo case

Due to the fact that this matrices are quite huge, we will not write them down explicitly in this thesis. The starting Hamiltonian (6.3) is very large and can not fit into a page so we will just give the different components of the Hamiltonian such as the fermionic operators and impurity operators. With the knowledge of these operators one can easily build up the matrix repesentation of the Hamiltonian. Table B.1 shows the 64 possible states which are obtained in the same way as in the case of 1CK, which has already been explained above. To obtain the different fermionic operators, one has to carry out a multiplication of square matrices of dimension 64 × 64. This is a very tedious and painstaking process and it is done exactly the same way as in the case of the single-channel fermionic operators of dimension 8 × 8 that has already been mentioned in the preceding subsection. We just state the non-zero elements of these operators below.

$\|0\rangle$	$c^{\dagger}_{-1\uparrow}\|0\rangle$	$c^{\dagger}_{0\uparrow}\|0\rangle$	$c^{\dagger}_{1\uparrow}\|0\rangle$
$c^{\dagger}_{-1\downarrow}\|0\rangle$	$c^{\dagger}_{0\downarrow}\|0\rangle$	$c^{\dagger}_{1\downarrow}\|0\rangle$	$c^{\dagger}_{-1\uparrow}c^{\dagger}_{-1\downarrow}\|0\rangle$
$c^{\dagger}_{0\uparrow}c^{\dagger}_{0\downarrow}\|0\rangle$	$c^{\dagger}_{1\uparrow}c^{\dagger}_{1\downarrow}\|0\rangle$	$c^{\dagger}_{0\uparrow}c^{\dagger}_{-1\uparrow}\|0\rangle$	$c^{\dagger}_{0\downarrow}c^{\dagger}_{-1\downarrow}\|0\rangle$
$c^{\dagger}_{0\downarrow}c^{\dagger}_{-1\uparrow}\|0\rangle$	$c^{\dagger}_{0\uparrow}c^{\dagger}_{-1\downarrow}\|0\rangle$	$c^{\dagger}_{1\uparrow}c^{\dagger}_{-1\uparrow}\|0\rangle$	$c^{\dagger}_{1\downarrow}c^{\dagger}_{-1\downarrow}\|0\rangle$
$c^{\dagger}_{1\uparrow}c^{\dagger}_{-1\downarrow}\|0\rangle$	$c^{\dagger}_{1\downarrow}c^{\dagger}_{-1\uparrow}\|0\rangle$	$c^{\dagger}_{1\uparrow}c^{\dagger}_{0\uparrow}\|0\rangle$	$c^{\dagger}_{1\downarrow}c^{\dagger}_{0\downarrow}\|0\rangle$
$c^{\dagger}_{1\uparrow}c^{\dagger}_{0\downarrow}\|0\rangle$	$c^{\dagger}_{1\downarrow}c^{\dagger}_{0\uparrow}\|0\rangle$	$c^{\dagger}_{1\uparrow}c^{\dagger}_{0\uparrow}c^{\dagger}_{-1\uparrow}\|0\rangle$	$c^{\dagger}_{1\downarrow}c^{\dagger}_{0\downarrow}c^{\dagger}_{-1\downarrow}\|0\rangle$
$c^{\dagger}_{1\downarrow}c^{\dagger}_{0\downarrow}c^{\dagger}_{-1\uparrow}\|0\rangle$	$c^{\dagger}_{1\downarrow}c^{\dagger}_{0\uparrow}c^{\dagger}_{-1\uparrow}\|0\rangle$	$c^{\dagger}_{1\uparrow}c^{\dagger}_{0\downarrow}c^{\dagger}_{-1\uparrow}\|0\rangle$	$c^{\dagger}_{1\downarrow}c^{\dagger}_{0\uparrow}c^{\dagger}_{-1\downarrow}\|0\rangle$
$c^{\dagger}_{1\uparrow}c^{\dagger}_{0\downarrow}c^{\dagger}_{-1\downarrow}\|0\rangle$	$c^{\dagger}_{1\uparrow}c^{\dagger}_{0\uparrow}c^{\dagger}_{-1\downarrow}\|0\rangle$	$c^{\dagger}_{0\uparrow}c^{\dagger}_{-1\uparrow}c^{\dagger}_{-1\downarrow}\|0\rangle$	$c^{\dagger}_{0\downarrow}c^{\dagger}_{-1\uparrow}c^{\dagger}_{-1\downarrow}\|0\rangle$
$c^{\dagger}_{1\uparrow}c^{\dagger}_{-1\uparrow}c^{\dagger}_{-1\downarrow}\|0\rangle$	$c^{\dagger}_{1\downarrow}c^{\dagger}_{-1\uparrow}c^{\dagger}_{-1\downarrow}\|0\rangle$	$c^{\dagger}_{-1\uparrow}c^{\dagger}_{0\uparrow}c^{\dagger}_{0\downarrow}\|0\rangle$	$c^{\dagger}_{-1\downarrow}c^{\dagger}_{0\uparrow}c^{\dagger}_{0\downarrow}\|0\rangle$
$c^{\dagger}_{1\uparrow}c^{\dagger}_{0\uparrow}c^{\dagger}_{0\downarrow}\|0\rangle$	$c^{\dagger}_{1\downarrow}c^{\dagger}_{0\uparrow}c^{\dagger}_{0\downarrow}\|0\rangle$	$c^{\dagger}_{-1\uparrow}c^{\dagger}_{1\uparrow}c^{\dagger}_{1\downarrow}\|0\rangle$	$c^{\dagger}_{-1\downarrow}c^{\dagger}_{1\uparrow}c^{\dagger}_{1\downarrow}\|0\rangle$
$c^{\dagger}_{0\uparrow}c^{\dagger}_{1\uparrow}c^{\dagger}_{1\downarrow}\|0\rangle$	$c^{\dagger}_{0\downarrow}c^{\dagger}_{1\uparrow}c^{\dagger}_{1\downarrow}\|0\rangle$	$c^{\dagger}_{0\uparrow}c^{\dagger}_{0\downarrow}c^{\dagger}_{-1\uparrow}c^{\dagger}_{-1\downarrow}\|0\rangle$	$c^{\dagger}_{1\uparrow}c^{\dagger}_{1\downarrow}c^{\dagger}_{-1\uparrow}c^{\dagger}_{-1\downarrow}\|0\rangle$
$c^{\dagger}_{1\uparrow}c^{\dagger}_{1\downarrow}c^{\dagger}_{0\uparrow}c^{\dagger}_{0\downarrow}\|0\rangle$	$c^{\dagger}_{1\uparrow}c^{\dagger}_{0\uparrow}c^{\dagger}_{-1\uparrow}c^{\dagger}_{-1\downarrow}\|0\rangle$	$c^{\dagger}_{1\downarrow}c^{\dagger}_{0\downarrow}c^{\dagger}_{-1\uparrow}c^{\dagger}_{-1\downarrow}\|0\rangle$	$c^{\dagger}_{1\downarrow}c^{\dagger}_{0\uparrow}c^{\dagger}_{-1\uparrow}c^{\dagger}_{-1\downarrow}\|0\rangle$
$c^{\dagger}_{1\uparrow}c^{\dagger}_{0\downarrow}c^{\dagger}_{-1\uparrow}c^{\dagger}_{-1\downarrow}\|0\rangle$	$c^{\dagger}_{1\uparrow}c^{\dagger}_{-1\uparrow}c^{\dagger}_{0\uparrow}c^{\dagger}_{0\downarrow}\|0\rangle$	$c^{\dagger}_{1\downarrow}c^{\dagger}_{-1\downarrow}c^{\dagger}_{0\uparrow}c^{\dagger}_{0\downarrow}\|0\rangle$	$c^{\dagger}_{1\downarrow}c^{\dagger}_{-1\uparrow}c^{\dagger}_{0\uparrow}c^{\dagger}_{0\downarrow}\|0\rangle$
$c^{\dagger}_{1\uparrow}c^{\dagger}_{-1\downarrow}c^{\dagger}_{0\uparrow}c^{\dagger}_{0\downarrow}\|0\rangle$	$c^{\dagger}_{0\uparrow}c^{\dagger}_{-1\uparrow}c^{\dagger}_{1\uparrow}c^{\dagger}_{1\downarrow}\|0\rangle$	$c^{\dagger}_{0\downarrow}c^{\dagger}_{-1\downarrow}c^{\dagger}_{1\uparrow}c^{\dagger}_{1\downarrow}\|0\rangle$	$c^{\dagger}_{0\uparrow}c^{\dagger}_{-1\downarrow}c^{\dagger}_{1\uparrow}c^{\dagger}_{1\downarrow}\|0\rangle$
$c^{\dagger}_{0\downarrow}c^{\dagger}_{-1\uparrow}c^{\dagger}_{1\uparrow}c^{\dagger}_{1\downarrow}\|0\rangle$	$c^{\dagger}_{1\uparrow}c^{\dagger}_{0\uparrow}c^{\dagger}_{0\downarrow}c^{\dagger}_{-1\uparrow}c^{\dagger}_{-1\downarrow}\|0\rangle$	$c^{\dagger}_{1\downarrow}c^{\dagger}_{0\uparrow}c^{\dagger}_{0\downarrow}c^{\dagger}_{-1\uparrow}c^{\dagger}_{-1\downarrow}\|0\rangle$	$c^{\dagger}_{0\downarrow}c^{\dagger}_{1\uparrow}c^{\dagger}_{1\downarrow}c^{\dagger}_{-1\uparrow}c^{\dagger}_{-1\downarrow}\|0\rangle$
$c^{\dagger}_{0\uparrow}c^{\dagger}_{1\uparrow}c^{\dagger}_{1\downarrow}c^{\dagger}_{0\uparrow}c^{\dagger}_{0\downarrow}\|0\rangle$	$c^{\dagger}_{-1\uparrow}c^{\dagger}_{1\uparrow}c^{\dagger}_{1\downarrow}c^{\dagger}_{0\uparrow}c^{\dagger}_{0\downarrow}\|0\rangle$	$c^{\dagger}_{-1\downarrow}c^{\dagger}_{1\uparrow}c^{\dagger}_{1\downarrow}c^{\dagger}_{0\uparrow}c^{\dagger}_{0\downarrow}\|0\rangle$	$c^{\dagger}_{1\uparrow}c^{\dagger}_{1\downarrow}c^{\dagger}_{0\uparrow}c^{\dagger}_{0\downarrow}c^{\dagger}_{-1\uparrow}c^{\dagger}_{-1\downarrow}\|0\rangle$

Table B.1: 64 possible states in the 2CK case obtained when the fermionic operators act on the vacuum state.

(B.1) in conjunction with the basis states in Table B.1 is used to compute the six different fermionic operators listed below.
For $c^{\dagger}_{-1\uparrow}$

$$\begin{aligned}
c^{\dagger}_{2,1} = c^{\dagger}_{8,5} = c^{\dagger}_{35,9} = c^{\dagger}_{39,10} = c^{\dagger}_{23,19} = c^{\dagger}_{25,20} = c^{\dagger}_{27,21} = c^{\dagger}_{26,22} = 1.0 \\
c^{\dagger}_{47,24} = c^{\dagger}_{48,28} = c^{\dagger}_{49,29} = c^{\dagger}_{46,30} = c^{\dagger}_{43,36} = c^{\dagger}_{44,40} = c^{\dagger}_{62,45} = c^{\dagger}_{64,63} = 1.0 \\
c^{\dagger}_{11,3} = c^{\dagger}_{15,4} = c^{\dagger}_{13,6} = c^{\dagger}_{18,7} = c^{\dagger}_{32,12} = c^{\dagger}_{31,14} = c^{\dagger}_{34,16} = c^{\dagger}_{33,17} = -1.0 \\
c^{\dagger}_{50,37} = c^{\dagger}_{52,38} = c^{\dagger}_{54,41} = c^{\dagger}_{57,42} = c^{\dagger}_{58,51} = c^{\dagger}_{59,53} = c^{\dagger}_{61,55} = c^{\dagger}_{60,56} = -1.0
\end{aligned} \tag{B.5}$$

For $c^{\dagger}_{-1\downarrow}$

$$\begin{aligned}
c^{\dagger}_{5,1} = c^{\dagger}_{36,9} = c^{\dagger}_{40,10} = c^{\dagger}_{31,11} = c^{\dagger}_{32,13} = c^{\dagger}_{33,15} = c^{\dagger}_{34,18} = c^{\dagger}_{30,19} = 1.0 \\
c^{\dagger}_{24,20} = c^{\dagger}_{29,21} = c^{\dagger}_{28,22} = c^{\dagger}_{63,45} = c^{\dagger}_{59,50} = c^{\dagger}_{58,52} = c^{\dagger}_{60,54} = c^{\dagger}_{61,57} = 1.0 \\
c^{\dagger}_{8,2} = c^{\dagger}_{14,3} = c^{\dagger}_{17,4} = c^{\dagger}_{12,6} = c^{\dagger}_{16,7} = c^{\dagger}_{46,23} = c^{\dagger}_{47,25} = c^{\dagger}_{48,26} = -1.0 \\
c^{\dagger}_{49,27} = c^{\dagger}_{43,35} = c^{\dagger}_{53,37} = c^{\dagger}_{51,38} = c^{\dagger}_{44,39} = c^{\dagger}_{56,41} = c^{\dagger}_{55,42} = c^{\dagger}_{64,62} = -1.0
\end{aligned} \tag{B.6}$$

For $c^{\dagger}_{0\uparrow}$

$$\begin{aligned}
c^{\dagger}_{3,1} = c^{\dagger}_{11,2} = c^{\dagger}_{14,5} = c^{\dagger}_{9,6} = c^{\dagger}_{31,8} = c^{\dagger}_{41,10} = c^{\dagger}_{36,12} = c^{\dagger}_{35,13} = 1.0 \\
c^{\dagger}_{43,32} = c^{\dagger}_{54,39} = c^{\dagger}_{56,40} = c^{\dagger}_{45,42} = c^{\dagger}_{60,44} = c^{\dagger}_{63,55} = c^{\dagger}_{62,57} = c^{\dagger}_{64,61} = 1.0 \\
c^{\dagger}_{19,4} = c^{\dagger}_{22,7} = c^{\dagger}_{23,15} = c^{\dagger}_{28,16} = c^{\dagger}_{30,17} = c^{\dagger}_{26,18} = c^{\dagger}_{38,20} = c^{\dagger}_{37,21} = -1.0 \\
c^{\dagger}_{51,24} = c^{\dagger}_{52,25} = c^{\dagger}_{50,27} = c^{\dagger}_{53,29} = c^{\dagger}_{46,33} = c^{\dagger}_{48,34} = c^{\dagger}_{58,47} = c^{\dagger}_{59,49} = -1.0
\end{aligned} \tag{B.7}$$

For $c_{0\downarrow}^{\dagger}$

$$\begin{gathered}
c_{6,1}^{\dagger}=c_{13,2}^{\dagger}=c_{12,5}^{\dagger}=c_{32,8}^{\dagger}=c_{42,10}^{\dagger}=c_{37,19}^{\dagger}=c_{38,22}^{\dagger}=c_{50,23}^{\dagger}=1.0\\
c_{52,26}^{\dagger}=c_{51,28}^{\dagger}=c_{53,30}^{\dagger}=c_{57,39}^{\dagger}=c_{55,40}^{\dagger}=c_{61,44}^{\dagger}=c_{59,46}^{\dagger}=c_{58,48}^{\dagger}=1.0\\
c_{9,3}^{\dagger}=c_{21,4}^{\dagger}=c_{20,7}^{\dagger}=c_{35,11}^{\dagger}=c_{36,14}^{\dagger}=c_{27,15}^{\dagger}=c_{24,16}^{\dagger}=c_{29,17}^{\dagger}=-1.0\\
c_{25,18}^{\dagger}=c_{43,31}^{\dagger}=c_{49,33}^{\dagger}=c_{47,34}^{\dagger}=c_{45,41}^{\dagger}=c_{62,54}^{\dagger}=c_{63,56}^{\dagger}=c_{64,60}^{\dagger}=-1.0
\end{gathered}\tag{B.8}$$

For $c_{1\uparrow}^{\dagger}$

$$\begin{gathered}
c_{4,1}^{\dagger}=c_{15,2}^{\dagger}=c_{19,3}^{\dagger}=c_{17,5}^{\dagger}=c_{21,6}^{\dagger}=c_{10,7}^{\dagger}=c_{33,8}^{\dagger}=c_{37,9}^{\dagger}=1.0\\
c_{23,11}^{\dagger}=c_{29,12}^{\dagger}=c_{27,13}^{\dagger}=c_{30,14}^{\dagger}=c_{40,16}^{\dagger}=c_{39,18}^{\dagger}=c_{42,20}^{\dagger}=c_{41,22}^{\dagger}=1.0\\
c_{55,24}^{\dagger}=c_{57,25}^{\dagger}=c_{54,26}^{\dagger}=c_{56,28}^{\dagger}=c_{46,31}^{\dagger}=c_{49,32}^{\dagger}=c_{44,34}^{\dagger}=c_{50,35}^{\dagger}=1.0\\
c_{53,36}^{\dagger}=c_{45,38}^{\dagger}=c_{59,43}^{\dagger}=c_{61,47}^{\dagger}=c_{60,48}^{\dagger}=c_{63,51}^{\dagger}=c_{62,52}^{\dagger}=c_{64,58}^{\dagger}=1.0
\end{gathered}\tag{B.9}$$

For $c_{1\downarrow}^{\dagger}$

$$\begin{gathered}
c_{7,1}^{\dagger}=c_{18,2}^{\dagger}=c_{22,3}^{\dagger}=c_{16,5}^{\dagger}=c_{20,6}^{\dagger}=c_{34,8}^{\dagger}=c_{38,9}^{\dagger}=c_{26,11}^{\dagger}=1.0\\
c_{24,12}^{\dagger}=c_{25,13}^{\dagger}=c_{28,14}^{\dagger}=c_{48,31}^{\dagger}=c_{47,32}^{\dagger}=c_{52,35}^{\dagger}=c_{51,36}^{\dagger}=c_{58,43}^{\dagger}=1.0\\
c_{10,4}^{\dagger}=c_{39,15}^{\dagger}=c_{40,17}^{\dagger}=c_{41,19}^{\dagger}=c_{42,21}^{\dagger}=c_{54,23}^{\dagger}=c_{57,27}^{\dagger}=c_{55,29}^{\dagger}=-1.0\\
c_{56,30}^{\dagger}=c_{44,33}^{\dagger}=c_{45,37}^{\dagger}=c_{60,46}^{\dagger}=c_{61,49}^{\dagger}=c_{62,50}^{\dagger}=c_{63,53}^{\dagger}=c_{64,59}^{\dagger}=-1.0
\end{gathered}\tag{B.10}$$

One uses all the above matrices to build up the starting Hamiltonian that is needed for the NRG calculations.

Appendix C

Numerical renormalization group symmetry construction

Like any physically relevant model, the partially broken SU(3) Kondo model is charge conserving. Since this model is a non-magnetic impurity model and the spin of the conduction sea electrons act like the channel index, consequently the z-component of the spin of these electron is conserved. We make use of these two symmetries in our code. All the states in the subspaces are classified according to the respective quantum number Q and S_z. In the single-channel version of our model only the charge symmetry is considered since only electrons of a the same spin direction are present due to the strong magnetic field applied to the conduction sea. The single-channel case can even be ran without making use of the symmetries since that Hilbert space grows only by a factor of 8. This means that, the sizes of the matrices to be diagonalized are not so large and can effectively be stored in moderate computer memory. The sophisticated case here is the two-channel version of the model where the Hilbert space grows by a factor of 64 after each iteration. Therefore the matrices to be diagonalized are so large that, they can not be stored in moderate computer memory. Even if they could be stored in memory, it will take an extremely long time for the computer to diagonalize these matrices. As already mentioned, the use of symmetry gives us a way round this problem of memory and speed. It also reduces round-off errors due to the diagonalization of large matrices.

C.1 Charge (Q) and z-component of the total spin (S_z) symmetry

Single-channel Kondo

Here we only have the charge conserving quantum number Q and it is quite easy to implement. The 8 possible states are enumerated as done in the preceding appendix and then the charge of each of the states is summed. These charges are then used to break up the Hamiltonian matrix into block matrices that are indexed by these charges. These block Hamiltonian matrices can now be diagonalize independent of each other. The block matrices are far smaller than the whole Hamiltonian matrix hence greatly reducing the roundoff errors compared to the diagonalization of the full matrix.

In Table C.1, the first column i numbers the possible ways of adding the angular momenta together. In the partially broken SU(3) Kondo, i runs from 1 to 8. The second column in Table C.1 is for the charge quantum number Q which is obtained (5.5). While the third column denoted by n just indexes different states with the same Q values. This enables us to generate a basis with well defined Q and S_z for a newly added site in the Wilson chain when provided with the eigenstates of the rest of the chain from the preceding iteration.

i	Q	n
1	-1	1
2	0	3
3	0	3
4	0	3
5	1	3
6	1	3
7	1	3
8	2	1

Table C.1: Charge conserving basis states for the new iteration in an NRG calculation.

Two-channel Kondo

The S_z component comes into play in the 2CK scenario since the conduction sea electrons are degenerate. Using both (5.4) and (5.5) one obtains Table C.2. The use of symmetries here is very essential since the Hilbert space grows very fast. Due to this large Hilbert space, the system is truncated just after the first iteration when 1000 states are kept. It takes about three days to complete an entire NRG calculations when the number of iteration is 50 on a computer with a processor speed of 3.00 GHz and at least 8 GB of memory (RAM). In the case where 2000 states are kept, the time to complete the calculations will be multiplied by 8 since the time to diagonalize the matrices scales as a factor of N^3 where N is the dimension of the matrix. So if the number of states is doubled then the time is multiplied by 2^3. This means that for 2000 states, it takes about 24 days for a complete NRG run and about 30 GB of memory (RAM). Without the use of symmetries, it would practically be impossible to run the 2CK version of this model.

Table C.1 gives us the different values of the possible ways for the adding of angular momenta i in column one. Column two is the charge quantum number Q, while column three is the z-component of the total spin S_z. The value of S_z is usually multiplied by 2 just to avoid dealing with fractions, hence the whole numbers in the third column. The last but not least is column five, which is represented by n that indexes the states with the same Q and S_z. The different states involved in the 2CK case have already been given in the preceding appendix. One can see in Table C.1 that, instead of dealing with a 64×64 matrix, one is rather dealing with much smaller matrices of the different subspaces of the different quantum numbers Q and S_z of dimensions indicated by the n values in the fourth column.

i	Q	S_z	n
1	-1	0	1
2	0	1	3
3	0	1	3
4	0	1	3
5	0	-1	3
6	0	-1	3
7	0	-1	3
8	1	0	9
9	1	0	9
10	1	0	9
11	1	0	9
12	1	0	9
13	1	0	9
14	1	0	9
15	1	0	9
16	1	0	9
17	1	-2	3
18	1	-2	3
19	1	-2	3
20	1	2	3
21	1	2	3
22	1	2	3
23	2	-3	1
24	2	-1	9
25	2	-1	9
26	2	-1	9
27	2	-1	9
28	2	-1	9
29	2	-1	9
30	2	-1	9
31	2	-1	9
32	2	-1	9
33	2	1	9
34	2	1	9
35	2	1	9
36	2	1	9
37	2	1	9
38	2	1	9
39	2	1	9
40	2	1	9
41	2	1	9
42	2	3	1
43	3	-2	3
44	3	-2	3
45	3	-2	3
46	3	0	9
47	3	0	9
48	3	0	9
49	3	0	9
50	3	0	9
51	3	0	9
52	3	0	9
53	3	0	9
54	3	0	9
55	3	2	3
56	3	2	3
57	3	2	3
58	4	-1	3
59	4	-1	3
60	4	-1	3
61	4	1	3
62	4	1	3
63	4	1	3
64	5	0	1

Table C.2: The basis states for an added site for the 2CK scenario used to build up the $i-th$ combination of the basis states of the current iteration for the Q and S_z basis.

Appendix D

Calculation of impurity contribution to the entropy of the system

In an attempt to calculate the impurity contribution to the entropy of the system, we follow exactly the approach of Bulla et al. in [50]. The knowledge of the low-lying energy levels of the system can permit us to acquire insight into the physical properties of the system under study especially the thermodynamic ones. The inverse temperature at each iteration is defined as follows

$$\beta_N = (k_B T_N)^{-1} \tag{D.1}$$

where by definition

$$\beta_N \Lambda^{-(N-1)/2} = \bar{\beta} \tag{D.2}$$

N is the iteration number and T_N is the temperature at the respective iteration number. One can use the truncated Hamiltonian to calculate the impurity contribution to the entropy at each iteration at the energy scale of $k_B T_N$. The value of $\bar{\beta}$ depends on two factors namely the number of states kept and the discretization parameter. Generally, $\bar{\beta}$ is of order one. In this thesis we have used $\bar{\beta}$ in the range of 1.2 to 1.5. If the Hamiltonian at each iteration is denoted by H^N where N is the iteration number, then the expression of the entropy by definition has the form below

$$S^N/k_B = \beta \langle H^N \rangle + \ln Z^N \tag{D.3}$$

This quantity is actually calculated using the NRG in the following way

$$\langle H^N \rangle = \frac{1}{Z^N} \sum_{Q,S_z} \sum_i E_N(Q, S_z, i) e^{-\beta E_N(Q,S_z,i)} \tag{D.4}$$

where $E_N(Q, S_z, i)$ are the eigenenergies labeled with respect to the different subspaces of the charge (Q) and z-component of the total spin (S_z) quantum number, respectively. While Z^N is the partition function at iteration N and it is defined as follows

$$Z^N = \sum_{Q,S_z} \sum_i E_N(Q, S_z, i) e^{-\beta E_N(Q,S_z,i)} \tag{D.5}$$

One can then deduce the impurity contribution to the entropy for temperature

$$k_B T_N = \Lambda^{-(N-1)/2} / \bar{\beta}. \tag{D.6}$$

as follows

$$S_{imp}(T_N)/k_B \approx S^N/k_B - S^N_{cb}/k_B \tag{D.7}$$

where S^N_{cb}/k_B is the entropy of the conduction sea without the impurity and obtained in the following way

$$S^N_{cb}/k_B = \beta\langle H^N_{cb}\rangle^N + \ln Z^N_{cb} \tag{D.8}$$

where H_{cb} is the Hamiltonian of the bare conduction band and given by

$$H^N_{cb} = \sum_{\sigma n=0}^{N} [\varepsilon_n c^\dagger_{n\sigma} c_{n\sigma} + t_n (c^\dagger_{n\sigma} c_{n+1\sigma} + c^\dagger_{n+1\sigma} c_{n\sigma}) \tag{D.9}$$

where t_n is the hopping matrix between nearest sites on the chain and decays like $\Lambda^{-n/2}$ for large n. The fact that t_n behaves in this way is very important because it enables one to associate a particular chain length N with the temperature or energy scale of the model as in [1, 52, 62].

Bibliography

[1] K. G. Wilson, Rev. Mod. Phys. **47**, 775 (1975).

[2] M. Arnold, T. Langenbruch, and J. Kroha, Phys. Rev. Lett. **99**, 186601 (2007).

[3] D. C. Ralph and R. A. Buhrman, Phys. Rev. Lett. **69**, 2118 (1992); Phys. Rev. B. **51**, 3554 (1995).

[4] J. Kondo, Prog. theor. Phys. **32**, 37 (1964).

[5] N. Andrei, Phys. Rev. Lett. **45**, 379 (1980).

[6] P. B. Wiegmann, Sov. Phys. JETP Lett. **31**, 392 (1980).

[7] P. Nozières and A. Blandin, Journal de Physique(Paris), **41**, 193(1980).

[8] D. M. Cragg, P. Lloyd, and P. Nozières, J. Phys. C, **13**, 803 (1980).

[9] H. B. Pang, and Cox, D. L., Phys. Rev. B, **44**, 9454. (1991).

[10] N. Andrei and C. Destri, Phys. Rev. Lett. **52**, 364 (1984).

[11] A. M. Tsvelik and P. B. Wiegmann, Z. Phys. B **54**, 201 (1994).

[12] I. Affleck and A. W. W. Ludwig, Nucl. Phys. B **352**, 849 (1991).

[13] A. W. W. Ludwig and I. Affleck, Phys. Rev. Lett. **67**, 3160 (1991).

[14] I. Affleck and A. W. W. Ludwig, Phys. Rev. B **48**, 7297 (1993).

[15] P. Coleman, L. B. Ioffe, and A. M. Tsvelik, Phys. Rev. B **52**, 6611 (1995).

[16] K. Vladár and A. Zawadowski, Phys. Rev. B **28**, 1564 (1983).

[17] I. L. Aleiner, B. L. Altshuler, Y. M. Galperin, and T. A. Shutenko, Phys. Rev. Lett. **86**, 2629 (2001).

[18] I. L. Aleiner and D. Controzzi, Phys. Rev. B **66**, 045107 (2002).

[19] K. Ballmann and J. Kroha, Ann. Phys. (Berlin) 524, No 3-4, 245-251(2012).

[20] W. J. de Haas, J. H. de Boer, and G. J. van den Berg, Physica **1**, 1115 (1934).

[21] P. W. Anderson, Phys. Rev. **124**, 41-53 (1961).

[22] J. R. Schrieffer and P. A. Wolff, Phys. Rev. **149**, 491 (1966).

[23] A. A. Abrikosov, Physics **2**, 5 (1965).

[24] S. E. Barnes, J. Phys. F **6**, 1375 (1976); J. Phys. F **7**, 2637 (1977).

[25] M. Gell-Mann and F. Low, Phys. Rev. **95**, 1300 (1954).

[26] A. A. Abrikosov and A. A. Migdal, J. Low. Temp. Phys. **3**, 519 (1970).

[27] M. Fowler and A. Zawadowski Solid St. Commun. **9**, 471 (1971).

[28] P. W. Anderson, J. Phys. C **3**, 2436-2441 (1970).

[29] A. C. Hewson, *The Kondo Problem to heavy Fermions* (Cambridge University Press, Cambridge, 1993).

[30] A. A. Abrikosov, L. P. Gorkov, and I. E. Dzyaloshinski, *Method of Quantum Field Theory in Statistical Physics* (Dover O-486-63228-8, 1975).

[31] P. Nozières, J. Low. Temp. Phys. **17**, 31 (1974).

[32] C. Kolf and J. Kroha, Phys. Rev. B **75**, 45129 (2007).

[33] D. L. Cox and A. Zawadowski, Adv. Phys. **47**, 599 (1998).

[34] J. Kondo, Physica (Utrecht) **84B**, 40 (1976).

[35] J. Kondo, Physica (Utrecht) **84B**, 207 (1976).

[36] K. S. Ralls and R. A. Buhrman, Phys. Rev. Lett. **60**, 2434 (1988); Phys. Rev. B **44**, 5800 (1991).

[37] E. L. Wolf, *Principles of Electron tunneling Spectroscopy* (Oxford Univ. Press, New York, 1989).

[38] A. M. Duif, A. G. M. Jansen, and P. Wyder, J. Phys. Condens. Matter **1**, 3157 (1989).

[39] K. S. Ralls, R. A. Buhrman, and R. C. Tiberio, Appl. Phys. Lett. **55**, 2459 (1989).

[40] I. K. Yanson and O. I. Shklyarevskii, Sov. J. Low Temp. Phys. **12**, 509 (1986).

[41] V. Yu. Sharvin, Sov. Phys. -JETP **21** 655 (1965).

[42] K. Vladár and A. Zawadowski, Phys. Rev. B **28**, 1582 (1983); Phys. Rev. B **28**, 1596 (1983).

[43] A. Halbritter, L. Borda, and A. Zawadowski, Adv. Phys. **53**, 939 (2004).

[44] M. H. Hettler, J. Kroha, and S. Hershfield, Phys. Rev. Lett. **73**, 1967 (1994).

[45] D. C. Ralph, a. W. W. Ludwig, J. von Deft, and R. A. Buhrmann, Phys. Rev. Lett. **72**, 770 (1994).

[46] Y. Kagan and N. V. Prokof'ev, Solid State Commun. **65** 1385 (1988); Sov. Phys. JETP **70** 957 (1990).

[47] P. W. Anderson, B. I. Halperin, C. M. Varma Phil. Mag. **25** 1 (1972).

[48] W. A. Philips, J. Low Temp. Physics **7** 351 (1972).

[49] R. C. Zeller, R. O. Pohl, Phys. Rev. B **4** 2029 (1971).

[50] R. Bulla, T. A. Costi, and Th. Pruschke, Rev. Mod. Phys. **80**, 395 (2008).

[51] K. J. Lanczos *Res. Natl. Bur. Stand* ***45**, 225(1950).*

[52] H. R Krishna-murthy, J. W. Wilkins, and K. G. Wilson, Phys. Rev. B, **21**, 1003 (1980a).

[53] Linear Algebra PACKage (LAPACK, Fortran and C libraries; an implementation of the BLAS library is required for this package), URL *http://www.netlib.org/lapack*.

[54] Basic Linear Algebra Subprograms (BLAS, Fortran libraries providing basic matrix and vector operations), URL *http://www.netlib.org/blas*.

[55] O. Sakai, Y. Shimizu, and T. Kasuya, J. Phys. Soc. Japan, **58** 3666, (1989).

[56] T. A. Costi, A. C. Hewson, and V. Zlatic, J. Phys.: Cond. Matter **6**, 2519 (1994).

[57] R. Bulla, T. A. Costi and D. Vollhardt, Phys. Rev. B **64**, 045103 (2001).

[58] J. Kondo, Phys. Rev. **169**, 437 (1968).

[59] D. M. Cragg and P. Lloyd, J. Phys. C: Solid State Phys., **11**, 597 (1978).

[60] I. Affleck, Acta Phys. Polon. B **26** 1869-1932 (1995).

[61] K. Ballmann, Diplomarbeit, Bonn University, 2008 (unpublished).

[62] W. C. Oliveira and L. N. Oliveira, Phys. Rev. B **49** 11986 (1994).